



UNIVERSITY OF VERONA

DEPARTMENT OF MEDICINE

PhD School of Life and Health Sciences

PhD in Inflammation, Immunity and Cancer

XXXV CYCLE




Modelling adaptation of PDAC to microenvironmental pressures

Coordinator: Prof. Vincenzo Corbo

Supervisor: Prof. Vincenzo Corbo

PhD Candidate: Dott.ssa Antonia Malinova

This work is licensed under a Creative Commons Attribution-NonCommercial- NoDerivs 3.0 Unported License, Italy. To read a copy of the licence, visit the web page:
<http://creativecommons.org/licenses/by-nc-nd/3.0/>

-  **Attribution** — You must give [appropriate credit](#), provide a link to the license, and [indicate if changes were made](#). You may do so in any reasonable manner, but not in any way that suggests the licensor endorses you or your use.
-  **NonCommercial** — You may not use the material for [commercial purposes](#).
-  **NoDerivatives** — If you [remix, transform, or build upon the material](#), you may not distribute the modified material.

Modelling adaptation of PDAC to microenvironmental pressures

Antonia Malinova

PhD thesis

Verona, January 09th 2024

Table of Contents

Abstract	3
1. General introduction and aims	4
1.1. Pancreas anatomy and function.....	4
1.2. Pancreatic cancer	6
1.3. Pancreatic ductal adenocarcinoma (PDAC).....	6
1.4. Aims.....	15
2. Establishment of PDOs from post-treatment tumours	17
3. RSPO is an essential stromal cue, provided by CAFs and endothelial cells.	34
4. ecDNA amplification of MYC drives intratumoral copy-number heterogeneity and adaptation to stress in PDAC.....	55
5. Concluding remarks	102
6. References	104
7. Acknowledgments.....	129

Abstract

Pancreatic ductal adenocarcinoma (PDAC) is an extremely lethal disease with the lowest survival rate of all cancers. It is characterised by a dense stroma, few neoplastic cells, and extreme heterogeneity in both the stromal and epithelial compartments. As PDAC is characterised by therapy resistance and high relapse rates, we first focused on the effects of neoadjuvant therapy on cancer cells. We established a library of patient-derived organoids (PDOs) from treated and non-treated tumours. The integration of DNA and RNA-sequencing revealed few differences between the two cohorts, with transcriptomic signatures of metabolic and epigenetic reprogramming enriched in post-treatment tumours. Next, we explored the importance of microenvironmental cues, present in the culture medium, on the propagation of PDOs. We found that the WNT pathway activator, *RSPO3*, is an essential cue for organoids' survival, and its expression is mostly confined to the stromal compartment of PDAC tissues (i.e., fibroblasts and endothelial cells). In keeping with this finding, endothelial cells could rescue PDOs survival in the absence of *RSPO*. Leveraging this known dependency of PDOs on the exogenous supplementation of stromal cues, we modelled the dynamics of oncogene amplifications on extrachromosomal DNA (ecDNAs). EcDNAs are circular elements containing oncogenes that are inherited through a non-Mendelian pattern and can supercharge oncogene expression due to increased chromatin accessibility. We found that PDOs can adapt to the withdrawal of Wnt ligands in the culture medium also through increased activity of *MYC* and that this occurs more rapidly when *MYC* is on ecDNAs. ecDNAs drove exceptionally high dosage of *MYC* and allowed cancer cells rapid adaptation to microenvironmental changes. However, the continued maintenance of extrachromosomal *MYC* was uniquely ensured by the presence of selective pressure. *MYC* dosage affected cell morphology and dependence of cancer cells on stromal niche factors, with the highest *MYC* levels correlating with squamous-like phenotypes. Collectively, this work provides the first omics analysis of PDOs from treated tumours, evidence that endothelial cells can support PDAC cells by providing niche factors and the first detailed analysis of ecDNAs in PDAC as a new genetic mechanism driving *MYC* heterogeneity.

1. General introduction and aims

1.1. Pancreas anatomy and function

The pancreas is an endoderm-derived organ, located deep in the abdomen, behind the stomach (Walkowska *et al.*, 2022; Talathi, Zimmerman and Young, 2023). Macroscopically, it is divided into three parts: head, body, and tail (Figure 1; Walkowska *et al.*, 2022). The head is located above the superior mesenteric artery and vein, and it is surrounded by the loop of the duodenum (Figure 1; Walkowska *et al.*, 2022). The pancreatic body extends almost perpendicularly to connect the head with the tail. It crosses anteriorly major vessels, including the superior mesenteric artery and vein, the abdominal aorta, and the inferior vena cava (Figure 1; Walkowska *et al.*, 2022). Finally, the tail is surrounded by the spleen (Figure 1; Walkowska *et al.*, 2022).

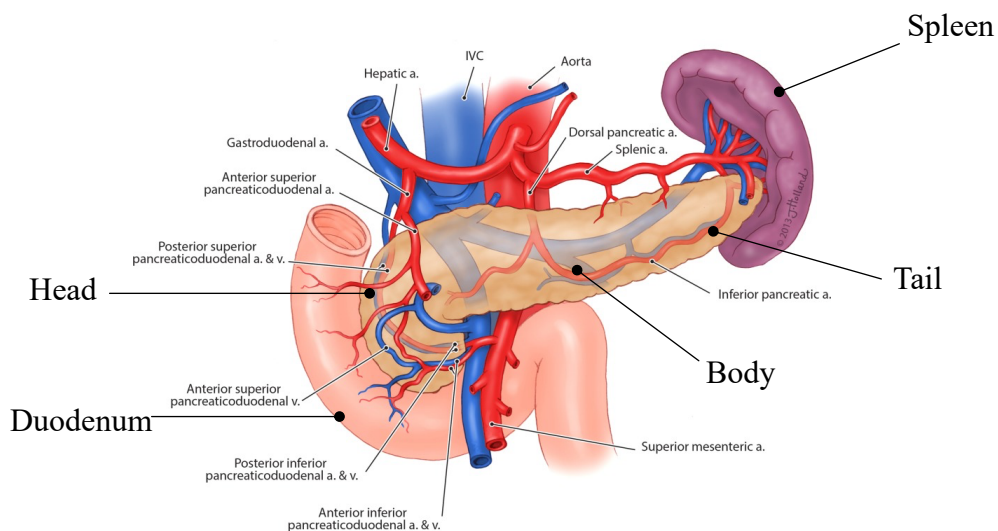


Figure 1. Anatomy of the pancreas. Schematic representation of the pancreas anatomy and location with respect to major blood vessels and other organs. IVC: Inferior vena cava, a: artery, v: vein. Adapted from Cesmebasi *et al.*, 2015.

The pancreas has two distinct functions: exocrine (food digestion via release of enzymes) and endocrine (regulation of glucose homeostasis via release of hormones) (Lodestijn *et al.*, 2021). The exocrine part, which makes up most of the organ, produces digestive enzymes and delivers them to the duodenum (Pandol, 2010). Acinar cells, organised into grape-like structures, secrete the digestive

enzymes into a lumen, lined with intercalated ducts (Figure 2A; Logsdon et al., 2013; Pandiri, 2014). The intercalated ducts are made up of centroacinar cells, whose main function is to secrete bicarbonates for neutralisation of stomach acids and prevention of enzymes aggregation (Figure 2A; Hegyi et al., 2011; Reichert & Rustgi, 2011). Macroscopically, acinar and centroacinar cells are organised into lobules, which are connected by a complex system of ducts that transport the digestive enzymes to the gut (Figure 2A; A-Kader & Ghishan, 2012; Hegyi et al., 2011). The last component of the exocrine pancreas, the ducts, are lined with ductal cells, which also produce bicarbonates to neutralise stomach acids (Figure 2A; Grapin-Botton, 2005).

The endocrine pancreas secretes hormones into the bloodstream, which regulate glucose levels (Röder *et al.*, 2016). The working unit of the endocrine pancreas is the Islet of Langerhans, which comprise 1-2 % of the organ (Röder *et al.*, 2016). They are composed of four hormone-secreting cell types: α cells (secrete glucagon to increase blood glucose levels), β cells (secrete insulin to reduce blood glucose levels), δ cells (secrete somatostatin to inhibit both glucagon and insulin production), and γ cells (release pancreatic polypeptide, regulating both digestive enzymes and hormones release) (Figure 2B; Röder et al., 2016). Finally, the islets are highly vascularised to ensure efficient delivery of the hormones into the bloodstream (Figure 2B; Muratore, Santos and Rorsman, 2021).

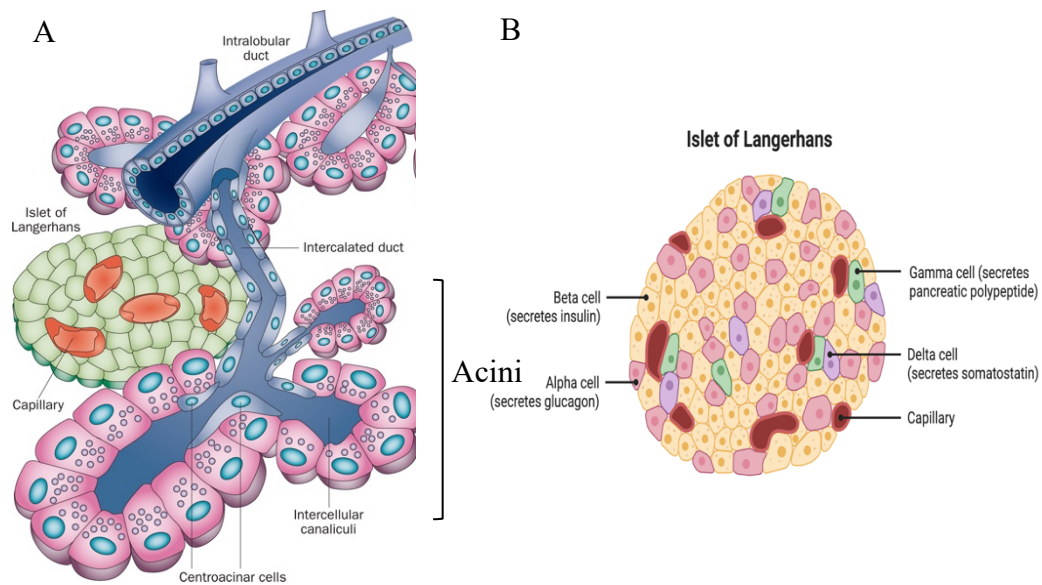


Figure 2. Functional units of the exocrine (A) and endocrine (B) pancreas. A. Schematic representation of the organisation of the acini and the ductal system. Adapted from Logsdon et al., 2013 B. Representation of the cells that make up the Islet of Langerhans, along with their functions. Created with BioRender.com.

1.2. Pancreatic cancer

Pancreatic cancer can affect both the exocrine and endocrine compartments, however endocrine tumours are rather rare, accounting for less than 5 % of all pancreatic cancer cases (Fesinmeyer *et al.*, 2005). Pancreatic cancers arising from the exocrine compartment are much more prevalent, with pancreatic ductal adenocarcinoma (PDAC), being the most common.

1.3. Pancreatic ductal adenocarcinoma (PDAC)

PDAC is the most common type of pancreatic cancer, and it affects the exocrine portion of the organ with the majority of PDACs arising in the head (60 - 70 %) (Sarantis *et al.*, 2020). It is a highly aggressive disease, with a five-year survival rate of 12 %, the lowest one out of all cancers (Siegel *et al.*, 2023). The high mortality is due to the late diagnosis, when most patients are not eligible for tumour resection: at presentation of first symptoms, 80 - 85 % of patients already have locally advanced or even metastatic disease (Hackert and Büchler, 2013). Moreover, among patients eligible for surgery there is a relapse rate of up to 80 %

(Dunne and Hezel, 2015). In addition to the late diagnosis and high recurrence rate, currently there are no effective immune- or personalised therapies, thus leaving patients only with chemo- and radiation-therapy as treatment options (Hosein *et al.*, 2022). However, due to its biology and inter- and intra-patient heterogeneity, PDAC remains extremely refractory to those therapies (Quiñonero *et al.*, 2019; Evan, Wang and Behrens, 2022).

1.3.1. Aetiology of PDAC

The majority of PDAC cases occur without any genetic predisposition (Bekkali and Oppong, 2017). Generally, PDAC occurs in older populations, with the median age of diagnosis of 70 (Hu *et al.*, 2021). Moreover, males are usually at a higher risk than females (Hu *et al.*, 2021). Modifiable risk factors, such as tobacco smoking, alcohol abuse, and obesity have also been shown to significantly increase the risk of PDAC incidence (Hu *et al.*, 2021). Finally, patients with chronic pancreatitis and diabetes are more likely to develop PDAC (Hu *et al.*, 2021).

Up to 10 % of PDAC cases are patients with familial history of the disease, where at least two first-degree relatives have been diagnosed with PDAC (Bekkali and Oppong, 2017). There are also certain germline mutations that can predispose patients, such as mutations in DNA damage repair genes (e.g.: *BRCA1* and *BRCA2*), occurring in around 8 % of cases (Bekkali and Oppong, 2017; Rosen, Goodwin and Vickers, 2021).

1.3.2. Tumorigenesis and histopathology

PDAC can arise from three types of precursor lesions: pancreatic intraepithelial neoplasia (PanINs), intraductal papillary mucinous neoplasms (IPMNs) or mucinous cystic neoplasms (MCNs) (Basturk *et al.*, 2015). These non-invasive lesions are a result of both oncogenic mutations and tissue inflammation (Basturk *et al.*, 2015). PanINs, IPMNs, and MCNs progress histologically through different grades, based on their degree of cellular atypia (Lennon *et al.*, 2014). Along with the histological progression, the mutational burden also increases with oncogenic mutations already present in early grade lesions (Figure 3; (Lennon *et al.*, 2014)).

However, further inactivating mutations in tumour suppressor genes, are usually required for the transition into *in situ* carcinoma (Figure 3; (Lennon *et al.*, 2014)). Despite PDAC's ductal morphology, both acinar and ductal cells have been identified as potential cells of origin (Figure 3; Malinova *et al.*, 2021). For acinar cells to transform into cancer, they first must *trans*-differentiate into ductal cells via a process called acinar-to-ductal metaplasia (ADM, Figure 3; (Guerra *et al.*, 2007; Habbe *et al.*, 2008; Kopp *et al.*, 2012; J. Bailey *et al.*, 2016; Lee *et al.*, 2019)). Despite being histologically very similar at first, the cell of origin can dictate the disease progression (J. Bailey *et al.*, 2016; Lee *et al.*, 2019; Flowers *et al.*, 2021). Acinar-derived tumours exhibit a stepwise progression from ADM, through pre-neoplastic lesions, into PDAC, whilst ductal-derived tumours are thought to transition straight into invasive carcinomas (Peter Bailey *et al.*, 2016; Ferreira *et al.*, 2017; Flowers *et al.*, 2021). However, it is possible that ductal-derived tumours also generate PanINs, which might be difficult to detect as they progress very quickly (Figure 3; Malinova *et al.*, 2021).

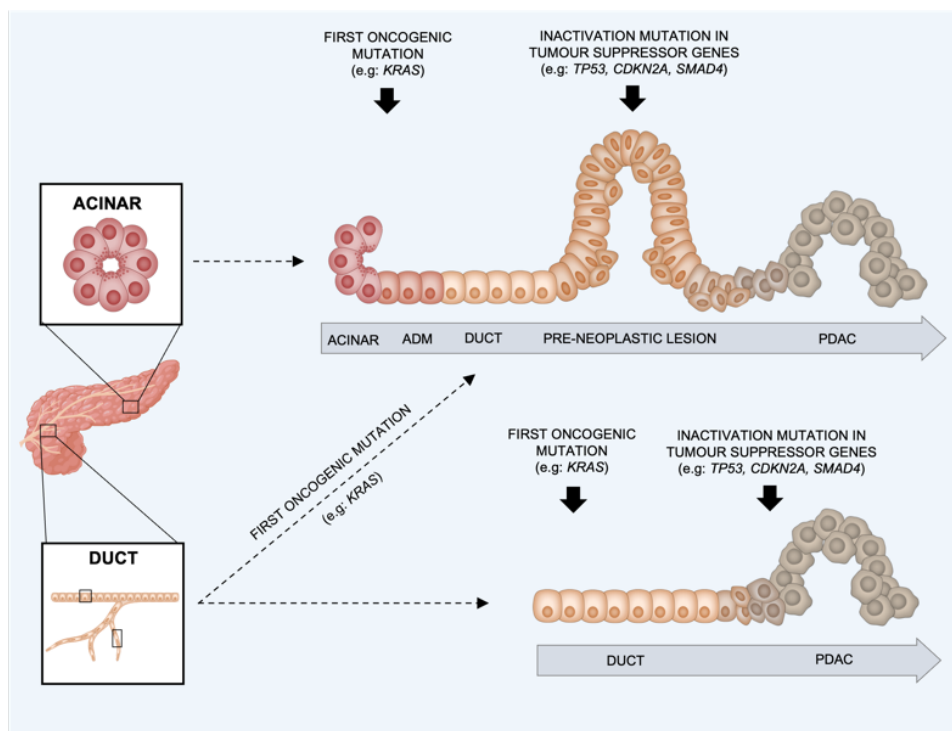


Figure 3. PDAC progression. PDAC progression from ductal or acinar cells. Malinova *et al.*, 2021.

1.3.3. PDAC Genetics

The earliest oncogenic mutation in PDAC is an activating mutation in the Kirsten rat sarcoma virus oncogene (*KRAS*), present in 90 % of PDAC cases (Figure 3; Biankin *et al.*, 2012). *KRAS* stimulates cell proliferation and survival through multiple downstream pathways (Bourne, Sanders and McCormick, 1990; Suzuki *et al.*, 2021). However, progression into PDAC requires further inactivating mutations in tumour suppressor genes, such as *TP53* and *CDKN2A*, present in up to 70 % and 90 % of patients, respectively (Schutte *et al.*, 1997; Maitra *et al.*, 2003; Hezel *et al.*, 2006; Raphael *et al.*, 2017). Despite the high prevalence of these driver mutations, PDAC is characterised by extensive intra- and inter-tumour heterogeneity. Genetically, the heterogeneity is due to a long tail of infrequent mutations, which affect important processes, such as chromatin remodelling and DNA damage repair (Jones, Zhang, Parsons, *et al.*, 2008; Biankin *et al.*, 2012; Kanda *et al.*, 2012; Waddell *et al.*, 2015; The Cancer Genome Atlas Research Network, 2017).

In addition to the complex mutational profile, PDAC also exhibits extensive copy number variation (CNV) heterogeneity (Ying *et al.*, 2016). In fact, chromosomal rearrangements, copy gains, and genome tetraploidisation have been shown to increase levels of genomic instability, driving disease progression and heterogeneity (Waddell *et al.*, 2015; Chan-Seng-Yue *et al.*, 2020). Major oncogene drivers, such as *KRAS* and genes encoding receptor tyrosine kinases, are affected by copy number aberrations (Waddell *et al.*, 2015; Chan-Seng-Yue *et al.*, 2020). In metastatic PDACs, the oncogene *MYC* is commonly amplified and increased *MYC* copy number is associated with poor prognosis (Witkiewicz *et al.*, 2015; Brar *et al.*, 2019). More recently, amplifications on extrachromosomal DNAs (ecDNAs) have also been detected in PDAC, but how ecDNAs drive heterogeneity in this disease remains unknown (Kim *et al.*, 2020).

1.3.4. PDAC Molecular subtypes

To reconcile PDAC's heterogeneity, several molecular classifications have been derived based on bulk transcriptomics from primary treatment naïve PDACs and 2D cell lines (Collisson *et al.*, 2011; Moffitt *et al.*, 2015; Peter Bailey *et al.*, 2016; Puleo *et al.*, 2018). When corrected for purity of samples, what emerges from these

analyses, is the existence of two consensus subtypes: classical/progenitor and basal-like/squamous (Raphael *et al.*, 2017). The classical subtype is characterised by a higher expression of endodermal cell-fate regulators, such as *GATA6* and *HNF1/4A*, while the basal-like/squamous subtype presents loss of pancreatic endoderm identity and upregulation of programmes, driven by Δ Np63 and TGF β (Figure 4; (Collisson *et al.*, 2011; Moffitt *et al.*, 2015; Peter Bailey *et al.*, 2016; Puleo *et al.*, 2018). The classical subtype is also generally considered less aggressive than the basal-like/squamous, however those differences seem to be marginal (Collisson *et al.*, 2011; Moffitt *et al.*, 2015; Peter Bailey *et al.*, 2016; Puleo *et al.*, 2018). Studies showing inactivation of chromatin remodelling genes, which silence endodermal transcriptional programmes, suggest that the classical PDAC is the default subtype, and it progresses into a squamous one through epigenetic silencing (Figure 4; (Peter Bailey *et al.*, 2016; Brunton *et al.*, 2020; Kloesch *et al.*, 2021). However, with the advent of single-cell technologies, there is now increasing evidence that the two subtypes co-exist in the same tumour and sometimes, the same cell (Figure 4; Puleo *et al.*, 2018; Porter *et al.*, 2019; Chan-Seng-Yue *et al.*, 2020; Juiz *et al.*, 2020; Nicolle *et al.*, 2020; Krieger *et al.*, 2021; Raghavan *et al.*, 2021; Hwang *et al.*, 2022). Basal-like cells seem to accumulate in advanced and post-treatment disease, supporting the idea the basal-like phenotype emerges during PDAC progression or after environmental selection (Porter *et al.*, 2019; Chan-Seng-Yue *et al.*, 2020; Hwang *et al.*, 2022). In summary, the basal-like subtype can originate from the classical one, via epigenetic and genetic dysregulations in endodermal transcription programmes or via selection of clones (Malinova *et al.*, 2021).

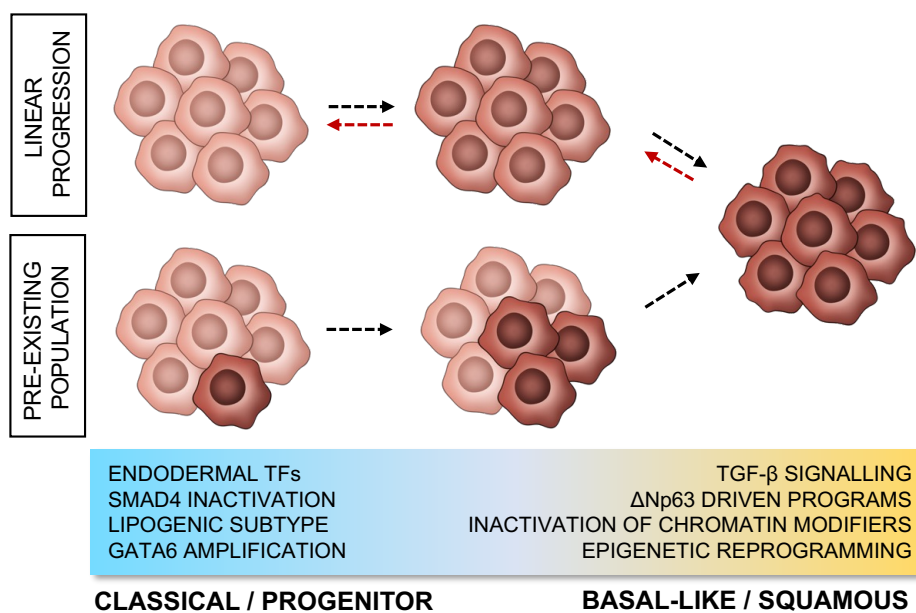


Figure 4. PDAC subtypes' characteristics and progression. (Malinova *et al.*, 2021).

1.3.5. PDAC Microenvironment

A cornerstone of PDAC, regardless of molecular subtype, is the prevalence of a strong desmoplastic reaction and low neoplastic cellularity. Most of the tumour (up to 80 % of its mass) is comprised of stroma (Erkan *et al.*, 2012). The dense stroma creates a high pressure, collapsing blood vessels, and creates a metabolically hostile environment, which selects for highly resilient tumour cells (Figure 5; Bulle and Lim, 2020).

Just like with the epithelial compartment, there have been multiple studies, based on transcriptomic data, attempting to subtype the stroma. Bulk transcriptomic studies from PDACs have identified two stromal subtypes: “normal” one and “activated” (Moffitt *et al.*, 2015). The activated stroma is characterised by the expression of inflammatory cytokines, and it is associated with the basal-like phenotype, whilst the normal one is characterised by expression of markers of pancreatic stellate cells (PSCs) (Moffitt *et al.*, 2015). Yet, single-cell RNA sequencing has revealed that the tumour microenvironment (TME) appears to be as diverse as the tumour cells, themselves (Peng *et al.*, 2019; Raghavan *et al.*, 2021). Thus, due to its heterogeneity it can play both a tumour promoting or tumour restrictive role. There are several important cell types that contribute to the TME.

Cancer-associated fibroblasts (CAFs)

The main player in the TME are CAFs (Murakami *et al.*, 2019). CAFs produce extracellular matrix (ECM) proteins, largely contributing to the desmoplastic reaction (Tian *et al.*, 2019; Sperb, Tsesmelis and Wirth, 2020). They also produce ligands, which can promote tumour progression, such as TGF β 1, which drive tumour cells proliferation and it is consistent with the increased TGF β signalling in basal-like tumours (Ligorio *et al.*, 2019).

CAFs can arise from activated PSCs (in response to insult), from tissue-resident fibroblasts or from fibroblasts, recruited to the tumour (Öhlund, Elyada and Tuveson, 2014; Sperb, Tsesmelis and Wirth, 2020; Gorchs and Kaipe, 2021). Previously, CAFs have been associated with worse disease as the ECM proteins they produce have been considered a physical barrier to drug delivery (Olive *et al.*, 2009; Erkan *et al.*, 2012). Indeed, initial studies in animal models showed CAF depletion, combined with chemotherapy promoted better vascularisation and drug delivery (Olive *et al.*, 2009; Provenzano *et al.*, 2012). However, in clinical trials CAF-depleting agents failed to show any benefits and paradoxically induced worse disease (Kim *et al.*, 2014; Ko *et al.*, 2016). Further studies in preclinical mouse models confirmed that long-term CAF depletion resulted in poorly differentiated tumours and reduced survival (Özdemir *et al.*, 2014; Rhim *et al.*, 2014). In summary, the influence of CAFs on the tumour is complex and it might be due to the presence of different CAF subtypes, that can promote or restrict tumours. Recently, distinct CAF subpopulations have been found to exist (Öhlund *et al.*, 2017; Elyada *et al.*, 2019). Two types of CAFs have emerged: inflammatory (iCAF), which express inflammatory interleukins, and myofibroblast CAFs (myCAFs), which express α SMA (Figure 5; (Öhlund *et al.*, 2017; Biffi *et al.*, 2019; Bhattacharjee *et al.*, 2021). iCAFs are considered tumour-promoting and are located away from neoplastic cells (Öhlund *et al.*, 2017; Biffi *et al.*, 2019). myCAFs, on the other hand, are located more closely to the tumour and can be both pro- and anti-tumorigenic (Öhlund, Elyada and Tuveson, 2014; Biffi *et al.*, 2019; Bhattacharjee *et al.*, 2021). Their production of hyaluronan seems to promote cancer proliferation, whilst their secretion of type I collagen suppresses it

(Bhattacharjee *et al.*, 2021; Chen *et al.*, 2021). Most recently, a new type of antigen presenting CAFs has been identified based on their ability to activate CD4+ T cells (Elyada *et al.*, 2019). Finally, the tumour cells themselves can also influence the subtypes of CAFs as the secretome of basal-like PDACs can induce an iCAF state, underlying the importance of the reciprocal tumour-stroma crosstalk (Somerville *et al.*, 2020).

Endothelial cells

PDAC is considered a hypoxic and poorly vascularised tumour (Figure 5; Zhang *et al.*, 2018). The hypoxic conditions have been shown to promote tumour angiogenesis, proliferation, and metastases (Zhang *et al.*, 2018). Moreover, endothelial cells have been found to promote and support cancer initiating cells (Choi *et al.*, 2021). However, the role of endothelial cells in the TME might be more complex as initially anticipated as vascular remodelling has been shown to improve delivery of therapies (Ruscetti *et al.*, 2020).

Immune cells

Tumour-associated macrophages (TAMs) and tumour-associated neutrophils (TANs) are the main immune cell types, found in the PDAC TME (Figure 5; Jin, Kim and Shi, 2021; Yang, Liu and Liao, 2021). TAMs can be recruited by cancer cells or resident macrophages can serve as their precursor (Yang, Liu and Liao, 2021). On the other hand, TANs are normally recruited by the cancer cells via CXC chemokines' release (Hosoi *et al.*, 2009; Steele *et al.*, 2016; Nywening *et al.*, 2018). Both TAMs and TANs are particularly important in promoting metastatic disease and establishing an immunosuppressive environment, rendering PDAC an "immunologically cold tumour" (Stromnes *et al.*, 2014; Habtezion, Edderkaoui and Pandol, 2016; Lianyuan *et al.*, 2020). Moreover, high TAM infiltration is a marker of poor prognosis (Hu *et al.*, 2016). In line with this, TAMs and TANs depletion reduces metastatic incidence and improves response to chemo- and immune-therapies respectively (Chao, Furth and Vonderheide, 2016; Steele *et al.*, 2016; Buchholz *et al.*, 2020; Nielsen *et al.*, 2021). Additionally, they also influence PDAC subtypes as removing TAMs in tumours shows reduction of basal-like/squamous

programmes whilst TAN depletion leads to a switch to the classical subtype (Steele *et al.*, 2016; Candido *et al.*, 2018). TAMs, just like CAFs and neoplastic cells have also been subtyped into three populations: monocyte-like, phagocytic (basal-like associated), and angiogenesis-associated (classical associated) (Raghavan *et al.*, 2021). However, no classification currently exists regarding TAN subtypes.

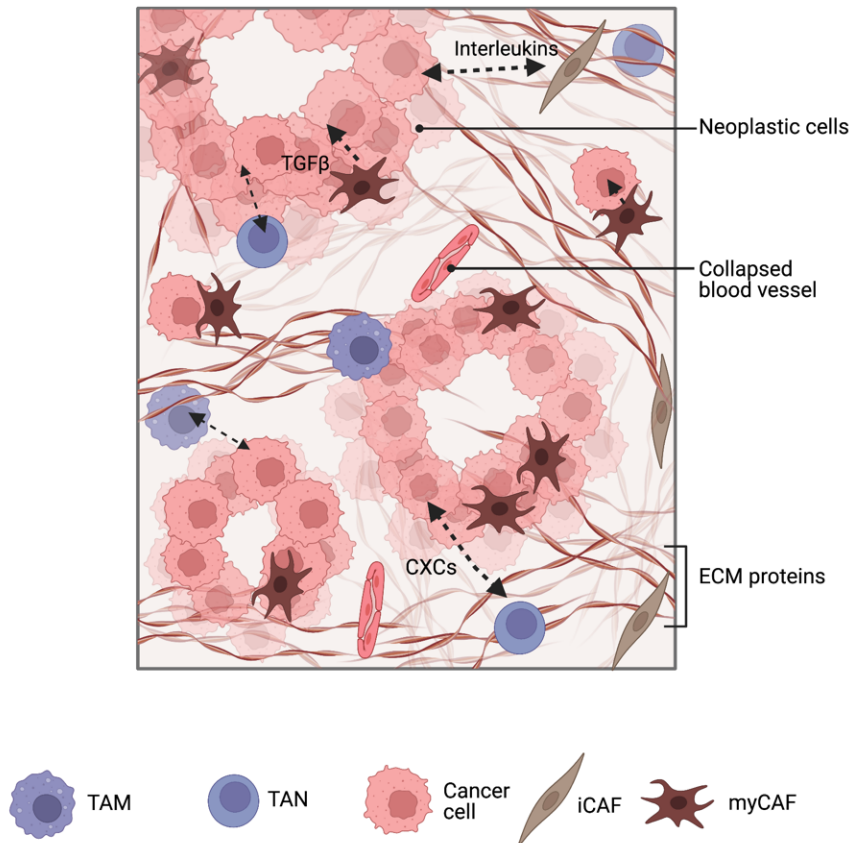


Figure 5. Tumour-stroma crosstalk. Dashed arrows indicate chemokines release. Created with BioRender.com.

1.3.6. *In vitro* preclinical PDAC models

PDAC *in vitro* models can generally be divided into two classes: 2D monolayer cultures (cell lines) and 3D models (organoids). Cell lines can be established from tumour resections, and they have been a valuable tool in elucidating tumour biology (Suri, Zimmerman and Burkhart, 2020). They can be cultured quickly and are also easy to manipulate genetically (Suri, Zimmerman and Burkhart, 2020). Despite their advantages, however, cell lines suffer from several drawbacks. The culture

conditions select for only certain cell populations, inducing loss of heterogeneity. Finally, 2D cultures do not allow for modelling the tumour-stroma crosstalk, which plays a crucial role in PDAC (Suri, Zimmerman and Burkhart, 2020).

More recently, 3D organoids have emerged as an alternative to cell lines. Organoids are a 3D culture system, where epithelial cells can be cultured in a semi-solid medium supplemented with growth factors and morphogens that collectively recreate the *in vivo* stromal niche (Drost and Clevers, 2018; Seino et al., 2018). Organoids can be derived directly from adult primary cells, either from healthy or diseased pancreases, or from human pluripotent stem cells (iPSCs) permitting expansion of the epithelial compartment even from limited amount of material. Organoids have been shown to preserve better the histological and genetic features of the parental tumours (Weeber *et al.*, 2015; Baker *et al.*, 2016). Patient-derived organoids (PDOs) provide a powerful platform to study both cell-autonomous processes and tumour-stroma interactions. The media, which is thoughtfully supplemented with ligands and growth factors, aims to recreate the secretome of the microenvironment. Additionally, because of their 3D structure, organoids allow for co-culturing of cancer cells with other cell types. One type of co-culturing system that has emerged in recent years is organ-on-a-chip. Organ-on-chips are small microfluidic devices with multiple channels, in which different cell types can be cultured (Leung *et al.*, 2022). Organ-on-chips allow for cell-cell interaction by exchanging signalling molecules, and importantly reproduce the flow and shear stress, experienced by cells *in vivo* (Leung *et al.*, 2022). In summary, 3D organoids present a superior model to 2D cell lines, as they recreate the human heterogeneity and allow for studying both cell-autonomous survival mechanisms (due to organoids being 100 % neoplastic cells) and tumour-stroma crosstalk (due to their ability to be co-cultured).

1.4. Aims

PDAC is an extremely heterogenous and resilient disease, whose phenotype can be impacted by changes in the microenvironment. Modelling how PDACs overcome microenvironmental pressures in a human setting, and identifying new tumour-stroma interactions could help elucidate targetable mechanisms of progression.

Pharmacological treatment is a microenvironmental challenge to which cancer cells are exposed. To identify cancer-specific molecular attributes associated with chemotherapy treatment, we performed an integrated genetic and transcriptomic analysis of PDOs established from either treatment-naïve or post-treatment tumours (Chapter 2).

Neoplastic cells are capable of reprogramming non-malignant stromal cells, which often reciprocate by supplying cancer cells with growth- or survival-promoting signals. A subset of these signals is referred to as stromal niche factors that contribute to tumour maintenance. An often-overlooked component of the PDAC tumour microenvironment are endothelial cells, which share phenotypes and functions with other mesenchymal-derived cells, namely fibroblasts. Therefore, we explored here the potential role of endothelial cells as source of mesenchymal niche factors that promote tumour survival in an *ex vivo* setting (Chapter 3). To this end, we used organ-on-a-chip co-culturing system of endothelial cells and PDOs. Microfluidic devices allow for endothelial cells to form “tubes” mirroring the *in vivo* blood vessels and allowing us to study the cancer-endothelium interaction in an anatomical setting.

Finally, we explored the emerging role of ecDNAs and how they drive heterogeneity and survival to microenvironmental selection pressures (Chapter 4). We exploited the niche dependency identified in Chapter 3 to impose an artificial selective pressure on PDOs to model the dynamics of ecDNAs under microenvironmental stress in PDAC. We explored how the environment influences ecDNAs and how their accumulation in turn influences PDACs phenotype.

2. Establishment of PDOs from post-treatment tumours

Antonia Malinova^{1*}, Francesco Pezzini^{1*}, Silvia Andreani², Borislav Rusev², Sonia Grimaldi², Aldo Scarpa^{2,3}, Rita Lawlor^{1,2}, Roberto Salvia⁴ & Vincenzo Corbo^{1,2}

¹Department of Engineering for Innovation Medicine, University of Verona, Verona, Italy

²ARC-Net Research Centre, University of Verona, Verona, Italy

³Department of Diagnostics and Public Health, University of Verona, Verona, Italy

⁴Department of General and Pancreatic Surgery, The Pancreas Institute, University of Verona, Verona, Italy

*Equal contribution

2.1. Introduction

Most PDAC patients (resectable and non-resectable) are offered chemotherapy as a standard of care (Principe *et al.*, 2021). The most widely used drug is gemcitabine, a cytidine analogue, which is converted by the cancer cells into active triphosphorylated nucleotides, interfering with DNA synthesis (Ciccolini *et al.*, 2016; Principe *et al.*, 2021). Gemcitabine is also often prescribed with albumin bound (Nab) Paclitaxel (also known as Abraxane), which affects the cancer cells' microtubular network, and together with gemcitabine improves survival compared to gemcitabine alone (Gradishar, 2006; Von Hoff *et al.*, 2013; Principe *et al.*, 2021). More recently, the multi-drug regimen 5-Fluorouracil, Leucovorin, Irinotecan, and Oxaliplatin (FOLFIRINOX) has been approved for both metastatic and non-metastatic PDAC, however FOLFIRINOX also induces more severe side effects than other therapies (Conroy *et al.*, 2018; Principe *et al.*, 2021). Finally, radiation therapy is also increasingly used, as there are now newer techniques, which minimise non-tumour tissues exposure to radiation (Chapman *et al.*, 2018).

Most of the above-mentioned therapy regimens, however, do not significantly improve survival rates. In fact, PDAC is characterised by being extremely refractory to standard chemotherapy and by high relapse rates. Recently, there has been a trend for administration of neoadjuvant therapy, i.e., administering

chemotherapy before surgery (Oba *et al.*, 2020). Therefore, there is an increase interest in establishing *in vitro* models, which are derived from post-treatment tumours, to understand how chemotherapy impacts the biology of the cancer and indicate targetable determinants of resistance and relapse.

In this preliminary study, we established a library of PDOs from treatment-naïve and from treated patients and characterised them by whole-exome sequencing (WES) and bulk RNA sequencing. We found no significant genetic differences between PDOs from treated and non-treated patients. However, PDOs from treated patients showed enrichment for proliferation and epigenetic regulation pathways.

2.2. Materials and methods

Human specimens and clinical data

PDAC tissues were obtained from the General and Pancreatic Surgery Unit at University of Verona. Written informed consent was obtained from patients preceding the acquisition of the specimens. The fresh tissues used to establish PDOs were collected under a study approved by the Integrated University Hospital Trust (AOUI) Ethics Committee (Comitato Etico Azienda Ospedaliera Universitaria Integrata): approval number 1911 (Prot. n 61413, Prog 1911 on 19/09/2018). Formalin-fixed and paraffin-embedded tissues were collected under the protocol number 1885 approved by the AOUI Ethics Committee and retrieved from the ARC-NET Biobank.

PDOs

PDOs were established using previously published procedures (Boj *et al.*, 2015). Briefly, tumour tissue, identified by a pathologist, was digested in 5 mg/ml Collagenase II (Gibco), Dispase I 1.25 mg/ml (Gibco), and 10.5 μ M Y-27632 (Sigma), all diluted in human splitting medium (HSM, Table 1) at 37°C for a maximum of two hours. Afterwards, tissue was further digested for 15 minutes at 37°C using TrypLE (Gibco). Digested cells were then embedded in growth factor reduced Matrigel® (Corning) and overlaid with human complete media (HCM, Table 2). Media were changed every 3-4 days and PDOs were expanded in these conditions. PDOs were kept in a humidified incubator at 37°C and 5 % CO₂ and

routinely tested for *Mycoplasma* contamination using Mycoalert Mycoplasma Detection Kit (Lonza). Upon establishment, quality check (QC) was performed in the form of a thaw check. Two weeks after freezing, PDOs were thawed and if they were able to recover, the model passed QC.

Table 1. HSM medium components. All components were diluted in Advanced Dulbecco's Modified Eagles Medium with Nutrient Mixture F-12 Hams (Gibco).

Component	Concentration
HEPES (Gibco)	10 mM
Glutamax™ (Gibco)	2 mM
Primocin™ (Invivogen)	1 mg/ml

Table 2. Components of human complete media (HCM). All components were diluted in HSM (Table 1).

Component	HCM
B-27 Supplement (Gibco)	1x
Nicotinamide (Sigma-Aldrich)	10 mM
N-Acetylcysteine (Sigma-Aldrich)	1.25 mM
Mouse Epidermal Growth Factor (Gibco)	50 ng/ml
FGF10 (Peprotech)	100 ng/ml
Y-27632 Dihydrochloride (Sigma)	10.5 μ M
Gastrin (Tocris)	10 nM
WNT3A Conditioned media	50 % V/V
RSPO1 Conditioned media	10 % V/V
TGF β Receptor inhibitor A83-01 (Tocris)	500 nM
mNoggin (Peprotech)	100 ng/ml

DNA and RNA isolation

PDOs were removed from Matrigel® via incubation in Cell Recovery Solution (Corning) for 30 minutes at 4°C and washed in HSM and phosphate-buffered saline 1x (PBS, Gibco). Afterwards, PDOs were pelleted by centrifuging 10,000 g at 4°C. DNA from PDOs and corresponding normal tissue were extracted using DNA

Quiagen DNeasy Blood & Tissue Kit according to the manufacturer's instructions. RNA was isolated using PureLink RNA Mini Kit (Thermo Fisher Scientific) according to the manufacturer's instructions.

Whole Exome Sequencing (WES)

The quality of DNA was assessed using DNF-467 Genomic DNA 50 kb Kit on a Bioanalyzer 2100 (Agilent). Sequencing libraries were prepared from 50 ng DNA using the Twist Library Preparation EF Kit 2.0 (Twist Bioscience) and Twist Comprehensive Exome probe panel (catalogue numbers: 104207, 103698, and 101308/09/10/11, Twist Bioscience) with unique dual indexes according to manufacturer's instructions. Sequencing was performed on a NovaSeq 6000 platform, S4 flow cell and v1.5 sequencing chemistry with paired end reads of 150 base pairs, at 20x coverage 160 million reads per sample.

WES processing, mutational calling, and CNV analysis

We applied a standard WES pre-processing pipeline: briefly, after quality checking and trimming with fastqc (<https://www.bioinformatics.babraham.ac.uk/projects/fastqc/>) and fastp (Chen et al., 2018), data were aligned to the GRCh38 genome build with BWA (Li and Durbin, 2009). Sequenced reads were then sorted and indexed, and duplicates marked with sambamba (Tarasov *et al.*, 2015). Next, recalibration and mutation calls were performed with gatk Mutect2 (Depristo *et al.*, 2011). Mutations were annotated with snpEffect (Cingolani *et al.*, 2012) and files were converted to maf format with the tool vcf2maf (Kandoth *et al.*, 2018). Downstream analysis was performed mainly through the bioconductor library maftools (Mayakonda *et al.*, 2018), mutational signatures were extracted with MuSiCa (Díaz-Gay *et al.*, 2018), and copy number variations were determined using the software tools sequenza (Favero *et al.*, 2015) and gistic2 (Mermel *et al.*, 2011).

RNA sequencing

The quality of RNA was assessed using RNA 6000 Nano kit on a Bioanalyzer 2100 (Agilent) and all samples used had RIN values of more than nine. Libraries were

prepared using Illumina TruSeq Stranded Total RNA sample Prep Kit and sequenced on a NovaSeq 6000 platform, S4 flow cell with paired end reads of 150 bases with a final coverage of 80 - 100 million reads per sample.

RNA Sequencing data processing, molecular subtyping, differential expression (DEG), and pathway analyses

Data were quality checked and trimmed with fastqc (<https://www.bioinformatics.babraham.ac.uk/projects/fastqc/>) and fastp (Chen *et al.*, 2018). Then, reads were aligned to the GRCh38 genome build and quantified using Salmon v1.4.0 (Patro *et al.*, 2017). Next, transcripts quantification was imported in R with the tximport package v4.0 (Soneson, Love and Robinson, 2016). Differentially expression analysis was performed using DESeq2 (Michael I. Love, Huber and Anders, 2014). Gene set enrichment analysis (GSEA) was performed with *fgsea* R package v1.16.0 (Kuleshov *et al.*, 2016) using the list of differentially expressed genes sorted by log2 of fold change. The pathways considered came from Gene Ontology, KEGG, Biocarta, Reactome, and Hallmark gene sets. GSVA R package v1.38.2 (Hänzelmann, Castelo and Guinney, 2013) was used to calculate the main PDAC transcriptomic subtypes (Moffitt *et al.*, 2015; Peter Bailey *et al.*, 2016) gene set scores. *Gsva* function was used with *ssgsea* and gene set scores were compared among untreated and treated samples with a Wilcoxon rank-sum test.

Immunohistochemistry

Immunohistochemistry staining was performed on sections of formalin-fixed, paraffin-embedded tissues, following established procedures using the reported primary antibody: β -catenin (Sigma-Aldrich, clone 15B8). The slides were then scanned and digitalised using the Aperio Scan-Scope XT Slide Scanner (Aperio Technologies).

2.3. Results

Overview of established PDOs

We received a total of 27 patient samples from the pancreatic surgery of the Università di Verona Borgo Roma hospital (Table 3). Out of those samples, 17 came

from treatment-naïve patients, whilst 10 came from patients with administered neoadjuvant therapy (Figure 1A). The most common neoadjuvant therapy was FOLFIRINOX (n = 6), followed by Gemcitabine/Nab-paclitaxel (n = 3). We established 12 PDOs in total, made up of models from six treated and six non-treated tumours (Figure 1A). After PDOs' establishment, quality control (QC) check was performed on all models. QC consisted of a thaw-check to see if models could recover after freezing and thawing. The main reason for failure of establishment was lack of outgrowth of tumour cells in culture, however four models also failed due to fungal contamination (Table 3). There was no enrichment for failures of PDOs establishment from pre-treated tumours or from rare histology types: only two cases that failed came from adeno squamous PDACs and four from pre-treated patients (Table 3). On the other hand, we established PDOs from three PDACs with squamous or adeno-squamous elements, and one clear cell carcinoma (Figure 1B). In terms of treatment, PDOs came from patients treated with FOLFIRINOX (n = 4), nITRO (n = 1), and Gemcitabine/Nab-paclitaxel (Abraxane) (n = 1). In summary, we established 12 PDOs from patients that had undergone neoadjuvant therapy (n = 6), as well as from patients with rare histology subtypes (n = 3).

Table 3. Patient characteristics for all samples collected. Established PDOs are indicated. F/M: female/male; Y/N: yes/no. DoB: date of birth.

ID	Sex (F/M)	DoB	Histological diagnosis	Post-treatment (Y/N)	Type of treatment	T	N	M	Staging	Established PDO (Y/N)	Failure reason
VR_P101_1	F	1941	PDAC	Y	Gemcitabine/Nab-Paclitaxel	T3	N1	M0	IIB	N	No outgrowth of tumour cells
VR_P102_1	M	1954	PDAC	N	N/A	T2	N2	M0	III	N	No outgrowth of tumour cells
VR_P103_1	M	1944	PDAC	N	N/A	T1	N2	M1	IV	N	No outgrowth of tumour cells
VR_P104_1	M	1967	PDAC	Y	FOLFIRINOX	T2	N2	M0	III	N	No outgrowth of tumour cells
VR_P105_1	F	1948	PDAC	N	N/A	T2	N0	M0	IB	N	No outgrowth of tumour cells
VR_P106_1	M	1948	PDAC	N	N/A	T2	N2	M0	III	N	No outgrowth of tumour cells
VR_P107_1	F	1950	PDAC	Y	Gemcitabine/Nab-Paclitaxel	T2	N1	M0	IIB	N	No outgrowth of tumour cells
VR_P108_1	M	1954	PDAC with squamous cells features	N	N/A	T2	N2	M0	III	N	No outgrowth of tumour cells
VR_P109_1	F	1941	Squamous adenocarcinoma	N	N/A	T2	N2	M0	III	N	No outgrowth of tumour cells
VR_P110_1	F	1964	PDAC	N	N/A	T2	N2	M0	III	N	No outgrowth of tumour cells
VR_P111_1	M	1943	PDAC	N	N/A	T2	N2	M0	III	N	Contamination
VR_P112_1	F	1948	PDAC	N	N/A	T2	N0	M0	IB	N	Contamination
VR_P113_1	M	1961	PDAC	N	N/A	T2	N2	M0	III	N	Contamination
VR_P114_1	M	1964	PDAC	Y	FOLFIRINOX 10 cycles	T4	N1	M0	III	N	Contamination
VR_P115_1	F	1946	PDAC	N	N/A	T4	N2	M0	III	N	No outgrowth of tumour cells
VR_P088_1	F	1935	PDAC	N	N/A	T3	N2	M0	III	Y	N/A
VR_P089_1	M	1951	Adenosquamous carcinoma (Signet)	N	N/A	T3	N1	M0	IIB	Y	N/A
VR_P090_1	M	1955	PDAC	Y	FOLFIRINOX 12 cycles (+ radiation)	T2	N2	M0	III	Y	N/A
VR_P091_1	F	1956	PDAC	Y	Gemcitabine/Nab-Paclitaxel	T4	N2	M0	III	Y	N/A
VR_P092_1	M	1947	PDAC	Y	FOLFIRINOX 6 cycles	T3	N2	M0	III	Y	N/A
VR_P093_1	M	1978	PDAC	N	N/A	T2	N2	M0	III	Y	N/A
VR_P094_1	M	1974	PDAC	N	N/A	T2	N2	M1	IV	Y	N/A
VR_P095_1	M	1971	Adenosquamous carcinoma	N	N/A	T2	N1	M0	IIB	Y	N/A
VR_P096_1	M	1949	Clear cell carcinoma	Y	FOLFIRINOX 10 cycles	T1c	N0	M0	IA	Y	N/A
VR_P097_1	F	1964	PDAC	Y	FOLFIRINOX (12 cycles)+radiation	T2	N2	M0	III	Y	N/A
VR_P098_1	M	1974	PDAC (poorly differentiated)	Y	Protocol nITRO (nITRO: nal-IRI/5-FU/LV and oxaliplatin)	T2	N2	M0	III	Y	N/A

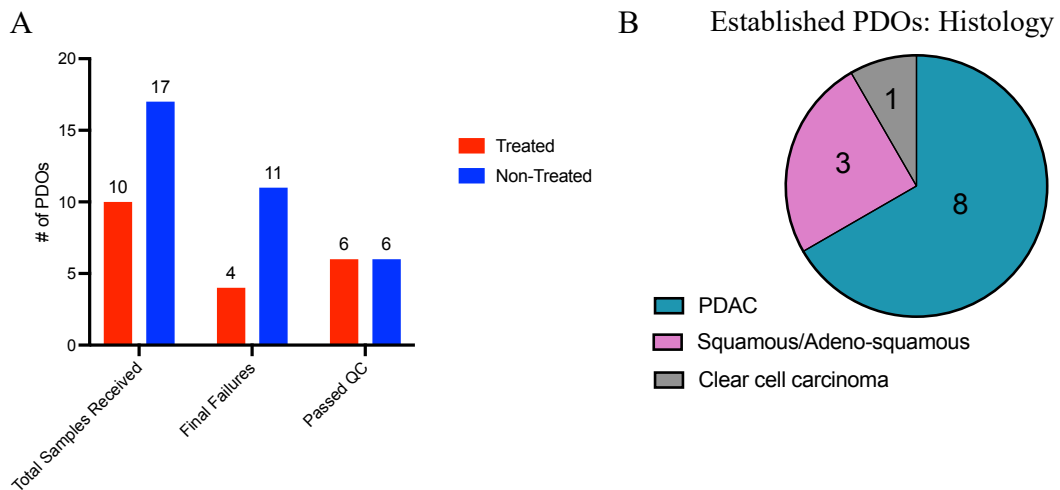


Figure 1. Overview of sample characteristics. **A.** Bar graph showing an overview of the characteristics of all samples received from which PDOs establishment was attempted. Number of total samples is indicated above each bar. **B.** Pie chart summarising the histological characteristics of the patient samples, from which PDOs were established.

Genetic characterisation of PDOs

To genetically characterise PDOs and to understand if there are any genetically driven differences between PDOs from treatment-naïve and post-treatment tumours, we performed WES on PDOs and matched normal tissues. We looked for both mutations and copy-number changes. To understand the copy-number landscape, gains and losses were defined using the COSMIC definition (Tate *et al.*, 2019). A gain was defined as when the average ploidy was less or equal to 2.7 and the total copy-number was bigger or equal to 5, or when the average ploidy was bigger than 2.7 and the total copy-number was bigger or equal to 9. A loss was defined when the average ploidy was less or equal to 2.7 and the total copy-number was 0 or when the average ploidy higher than 2.7 and the total copy-number was less than the average ploidy -2.7 (Tate *et al.*, 2019).

We first explored the differences between groups in terms of mutational and copy number burdens (Figures 2A and 2B). The average mutational burden for PDOs from both treated and non-treated tumours was 2 and there were no statistically significant differences (Figure 2A). This is consistent with data from human PDACs, showing that majority of tumours have a low mutational burden (< 10)

(Alexandrov *et al.*, 2013; Quintanilha *et al.*, 2023). There were also no statistically significant differences in the copy number burden (Figure 2B).

We then looked at specific mutations and copy-number alterations. We did not notice any significant differences between oncogenes in PDOs from treatment naïve and pre-treated tumours. However, *RNF43* mutations were exclusive to the post-treatment cohort (n = 3) (Figure 2C). All models (treated and post-treated) contained at least one oncogenic mutation either in *KRAS* or *GNAS* and inactivating mutations in *TP53* (n = 11; Figure 2C). One model (VR-P097-01) contained an activating mutation in *GNAS* and a frameshift insertion in *RNF43*, instead (Figure 2C). However, *CDKN2A* was also inactivated in this model due to a copy number loss (Figure 2C). *GNAS* and *RNF43* mutations are particularly characteristic of PDACs arising from IPMNs (Chang *et al.*, 2020). Another interesting case was VR-P094-01, which contained an activating mutation in *CTNNB1* (S45Y), in addition to mutations in *KRAS* and *TP53* (Figure 2C). Mutations in the WNT/ β -catenin pathway are uncommon in PDAC and are more characteristic of rarer pancreatic cancers, such as acinar cell carcinomas or pancreatoblastomas (Abraham *et al.*, 2001, 2002; Jones, Zhang, Williams Parsons, *et al.*, 2008; Witkiewicz *et al.*, 2015; Peter Bailey *et al.*, 2016). We performed immunohistochemistry for β -catenin on the patient tissue and confirmed it was translocated in the nucleus, suggesting aberrant activation of the pathway (Figure S1).

Late-stage and metastatic tumours can often harbour copy number alterations, such as gains of oncogenes (e.g.: *KRAS* or *MYC*) (Mueller *et al.*, 2018; Sodir *et al.*, 2020). Only treatment naïve PDOs showed true gains of *MYC* and *KRAS* (Figure 2C). We also looked at genes that encode cyclin-dependant kinases (e.g.: *CDKI*) as their overactivation drives cell cycle, tumour progression and initiation (Ghafouri-Fard *et al.*, 2022). We found no gains of cyclin-dependant kinases, however only post-treatment tumours contained gains for *CCND1* and *CCND3* (Figure 2C). Finally, VR-P089-01, a PDO from a treatment-naïve tumour, was a particularly interesting case as it harboured multiple gains in *KRAS*, *MYC*, cyclin and cyclin-dependant kinases genes, as well as a gain of *CYP3A5*, a mediator of therapy resistance and the basal-like PDAC subtype (Noll *et al.*, 2016). These observations were in line with the adeno-squamous histology of the patient tumour (Table 3).

Lastly, we looked at somatic and germline mutations in the BRCA-mediated DNA damage repair pathway. These mutations are rare in PDAC, but patients with these alterations have been shown to benefit from platinum therapy (Lowery *et al.*, 2018). Our cohort contained two models that harboured germline mutations. VR-P096-01 had a mutation in *BRCA2* (60 % variant allele frequency (VAF)), whilst VR-P093-01 had a mutation in *RAD50* (49 % VAF) (Figure 2D). Our cohort also contained a sample (VR-P100-01) with a somatic *BRCA2* mutation, but with a very low VAF (2 %) (Figure 2D). We characterised the mutational signatures in our cohort and found that the *BRCA* mutational signature (COSMIC signature 3) contributed to a various degree in four PDOs (Figure 2E). Despite the low VAF of the somatic *BRCA2* mutation in VR-100-01, COSMIC signature 3 contributed 40.5 % to the overall mutational burden of the PDO (Figure 2E). The model did not contain any other mutations in BRCA-mediating genes; however, the high contribution of this mutational signature could also be explained by the fact that VR-P100-01 had the highest mutational burden out of all models (3.5 mutations/megabase). In VR-P093-01, COSMIC signature 3 contributed 7.1 % to the overall mutational burden, and there was no contribution of the same signature to VR-P096-01, indicating that in these cases the clinical significance of the germline BRCA mutations was low. Finally, we found a contribution of 27.2 % to VR-P095-01, a PDO without BRCA-associated mutations (Figure 2E). VR-P095-01 was had the second highest mutational burden in our cohort (Figure 2C), suggesting defects in DNA-damage repair mechanisms.

Overall, our results align with the previously reported genetic landscape of PDAC (Waddell *et al.*, 2015). We did not observe any significant genetic differences between PDOs from treated and non-treated tumours, however we PDOs from chemo-treated tumours were enriched for inactivation of *RNF43* and gains of *CCND1/3*.

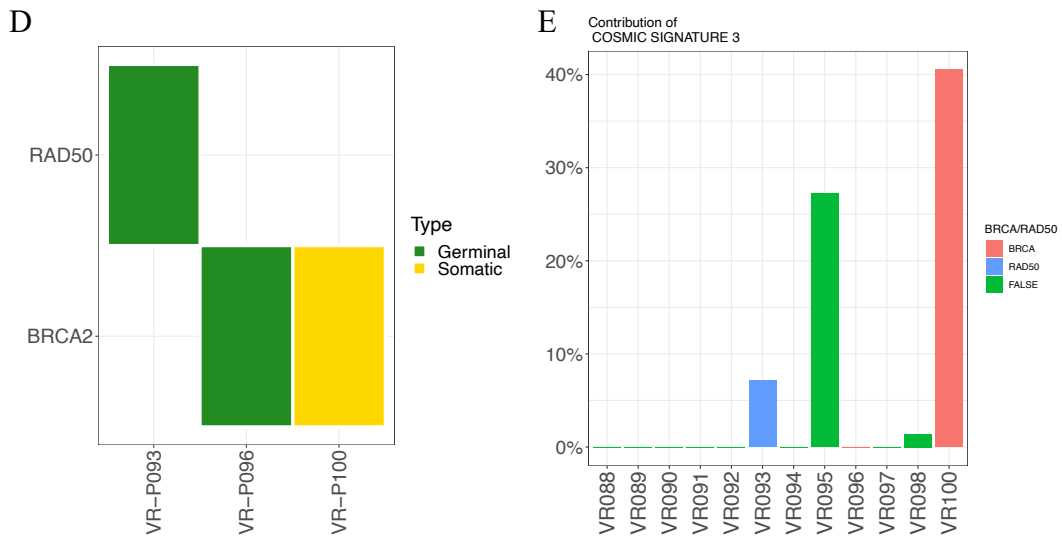


Figure 2. Genetic characterisation of PDOs' cohort. **A.** Box plot showing tumour mutational burden as mutations per mega base of PDOs from treated and post-treated tumours. **B.** Box plot showing tumour copy number variation (CNV), as a percent of the autosomal tumour genome bearing CNVs, in PDOs from treated and post-treat tumours. **C.** Oncoplot showing somatic mutations and copy-number gains and losses in main oncogenes in PDOs from treated and post-treat tumours (Y: Yes. N: No). **D.** Oncoplot showing the presence of germline and somatic mutations in genes of the BRCA pathway in three PDOs. **E.** Bar plot showing the contribution of BRCA mutational signature (COSMIC SIGNATURE 3) as a percentage out of the total mutational burden of established PDOs. FALSE means no mutations in the BRCA pathway.

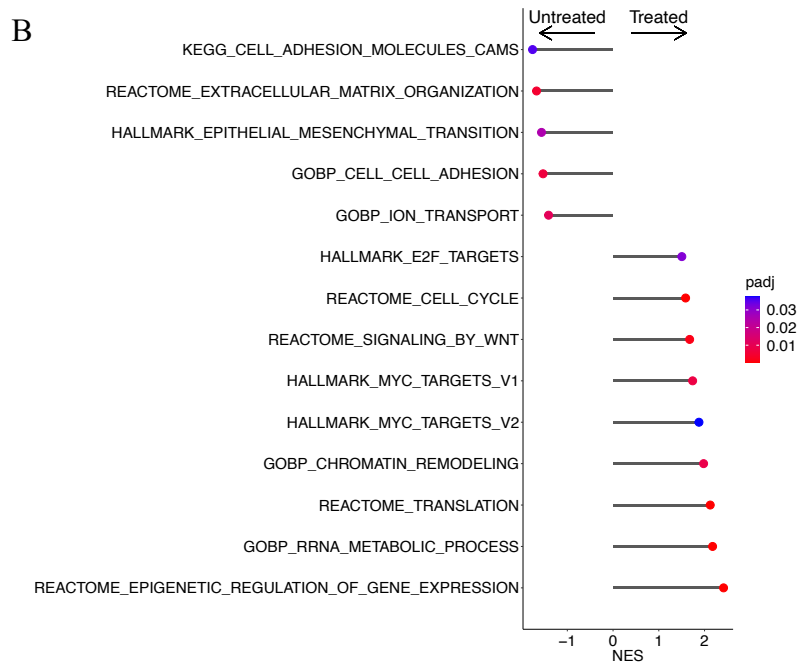
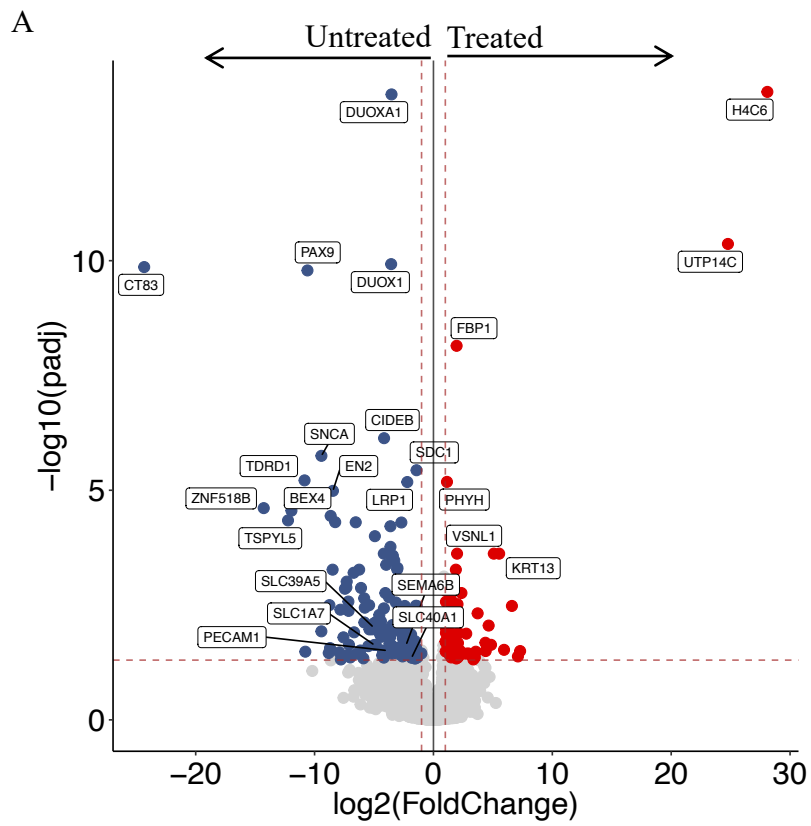
PDOs from post-treated tumours show features of more advanced disease

We performed bulk RNA sequencing on nine PDOs, five from treatment naïve tumours (VR-P088-01, VR-P093-01, VR-P094-01, VR-P095-01, and VR-P100-01) and four from post treatment ones (VR-P090-01, VR-P091-01, VR-P096-01, and VR-P098-01). Interestingly, PDOs from post-treatment tumours upregulated *H4C6*, a histone encoding gene (Figure 3A). Accordingly, these PDOs were also enriched for chromatin remodelling and epigenetic regulation pathways (Figure 3B). This is in line with evidence that more advanced tumours are enriched for alterations in chromatin remodelling pathways (Peter Bailey *et al.*, 2016). Post-treatment PDOs also showed increased expression of *KRT13*, whose upregulation is associated with radiotherapy resistance in PDAC (Takenaka *et al.*, 2023). Treated PDOs were enriched for *MYC* targets (even though *MYC* gain was observed only in PDOs from treatment naïve tumours), cell cycle, and E2F targets, suggesting they are more

proliferative (Figure 3B). Additionally, *MYC* has been shown to be upregulated in advanced PDACs (Witkiewicz *et al.*, 2015; Brar *et al.*, 2019). Finally, despite no significant differences in CNV burden derived from WES, treated PDOs were enriched for CIN70, a signature, associated with chromosomal instability and worse patient outcome (Figure 3D) (Carter *et al.*, 2006).

PDOs from treatment-naïve patients showed upregulation of *PECAMI*, which is normally a marker of endothelial cells (Figure 3A) (van Mourik *et al.*, 1985). Upregulation of *PECAMI* in PDAC is associated with increased vascularity and better survival (Katsuta *et al.*, 2019). Non-treated PDOs were also enriched for pathways, associated with cell adhesion and ion transport (Figure 3B). Surprisingly, non-treated PDOs showed upregulation of the epithelial-mesenchymal transition (EMT), which is normally associated with advanced disease (Figure 3B) (Peter Bailey *et al.*, 2016). This could be because the non-treated cohort included two PDOs from patients with adeno-squamous histology. Finally, PDOs from non-treated tumours were enriched for the pancreatic-progenitor molecular subtype, associated with slightly better survival rates (Figure 3C; Bailey *et al.*, 2016b). Overall, our results suggest that PDOs from post-treated tumours show a transcriptional phenotype of more advanced disease.

PDOs from post-treatment tumours also showed enrichment for WNT pathway signalling (Figure 3B). As shown by WES, PDOs from that group were also enriched for *RNF43* mutations. To understand if these genetic events were contributing to the phenotype, we performed pathway enrichment analysis, excluding those cases (VR-P091 and VR-P096), and excluding the PDO with *CTNNB1* mutation (VR-P094). Our results were similar to the first analysis, including upregulation of epigenetic pathways and *MYC* targets (Figure 3E). However, there was no upregulation of WNT pathways, suggesting that the *RNF43* mutant cases were contributing to the initial results and the mutations were functionally important.



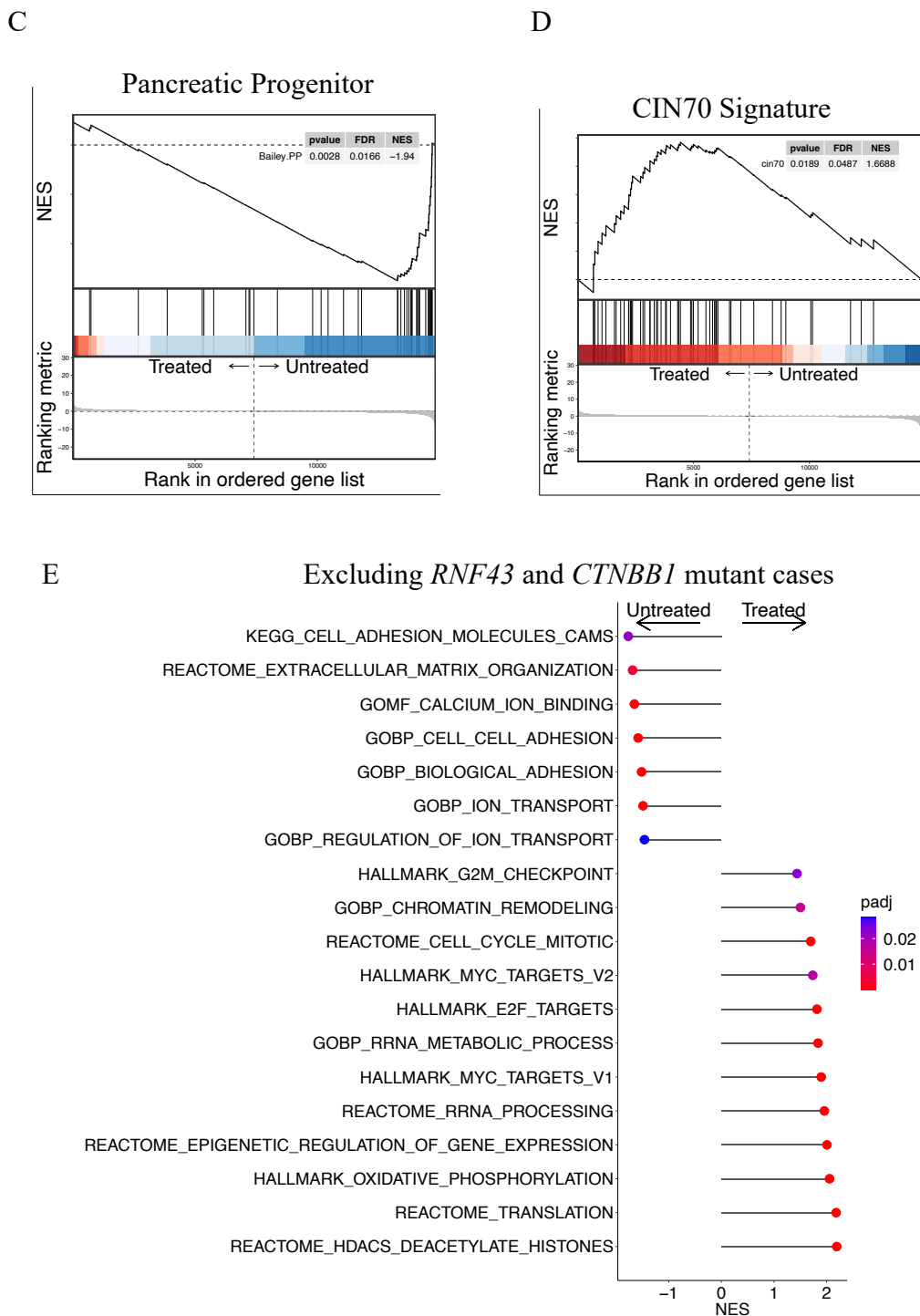


Figure 3. Transcriptional differences between PDOs from treated and non-treated tumours. **A.** Volcano plot showing differentially expressed genes between PDOs from treated tumours (treated) and non-treated (untreated). **B.** Lollipop plot showing pathways enriched in PDOs from treated tumours (treated) and non-treated (untreated). **C.** Gene set enrichment analysis for the pancreatic-progenitor subtype (Peter Bailey *et al.*, 2016) in PDOs from non-treated tumours (untreated). **D.** Gene set enrichment analysis for the CIN70 signature (Carter *et al.*, 2006) in PDOs

from treated tumours (treated). E. Lollipop plot showing pathways enriched in PDOs from treated tumours (treated) and non-treated (untreated), excluding VR-P091, VR-P096, and VR-P094.

2.4. Discussion

In this study, we established a library of 12 PDO models from treated and non-treated tumours. Our cohort also contained models from tumours with adeno-squamous features and from models with germline *BRCA* mutations. Overall, our cohort could provide models of PDACs with rare features.

We focused our analyses to understand if we can find differences between PDOs from treated and from non-treated tumours. We found no significant differences in genetics between the groups, however treated PDOs were enriched for programmes, associated with more advanced tumours. This is in line with previous studies, showing enrichment for the squamous programmes in post-treated PDACs (Hwang *et al.*, 2020). This could be due to the emergence of fitter and more aggressive cancer cells or because patients, undergoing neoadjuvant treatment usually already have more advanced disease. Targeted studies on matched treated and non-treated PDOs are required to understand better how therapy affects the tumour. Additionally, RNA sequencing showed enrichment for epigenetic reprogramming and histone modification programmes. Generally, this is associated with the switch from classical to basal-like subtype. However, all PDOs from adeno-squamous histology subtypes came from the non-treated cohort. This could suggest that the chemotherapeutics are inducing epigenetic, rather than genetic changes. Further, functional studies are required to understand this.

Finally, treated PDOs showed similar oncogene driver mutations to non-treated PDOs, but appeared to be enriched for signatures of chromosomal instability. This is in line with previous reports showing that advanced disease in PDAC is a result of increased chromosomal instability (Chan-Seng-Yue *et al.*, 2020). Additionally, recent work has shown that PDOs from FOLFIRINOX treated patients also harbour similar features (Farshadi *et al.*, 2021).

PDOs from non-treated tumours were enriched for the pancreatic progenitor subtype, however treated PDOs were not enriched for the squamous subtype. This could be because, our treated cohort consisted of different types of neoadjuvant

regimens, which induce different changes, driving higher heterogeneity in the treated cohort. Studies are needed to focus on one type of treatment regimen to understand drug-specific changes. Additionally, we need to understand the drift that PDOs undergo in culture so combinatorial studies are needed on matched patient tissues and established PDOs.

In conclusion, we established a heterogeneous cohort of PDOs from treatment-naïve and pre-treated patients. Despite no mutational differences between the two cohorts, treated PDOs were enriched for chromosomal instability signatures and epigenetic remodelling pathways. Our study provides a library of PDAC organoids that can be used to model specific disease features of both post- and pre-treatment tumours.

2.5. Supplementary data

β -catenin

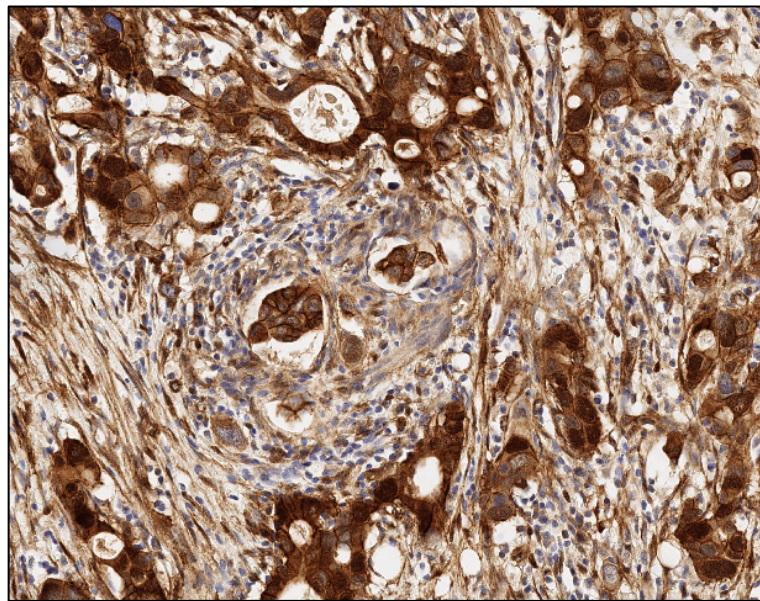


Figure S1. Patient β -catenin translocation. Representative image of immunohistochemistry staining of β -catenin of patient tissue, from which VR-P094-01 was derived.

3. RSPO is an essential stromal cue, provided by CAFs and endothelial cells

Antonia Malinova^{1*}, Elena Fiorini^{1*}, Alma Franceschini¹, Davide Pasini¹, Pietro Delfino¹, Silvia Andreani², Sabrina D'Agosto², Davide Antonello², Aldo Scarpa^{2,3}, Rital Lawlor^{1,2}, Roberto Salvia⁴, Marlene Geyer⁵, Karla Queiroz⁵, & Vincenzo Corbo^{1,2}

¹Department of Engineering for Innovation Medicine, University of Verona, Verona, Italy

²ARC-Net Research Centre, University of Verona, Verona, Italy

³Department of Diagnostics and Public Health, University of Verona, Verona, Italy

⁴Department of General and Pancreatic Surgery, The Pancreas Institute, University of Verona, Verona, Italy

⁵Mimetas B.V., Oegstgeest, Netherlands

*Equal contribution

3.1. Introduction

One of the ways the stroma in PDAC supports cancer cells is by providing growth factors and chemokines (Hessmann *et al.*, 2020). However, as tumours progress, they become less reliant on microenvironmental cues. Indeed, stromal depleting agents in preclinical mouse models and clinical trials have shown poorly differentiated and aggressive tumours (Kim *et al.*, 2014; Özdemir *et al.*, 2014; Rhim *et al.*, 2014). Therefore, it is important to identify the essential cues and their origin, to eventually understand how cancer cells overcome their removal.

In PDOs, the media is rich in cues and growth factors, in an attempt to replicate the TME. Previous studies have found that PDOs that are more reliant on the niche factors WNT and RSPO (WNT pathway activators), associate with the less aggressive classical PDAC subtype (Seino *et al.*, 2018). This shows that PDOs mirror the stromal dependency found in PDACs as progression from WNT/RSPO dependant to WNT/RSPO independent PDOs also associated with progression to more aggressive disease (Seino *et al.*, 2018). In this study, WNT was confirmed to

be derived from CAFs and accordingly, CAFs and PDOs co-culturing in the absence of WNT rescued survival (Seino et al., 2018). However, it remains unclear whether RSPO is a cue provided by CAFs or other cell types in the TME and how it might support cancer cells.

Here, we explored WNT/RSPO niche dependency in a cohort of early-stage disease and treatment-naïve PDOs and found that RSPO, rather than WNT is essential for PDOs survival. Next, we showed that RSPO can be provided by both CAFs and endothelial cells. Finally, we confirmed that endothelial cells support cancer cells via RSPO release by co-culturing of PDOs and endothelial cells in the absence of niche factors supported PDOs growth. Our study presents a previously unknown endothelial niche in the TME.

3.2. Materials and methods

PDOs

All PDAC PDOs were obtained from the Human Cancer Model Initiative (HCMI <https://ocg.cancer.gov/programs/HCMI>) and are available for access from ATCC. Patient data are available on the HCMI searchable catalogue (<https://hcmi-searchable-catalog.nci.nih.gov/>). The corresponding HCMI IDs are listed in Table 1.

Table 1. PDOs' IDs used for experiments with their corresponding HCMI IDs.

ID	HCMI ID
VR01-O	HCM-CSHL-0080-C25
VR02-O	HCM-CSHL-0077-C25
VR06-O	HCM-CSHL-0084-C25
VR20-O	HCM-CSHL-0092-C25
VR23-O	HCM-CSHL-0089-C25
VR29-O	HCM-CSHL-0187-C25
VR30-O	HCM-CSHL-0192-C25
VR31-O	HCM-CSHL-0090-C25
VR32-O	HCM-CSHL-0081-C25

All PDOs were embedded in growth factor reduced Matrigel®, and cultured in human complete medium (+WR, Table 3) in a humidified incubator at 37°C and 5 % CO₂. For the propagation experiments, PDOs were removed from Matrigel®, broken into cell clusters by pipetting, washed in human splitting medium (HSM, Table 2), and resuspended in the appropriate volume of fresh Matrigel® to obtain a splitting ratio of 1:3 every seven days. Post-plating, PDOs were supplemented with the following media, as indicated on the figure legends: human complete media (+WR), media without WNT3A (-W), media without WNT3A and RSPO1 (-WR), media without RSPO1 (+W-R), or HSM media only with RSPO1 (HSM+R). Passaging experiments with recombinant RSPO3 (100 ng/ml, Biotechne) and C59 (100 nM, Selleckchem) were performed in the same splitting ratio. Drugs were added to the media every two days. Organoids were routinely tested for the presence of *Mycoplasma* contamination using Mycoalert Mycoplasma Detection kit (Lonza).

Table 2. HSM medium components. All components were diluted in Advanced Dulbecco's Modified Eagles Medium with Nutrient Mixture F-12 Hams (Gibco).

Component	Concentration
HEPES (Gibco)	10 mM
Glutamax™ (Gibco)	2 mM
Primocin™ (Invivogen)	1 mg/ml

Table 3. Components of human complete media (+WR). All components were diluted in HSM (Table 2).

Component	+WR
B-27 Supplement (Gibco)	1x
Nicotinamide (Sigma-Aldrich)	10 mM
N-Acetylcysteine (Sigma-Aldrich)	1.25 mM
Mouse Epidermal Growth Factor (Gibco)	50 ng/ml
FGF10 (Peprotech)	100 ng/ml
Y-27632 Dihydrochloride (Sigma)	10.5 μM
Gastrin (Tocris)	10 nM
WNT3A Conditioned media	50 % V/V

RSPO1 Conditioned media	10 % V/V
TGF β Receptor inhibitor A83-01 (Tocris)	500 nM
mNoggin (Peprotech)	100 ng/ml

DNA and RNA isolation

PDOs were removed from Matrigel® via incubation in Cell Recovery Solution (Corning) for 30 minutes at 4°C and washed in HSM and phosphate-buffered saline 1x (PBS, Gibco). Afterwards, PDOs were pelleted by centrifuging 10,000 g at 4°C. DNA from PDOs and corresponding normal tissue were extracted using DNA Quiagen DNeasy Blood & Tissue Kit according to manufacturer's instructions. RNA was isolated with TRIzol™ Reagent (Life Technologies) and PureLink RNA Mini Kit (Thermo Fisher Scientific).

PDOs RNA sequencing and subtyping

Libraries were prepared using TrueSeq Standard mRNA Library Prep Kit (Illumina) and sequenced to a depth of 30M fragments and 150 base paired end reads on an Illumina NextSeq 500 sequencer. Quality control and cleaning were performed on raw FastQ files using fastp. Reads were quantified and aligned to GRCh38 genome using standard STAR/RSEM pipeline. Counts were normalised using DESeq2 Bioconductor R package and transformed with the VST function of the same package (Michael I. Love, Huber and Anders, 2014). For PDO subtyping, gsva function was used with classical and basal-like signatures (Moffitt *et al.*, 2015) and subtypes were assigned based on the signature with the higher score.

DNA Panel Sequencing

Library preparation was performed using SureSelectXT HS Target Enrichment System (Agilent). Panel pair-end 2x150 sequencing (genes, present in the panel are listed in Table 4) was performed on a NextSeq 550 (Illumina).

Table 4. Genes covered for all coding exons.

<i>AKT1</i>	<i>BRCA2</i>	<i>EP300</i>	<i>HIST1H3B</i>	<i>MAP2K4</i>	<i>NOTCH3</i>	<i>RAC1</i>	<i>STAG2</i>
<i>AKT2</i>	<i>CBL</i>	<i>EPHA3</i>	<i>HIST1H3C</i>	<i>MAP3K1</i>	<i>NOTCH4</i>	<i>RAD21</i>	<i>STAT3</i>
<i>AKT3</i>	<i>CCND1</i>	<i>ERBB2</i>	<i>HIST2H3C</i>	<i>MAPK1</i>	<i>NPM1</i>	<i>RAD50</i>	<i>STAT5B</i>
<i>ALK</i>	<i>CCND3</i>	<i>ERBB3</i>	<i>HLA-A</i>	<i>MAX</i>	<i>NRAS</i>	<i>RAF1</i>	<i>STK11</i>
<i>AMER1</i>	<i>CD274</i>	<i>ERBB4</i>	<i>HLA-B</i>	<i>MED12</i>	<i>NTRK1</i>	<i>RBI</i>	<i>SYK</i>
<i>APC</i>	<i>CD58</i>	<i>ERG</i>	<i>HLA-C</i>	<i>MEN1</i>	<i>PALB2</i>	<i>RET</i>	<i>TGFBR2</i>
<i>APLNR</i>	<i>CDK12</i>	<i>ESR1</i>	<i>HNF1A</i>	<i>MET</i>	<i>PBRM1</i>	<i>RHOA</i>	<i>TP53</i>
<i>AR</i>	<i>CDK4</i>	<i>ETV6</i>	<i>HRAS</i>	<i>MLH1</i>	<i>PDCD1LG2</i>	<i>RNF43</i>	<i>TSC1</i>
<i>ARAF</i>	<i>CDKN1A</i>	<i>EZH2</i>	<i>IDH1</i>	<i>MSH2</i>	<i>PDGFRA</i>	<i>ROS1</i>	<i>TSC2</i>
<i>ARID1A</i>	<i>CDKN1B</i>	<i>FAS</i>	<i>IDH2</i>	<i>MSH6</i>	<i>PDGFRB</i>	<i>RPL5</i>	<i>U2AF1</i>
<i>ARID1B</i>	<i>CDKN2A</i>	<i>FBXW7</i>	<i>JAK1</i>	<i>MTOR</i>	<i>PHF6</i>	<i>RUNX1</i>	<i>VHL</i>
<i>ARID2</i>	<i>CDKN2B</i>	<i>FGFR1</i>	<i>JAK2</i>	<i>MUTYH</i>	<i>PIK3CA</i>	<i>SETBP1</i>	<i>WT1</i>
<i>ASXL1</i>	<i>CHEK2</i>	<i>FGFR2</i>	<i>JAK3</i>	<i>MYB</i>	<i>PIK3CB</i>	<i>SETD2</i>	
<i>ATM</i>	<i>CIITA</i>	<i>FGFR3</i>	<i>JUN</i>	<i>MYC</i>	<i>PIK3R1</i>	<i>SF3B1</i>	
<i>ATR</i>	<i>CREBBP</i>	<i>FGFR4</i>	<i>KDR</i>	<i>MYCN</i>	<i>PMS2</i>	<i>SMAD4</i>	
<i>ATRX</i>	<i>CTCF</i>	<i>GATA3</i>	<i>KIT</i>	<i>NBN</i>	<i>POLE</i>	<i>SMARCA4</i>	
<i>B2M</i>	<i>CTNNB1</i>	<i>GNAI1</i>	<i>KLF4</i>	<i>NF1</i>	<i>POLQ</i>	<i>SMARCB1</i>	
<i>BAP1</i>	<i>DAXX</i>	<i>GNAQ</i>	<i>KMT2A</i>	<i>NF2</i>	<i>PPP2R1A</i>	<i>SMO</i>	
<i>BLM</i>	<i>DICER1</i>	<i>GNAS</i>	<i>KRAS</i>	<i>NFE2L2</i>	<i>PTCH1</i>	<i>SOCS1</i>	
<i>BRAF</i>	<i>DNMT3A</i>	<i>H3F3A</i>	<i>MAP2K1</i>	<i>NOTCH1</i>	<i>PTEN</i>	<i>SPOP</i>	
<i>BRCA1</i>	<i>EGFR</i>	<i>H3F3B</i>	<i>MAP2K2</i>	<i>NOTCH2</i>	<i>PTPN11</i>	<i>STAG1</i>	

Human Umbilical Vein Endothelial Cells (HUVECs)

HUVECs (Lonza) were cultured in Endothelial Growth Medium (EGM-2) (Lonza) with 1 % Penicillin/Streptomycin (Pen-Strep, Gibco) and 2 % FBS (Gibco). Cells were kept in a humidified incubator at 37°C and 5 % CO₂. Only HUVECs up to passage six were used.

PDOs dissociation into single cells

Organoids were incubated with Dispase I diluted in HSM (Dispase I solution, 2 mg/ml) for 20 minutes at 37°C to digest Matrigel®. Following incubation, organoids were dissociated into single cells by incubation with TrypLE (Gibco) for 10 minutes and Dispase I solution for additional 10 minutes, at 37°C.

PDOs reformation assay

PDOs were dissociated into single cells and resuspended in 50 % Matrigel® and 50 % HSM. They were then plated in a 96-well cell culture plates (1000 cells/well) in five replicas and incubated at 37°C and 5 % CO₂ for 15 minutes before supplementing with tested media. PDOs were incubated at 37°C and 5 % CO₂ for one week and media were changed every three days. One week after plating, cell viability was assessed using CellTiter-Glo® Luminescent cell viability assay (Promega). The results were normalised to +WR of each PDO.

Single-cell RNA-sequencing (scRNA-seq) data mining

For expression of *RSPOs* in PDAC, scRNA-seq dataset from (Peng *et al.*, 2019) (primary PDAC = 24, cells = 41964) was queried. The dataset was first pre-processed using the R package Seurat (Hao *et al.*, 2021) for quality control and filtering (percent_mt_max = 20, nFeature_min = 500, nCount_min = 500, nCount_max = 50000), and then integrated using the harmony function with default parameters. Cell annotation and gene expression stratification by cell type was performed with singleR package and the dataset HPCA from the celldex package (Aran *et al.*, 2019). For the expression of *RSPO3* in normal pancreas, four data sets were queried ((Muraro *et al.*, 2016) cells = 2285; (Segerstolpe *et al.*, 2016), cells = 2394; (Lawlor *et al.*, 2017) cells = 638; (Grün *et al.*, 2016), cells = 1004)). Datasets were downloaded from the Seurat V3 repository together with their annotation metadata.

Human specimens

Formalin-fixed paraffin-embedded (FFPE) tissues were retrieved from the ARC-Net Biobank and were collected under protocol 1885, approved by the local Ethics Committee.

RNA *In Situ* Hybridisation (ISH)

RNA ISH was performed on 4 µm sections of PDAC tissues (n = 8) on adhesion slides. PDAC cases, on which ISH was performed, were the matched patients for

the following PDOs: VR01-O, VR02-O, VR06-O, VR20-O, VR23-O, VR29-O, VR31-O, and VR32-O. Tissues were examined by a pathologist to confirm the presence of neoplastic cells. Excess wax on sections was melted at 60°C for one hour. Sections were then deparaffinised by incubation in xylene for 10 minutes and 100 % ethanol for two minutes. Sections were dried for five minutes at room temperature and incubated for 10 minutes with RNAscope® Hydrogen Peroxide (Advanced Cell Diagnostics) at room temperature. Afterwards, slides were washed with distilled water and antigen retrieval was performed using RNAscope® 1X Retrieval Reagents (Advanced Cell Diagnostics) for 20 mins at 99°C. Sections were then washed again with distilled water, dehydrated in 100 % ethanol for three minutes and dried at room temperature. Slides were then incubated at 40°C for 10 minutes with RNAscope® Protease Plus (Advanced Cell Diagnostics), washed with distilled water and incubated with probes for *RSPO3* (Hs-RSPO3-O3, Advanced Cell Diagnostics), *KRT18* (Hs-KRT18-C2, Advanced Cell Diagnostics), positive control (Hs-UBC; Advanced Cell Diagnostics), and negative control (2-plex negative control probe; Advanced Cell Diagnostics) for two hours at 40°C. Post-hybridisation, slides were washed with RNAscope® 1X Wash Buffer (Advanced Cell Diagnostic). RNAscope® 2.5 HD AMPs (Advanced Cell Diagnostics) were added to the slides following the manufacturer's instructions and slides were washed in RNAscope® 1X Wash Buffer (Advanced Cell Diagnostic) in between each AMP incubation step. Slides were stained with Vina Green™ Chromogen Kit (Biocare) for *RSPO3* and Vector® Red Substrate Kit, Alkaline Phosphatase (AP) (SK-5100, Vector labs) for *KRT18* for 10 minutes at room temperature. Finally, slides were counter-stained with haematoxylin, dried at 60°C for 15 minutes and mounted with VectaMount® mounting medium (Vector Laboratories). Slides were scanned at 40x magnification with the Aperio Scan-Scope XT Slide Scanner within two days of mounting.

Organ-on-a-chip co-culturing

For co-culturing PDOs with HUVECs, OrganoPlate 3-lane (Mimetas) was used. PDOs (VR02-O, VR06-O, and VR32-O) were dissociated into single cells and 2000 cells were seeded in 2 µl of Matrigel® per chip into the middle gel channel and

incubated for 15 minutes at 37°C and 5 % CO₂ before supplementing with media. HUVECs were seeded in EGM-2 medium (10000 cells/chip) in the top perfusion channel and media were also added to the top medium inlet. The plate was then incubated vertically at a 75° angle for two hours at 37°C and 5 % CO₂ to allow for the HUVECs to form a tube. Following incubation, EGM-2 media were added to the top outlet channel. Plates were placed in the incubator on a rocking platform (OrganoFlow, Mimetas) at an incline of 7° and an interval of eight minutes. Media of both PDOs and HUVECs were changed every three days and imaged every day using a brightfield microscope (Molecular devices). At least three chips per condition were used for each PDO.

Live dead staining and quantification

On day seven of co-culturing, PDOs and HUVECs were stained for total nuclei with NucBlue Live ReadyProbes Reagent (Life technologies) and for nuclei of dead cells with DRAQ7TM (BioStatus). Fluorescence imaging was performed using ImageXpress® Micro XLS confocal microscope (Molecular Devices). Quantification was performed in Fiji, using Allevi3D live/dead macro (<https://www.allevi3d.com/livedead-assay-quantification-fiji/>). Percent dead cells was calculated by dividing the number of nuclei of dead cells (DRAQ7TM) over the total number of nuclei (Hoechst). Only middle channels, containing PDOs, were quantified.

Statistical analyses

For all experiments, sample size, statistical tests and replica details are indicated in the figure legends. All statistical analyses were performed with GraphPadPrism Version 9.5.1.

3.3. Results

RSPO: Essential cue for PDOs propagation and reformation

To understand the dependency of PDOs on WNT and RSPO in our cohort, we investigated the effect of their removal on PDOs' propagation and reformation from single cells. First, we performed targeted panel DNA sequencing (genes covered in

Table 4) to confirm that our PDOs (n = 8) were cancer-derived and to understand if any of them harboured mutations in the WNT pathway (e.g.: *CTNNB1*). All models contained activating mutations in *KRAS* and inactivating mutation of *TP53* and had no WNT pathway mutations (Figure S1). To molecularly subtype our models, we performed RNA sequencing. Molecular subtypes were determined based on the classification system from Moffit et al. (2015) and our cohort consisted of four basal-like and four classical PDOs (Table S1).

We first tested the effect of short-term removal of niche factors on PDOs reformation from single cells in four models, including both classical and basal-like ones (VR01-O, VR02-O, VR06-O, and VR29-O). We found that RSPO1 conditioned medium was essential for PDOs reformation from single cells (Figure 1A). Removing WNT3A had no significant effects on reformation, however VR02-O (classical) and VR29-O (basal-like) were affected more than the others, as their viability was reduced by 51.09 % and 52.44 % respectively (Figure 1B). These data suggested that molecular subtype has no influence on WNT dependency in our cohort, different from previous reports (Seino et al., 2018). Finally, removing both WNT3A and RSPO1 conditioned media completely prevented PDOs reformation (Figure 1A). Interestingly, removing only RSPO1, but keeping WNT3A in the media, also showed no PDOs reformation, suggesting that RSPO, rather than WNT drives PDOs' survival in culture.

We then propagated all PDOs (n = 8) in complete media (+WR, Table 1), media without WNT3A conditioned media (-W), without WNT3A and RSPO1 conditioned media (-WR), and HSM media supplemented only with RSPO1 conditioned media. In line with the data from the reformation experiments, we found that RSPO1 conditioned media was also essential for PDOs long-term propagation (Figure 1B). Subtype did not appear to predict niche dependency, as both classical and basal-like PDOs were able to be passaged without WNT3A indefinitely, confirming the observation that molecular subtype has no influence on WNT dependency (Figure 1B). Removing RSPO1, in addition to WNT3A, was detrimental to all cultures, albeit basal-like PDOs were able to survive for slightly longer in those conditions (Figure 1B). RSPO1, alone, was able to support PDOs, as all PDOs were able to be passaged in minimal media, supplemented only with

RSPO1 (Figure 1B). This suggested that PDOs can replace the supplemented WNT, but not RSPO, via internal production. Taken altogether these data suggest that in our cohort RSPO, rather than WNT, is an essential media cue for PDOs, regardless of their molecular subtype.

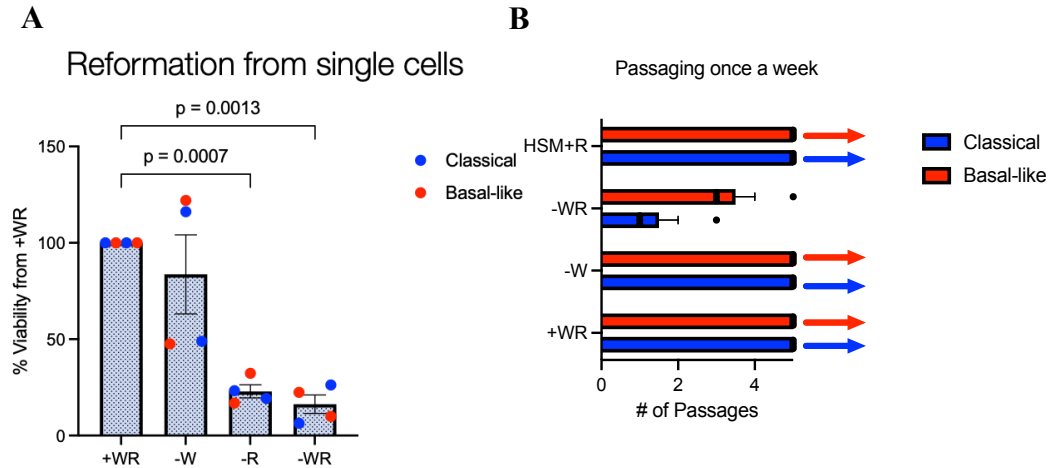


Figure 1. RSPO is an essential media cue for PDOs propagation and reformation. **A.** Scattered dot plot showing the reformation of PDOs ($n = 4$, subtype based on RNA sequencing) as a percentage of the positive control (+WR). PDOs were dissociated into 1000 single cells and plated in 50 % Matrigel® and 50 % HSM in five replicas and then supplemented with tested media. Media were changed every three days and cell viability was assessed using CellTiter-Glo® seven days post-plating. For each PDO the experiment was repeated three times. On the plot, every dot represents an average of all three experiments for each PDO. Error bars represent standard error of the mean (SEM). P values have been determined using standard One-way ANOVA test. **B.** Bar plot showing the number of passages at which PDOs ($n = 8$, subtype based on RNA sequencing), passaged every week with a splitting ratio of 1:3, reach extinction in complete media (+WR), media without WNT3A conditioned media (-W), media without WNT3A and RSPO1 conditioned media (-WR), and HSM media, supplemented only with RSPO1 conditioned media (HSM+R). Arrows indicate that PDOs could be propagated indefinitely.

PDOs are dependent on WNT internal production

To understand whether PDOs were reliant on endogenous WNT, or if they were completely WNT independent, we performed drug treatment experiments using the Porcupine (PORCN) inhibitor C59. C59 inhibits WNT ligand production by blocking the palmitoylation and subsequent WNT secretion (Proffitt *et al.*, 2013). We did long-term (at least three passages) treatment of all PDOs ($n = 8$) with C59 both in complete media and in media without WNT (but supplemented with RSPO).

Unsurprisingly, C59 in the presence of exogenous WNT supplementation had little to no effect on all PDOs. However, removing WNT and blocking endogenous WNT ligands, was detrimental to the cultures within three passages (Figure 2A). Interestingly, exogenous RSPO alone was not sufficient to protect PDOs from the detrimental effect of C59, thereby suggesting that RSPO is indeed acting through hyperactivation of the WNT pathway. To confirm this, we also treated PDOs, grown in minimal media and RSPO (HSM+R), with C59 and as expected, C59 without exogenous WNT supplementation was detrimental to the culture (Figure 2B). Accordingly, supplementing with WNT3A conditioned media was able to rescue PDOs.

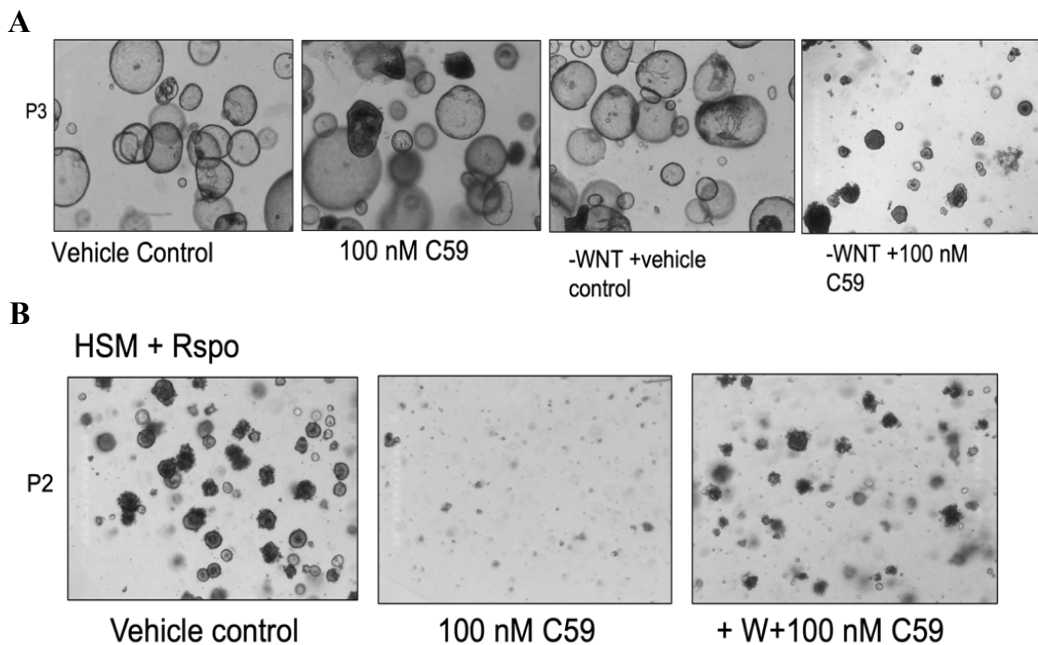


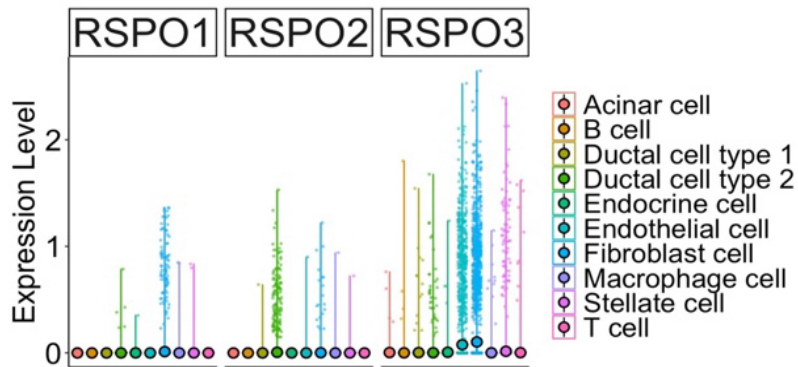
Figure 2. PDOs are dependent on internal WNT ligand production. A. Representative images of PDO once a week for up to three passages (P3) in +WR and vehicle control, +WR and 100 nM C59, -W and vehicle control and -W and 100 nM C59. The experiment was repeated for eight PDOs. Representative images display VR06-O. **B.** Representative images of PDO once a week for up to two passages (P2) in HSM+R and vehicle control, HSM+R and 100 nM C59, and HSM+R+W and 100 nM C59. Representative images display VR01-O.

RSPOs source in PDAC: CAFs and endothelial cells

The role of the PDOs' media is to mimic the microenvironment by providing supportive cues to cancer cells (Hofer and Lutolf, 2021). Therefore, it is important to identify the source of stromal cues *in vivo*. To understand the source cells of RSPO, we queried PDAC scRNA-seq dataset (Peng *et al.*, 2019) for *RSPO1* expression, however we found very low expression, predominantly restricted to CAFs (Fibroblast cell) (Figure 3A). As the R-spondin protein family consists of four proteins (RSPO1-4), which can have interchangeable functions, we also investigated the expression of those (de Lau *et al.*, 2012). We found no evidence for *RSPO4* expression and expression levels of *RSPO2* were similar to those of *RSPO1*. Interestingly, neoplastic cells ("Ductal cell type 2"), rather than stromal ones, appeared to be the predominant source of *RSPO2*. Finally, *RSPO3* was the most highly expressed R-spondin, mainly expressed by endothelial cells and CAFs (Figure 3A). Moreover, *RSPO3* expression seemed to be limited to PDAC, as we found very low expression in normal pancreas scRNA-seq datasets (Figure S2). In normal pancreases *RSPO3* expression seemed mainly restricted to activated stellate cells, the precursors of fibroblasts (Figure S2). In summary, scRNA-seq data strongly suggested that RSPO3 is the predominant RSPO *in vivo* and it is provided by stromal cells, namely CAFs and endothelial cells. To orthogonally validate this inference, we performed RNA *in situ* hybridisation (ISH) for *RSPO3* and a marker of cancer epithelial cells, *KRT18* (cytokeratin 18) on patient FFPE tissues (n = 8). We found *RSPO3* expression with varying levels in seven cases, reflecting inter-patient stromal heterogeneity. One case, VR29-O was completely negative for *RSPO3* (Figure 3A). In four cases (VR01-O, VR06-O, VR23-O, and VR32-O), we found high levels of *RSPO3* expression, with the signal localising predominantly to CAFs (Figure 3B). However, in three cases (VR02-O, VR20-O, and VR31-O) there were very low levels of *RSPO3* in CAFs. Interestingly, we also found *RSPO3* localising to blood vessels in five cases (Figure 3B), suggesting that the scRNA-seq inference was correct as endothelial cells form the linings of blood vessels. As stromal cell populations could differ based on their location with respect to the neoplastic cells, we also examined if there was any correlation between *RSPO3* levels and distance to tumours, however, we found no pattern. ISH analysis on

patient tissues confirmed scRNA-seq that RSPO3 is provided by endothelial cells and CAFs. However, as PDOs media is supplemented with RSPO1, and not RSPO3, we also investigated if RSPO3 can replace RSPO1 in PDOs culturing. To this aim, we propagated PDO VR23-O in depleted media (-WR), supplemented with recombinant RPO3 (Figure 3C). RSPO3 rescued VR23-O in the absence of WNT3A and RSPO1, suggesting RSPO3 and RSPO1 are interchangeable in PDOs media. Taken altogether, these results suggest that RSPO3 is a major cue in the PDAC stroma, that supports cancer cells, and it is provided by CAFs and endothelial cells.

A



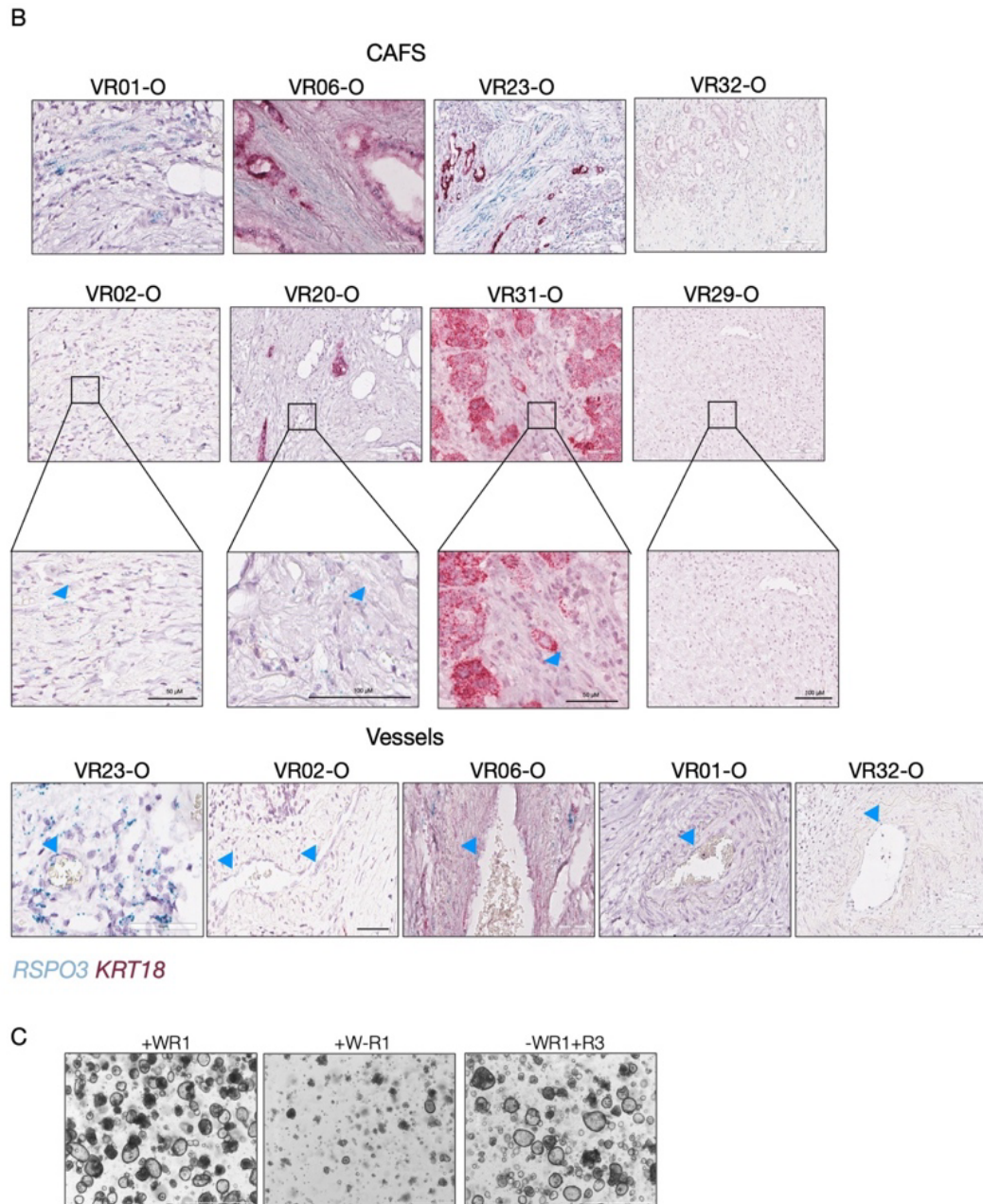


Figure 3. RSPO3 is the dominant RSPO in humans and it can replace RSPO1 in PDOs. A. Violin plots showing the number of cells of each cell type that expresses *RSPO1*, *RSPO2* and *RSPO3*, based on scRNA-Seq data obtained from Peng et al., 2019. “Ductal cell type 2” represent neoplastic cells. No expression was found for *RSPO4*. The total number of cells queried is shown at the top. **B.** Representative RNA ISH images for *RSPO3* (blue) and *KRT18* (red, epithelial cells) for each case, indicating cases where *RSPO3* was detected in CAFs (n = 7) and vessels (n = 5). Blue arrows point to *RSPO3* signal. VR29-O was completely negative for *RSPO3*. **C.** Representative

images showing PDO propagated once a week in a 1:3 ratio in complete media (WR1), media with WNT3A but without RSPO1 conditioned media (+W-R), and in -WR. media, supplemented with recombinant RSPO3 (100 ng/ml). Scale bars represent 1000 μ m.

Endothelial cells can support PDOs survival in the absence of RSPO

As CAFs' role in cancer cells survival by providing niche factors have been previously demonstrated, we next focused our functional experiments on endothelial cells (Seino et al., 2018). To understand if endothelial cells can rescue PDOs in the absence of RSPO, we performed co-culturing experiments with PDOs and HUVECs, using organ-on-a chip system. We used the OrganoPlate 3-lane system by Mimetas, which consists of three different channels, where different cell types can be cultured for a limited period (Figure 4A). The gaps between channels allow for cell-to-cell communication via ligands' release. We used both basal-like and classical PDOs (VR02-O, VR06-O, and VR32-O), as well as HUVECs, a primary cell culture, regularly used to study endothelial cells *in vitro* (Cao et al., 2017). As the OrganoPlate does not allow for continuous propagation, we focused on investigating if HUVECs can rescue PDOs reformation from single cells instead. We plated single cells from organoids in ECM, in complete media and -WR and in the absence or presence of HUVECs. HUVECs were seeded in the top inlet channel in their own media to ensure their proliferation and survival. Post-seeding, the plate was incubated at a vertical angle to allow the HUVECs to form a tube. After one week of culturing, we performed a live-dead assay by staining nuclei of dead cells and nuclei of all cells. For all tested models, HUVECs appeared to rescue organoid reformation in the absence of WNT and RSPO (Figure 4B). Moreover, when we quantified the number of dead cells in the middle channel (where PDOs were seeded), we found that HUVECs significantly reduced the number of dead cells in the absence of WNT and RSPO (Figure 4C). By using this co-culturing system, we were able to show that endothelial cells can rescue PDOs in the absence of niche factors, likely due to RSPO secretion.

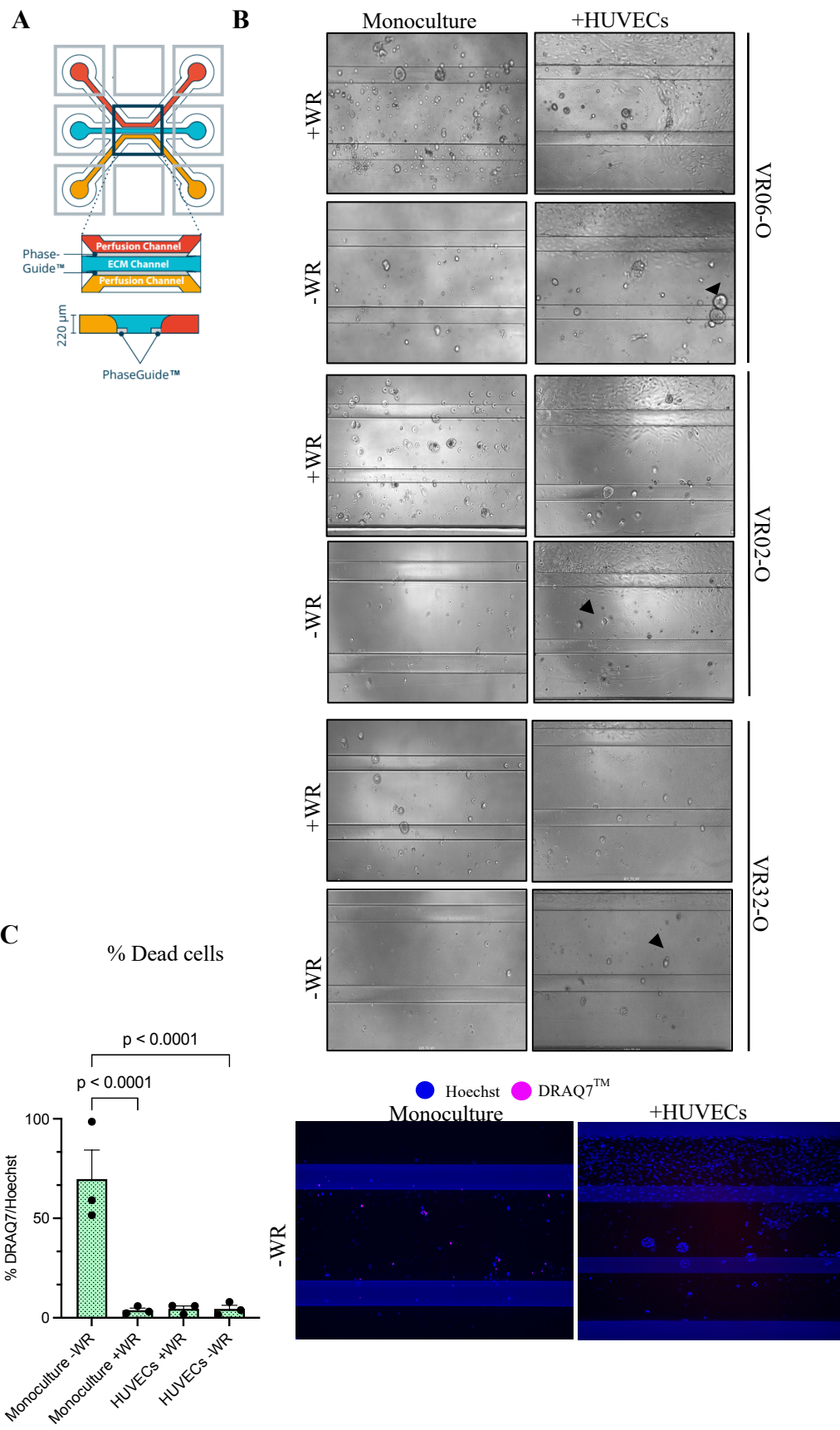


Figure 4. Endothelial cells can rescue PDOs reformation in the absence of RSPO/WNT. **A.** A schematic representation of the OrganoPlate 3-lane used in co-culturing experiments. Figure taken from <http://mimetas.com>. **B.** Representative images on day 7 post-plating for each tested PDO (n = 3) in monoculture or co-cultured with HUVECs, in complete media (+WR) or media without WNT3A and RSPO1 (-WR). Black arrows indicate organoids in PDOs co-cultured with HUVECs in-WR **C.** Scattered dot plot showing % Dead cells for each PDO, calculated as the number of DRAQ7™ positive nuclei over total number of nuclei (Hoechst positive nuclei). For each PDO (each dot), the experiment was performed in at least three replicas. On the plot, each dot represents an average of all replicas for each PDO. Error bars represent standard error of the mean (SEM). P values have been determined using standard One-way ANOVA test. On the right, representative images showing Hoechst (blue) and DRAQ7™ (red) staining for a PDO in -WR, in monoculture and co-cultured with HUVECs.

3.4. Discussion

In this preliminary study we determined that RSPO, rather than WNT is an essential stromal cue that supports cancer cells *in vitro*. This RSPO dependency was valid for all tested PDOs, regardless of molecular subtype. Additionally, PDOs appeared to be relying on internally produced WNT and needed RSPO to potentiate signalling. We then established a previously unknown endothelial niche, where endothelial cells can provide and support cancer cells with RSPO. Finally, by performing ISH on patient tissues we were able to validate our findings that RSPO is found in endothelial cells and CAFs *in vivo*.

Whereas previous studies have found PDOs consistently dependant on WNT and RSPO, our PDOs were all dependant only on RSPO (Boj et al., 2015). Additionally, we did not have any PDOs that were WNT dependant, as all of them could be propagated without WNT (Seino et al., 2018). Finally, we did not observe any progression from classical to basal-like subtype paralleling the RSPO dependency: lack of RSPO was detrimental to all cultures, regardless of subtype. Interestingly, basal-like PDOs could survive lack of WNT and RSPO for slightly longer than classical ones, but the subtype did not affect reformation of PDOs from single cells. These differences could be explained through the intrinsic differences in the PDOs cohorts. Another explanation could be found in the fact that the PDOs' media, rich in WNT and RSPO, has been shown to “push” PDOs towards a classical subtype (Raghavan et al., 2021). Thus, despite being subtyped as basal-like or classical

initially, it is possible that the culture conditions have selected for a classical phenotype over time.

RSPOs work with WNT to potentiate WNT signalling and downstream pathways (de Lau *et al.*, 2012). One of the pathways they activate is the WNT/ β -catenin signalling pathway (canonical), whose overactivation is linked to cancer development and progression (ter Steege and Bakker, 2021). In PDAC, this pathway is particularly important for tumorigenesis, as WNT inhibition blocks ADM, PanINs, and PDAC development in mouse models (Zhang *et al.*, 2013). However, the pathway is rarely dysregulated in PDAC due to activating mutations, but largely due to hyperactive signalling at the plasma membrane level (White, Chien and Dawson, 2012; Makena *et al.*, 2019; Zhong *et al.*, 2020). Yet, WNTs and RSPOs are known to activate other less studied pathways (non-canonical), such as the WNT/ Ca^{2+} pathway, which can also promote survival and proliferation (Kühl *et al.*, 2000). Thus, it is unsurprising that PDOs are highly dependent on WNT signalling. However, our experiments suggest that WNT acts in an autocrine manner, and it is produced by cancer cells themselves, in line with the self-sufficiency hallmark of cancer (Hanahan and Weinberg, 2000). Further experimental evidence is needed, however, to understand whether RSPO is activating the canonical WNT signalling, or it is cooperating with WNTs to activate non-canonical pathways.

Whereas WNT signalling appeared to be autocrine, cancer cells seemed to be relying on the microenvironment to produce RSPO, as removing external supplementation was detrimental. We identified both endothelial cells and CAFs as source TME cells of RSPO, via RNA ISH and scRNA seq. CAFs produce WNTs, and they have already been shown to support PDOs in the absence of niche factors (Seino *et al.*, 2018). Additionally, endothelial cells can *trans*-differentiate into CAFs via process known as endothelial-mesenchymal transition (EndMT) (Zeisberg *et al.*, 2007; Garcia *et al.*, 2012). In tumours, CAFs are much more likely to be a product of *trans*-differentiation of local cells than due to recruitment of precursors (Arina *et al.*, 2016). Thus, endothelial cells and CAFs are intimately linked and their role in the tumour-stroma crosstalk is not limited to vessels formation. Thus, we mechanistically explored the role of the endothelial cells and found that they could

providing cancer cells with cytokines. This is in line with previous studies, showing *RSPO3* is expressed by the vasculature, and it is crucial for vascular development, which it stimulates via the non-canonical WNT/Ca²⁺ pathway (Cambier *et al.*, 2014; Scholz *et al.*, 2016). Moreover, a recent study showed that endothelial cells support and maintain cancer-initiating cells via WNT signalling (Choi *et al.*, 2021). Our study lends evidence to the hypothesis that endothelial cells produce RSPO3, which in turn supports cancer cells. Moreover, endothelial cells (and fibroblasts) produced RSPO3 has been found to maintain the intestinal stem cell niche in normal tissues (Goto *et al.*, 2022). Therefore, it is likely that endothelial cells in cancer could support a cancer stem cell niche. However, further studies are required to identify whether endothelial cells are instructed by the cancer cells to produce RSPO3 or if RSPO3 is co-opted from nearby endothelial cells. In our study, endothelial cells did not completely rescue PDO reformation, with only few organoids reforming, which might be due to the usage of non-cancer derived endothelial cells. Better *in vitro* models are needed to investigate the endothelial stem cells, which cannot just rely on HUVECs, which are cancer-naïve and are completely different to the collapsed endothelium, found in PDAC.

In conclusion, our study provides preliminary data that RSPO3 supports cancer cells and that the endothelial niche in PDAC needs to be investigated better, not just in terms of vascularisation, but also in terms of cytokines that promote tumorigenesis.

3.5. Supplementary data

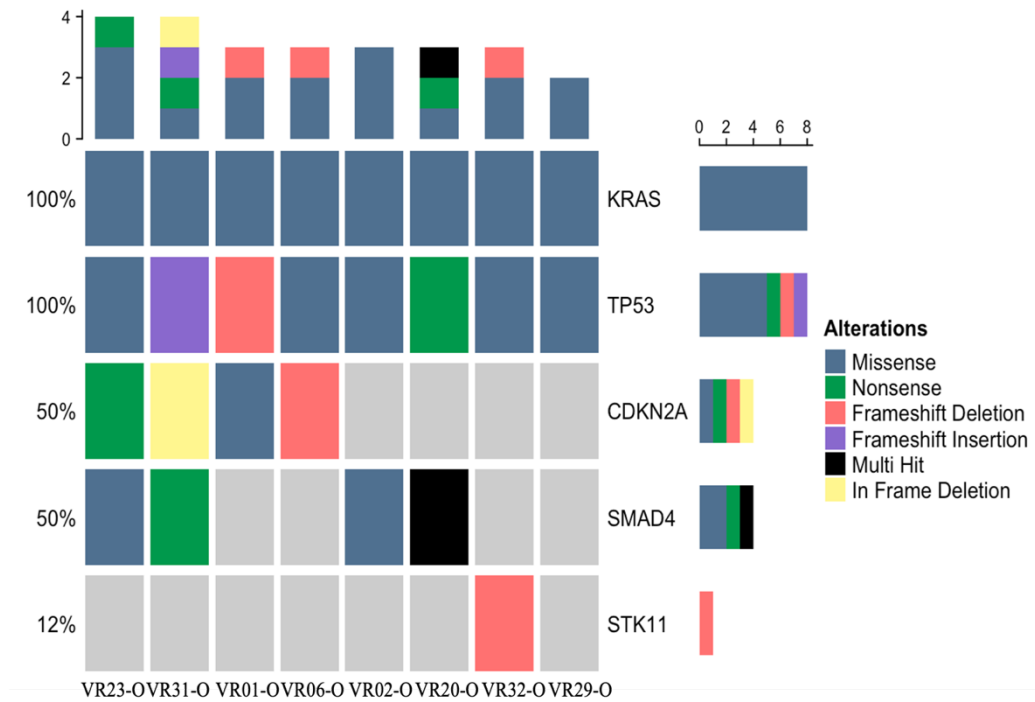


Figure S1. Overview of genetic drivers in PDOs. Oncoplot showing mutations in oncogenes for all PDOs.

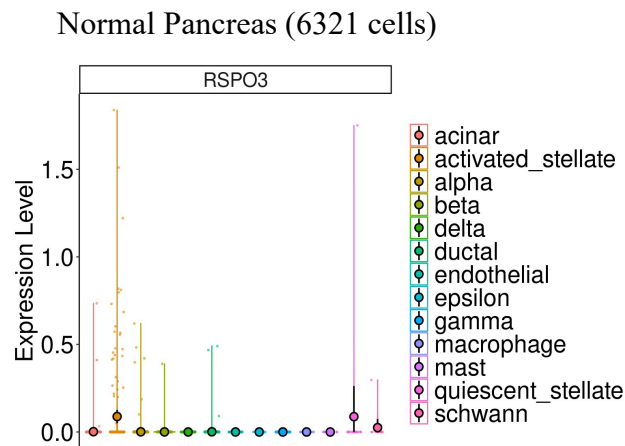


Figure S2. Normal pancreas has low expression levels of *RSPO3*. Violin plot showing the number of cells of each cell type that express *RSPO3*, based on scRNA-Seq data obtained from Muraro et al., 2016; Segerstolpe et al., 2016; Lawlor et al., 2017; Grün et al., 2016. The total number of cells queried is shown at the top.

Table S1: Molecular subtypes (based on Moffit et al., 2015) of PDOs, as determined by RNA sequencing.

ID	Subtype
VR01-O	Classical
VR02-O	Classical
VR06-O	Basal-like
VR20-O	Classical
VR23-O	Classical
VR29-O	Basal-like
VR31-O	Basal-like
VR32-O	Basal-like

4. ecDNA amplification of *MYC* drives intratumoral copy-number heterogeneity and adaptation to stress in PDAC

Antonia Malinova^{1*}, Daniel Schreyer^{2*}, Elena Fiorini^{1*}, Davide Pasini¹, Sabrina D'Agosto³, Silvia Andreani³, Francesca Lupo¹, Lisa Veghini¹, Sonia Grimaldi³, Craig Nourse^{4,5}, Roberto Salvia⁶, Giuseppe Malleo⁶, Andrea Ruzzenente⁷, Alfredo Guglielmi⁷, Michele Milella⁸, Rita Lawlor^{1,3}, Claudio Luchini⁹, Christian Pilarsky¹⁰, Aldo Scarpa^{3,9}, David A. Tuveson¹¹, Peter Bailey^{2,5^§} & Vincenzo Corbo^{1,3^§}

¹Department of Engineering for Innovation Medicine, University of Verona, Verona, Italy

²Wolfson Wohl Cancer Research Centre, Institute of Cancer Sciences, University of Glasgow, Glasgow, UK

³ARC-Net Research Centre, University of Verona, Verona, Italy

⁴Cancer Research UK Beatson Institute, Glasgow, Scotland, UK

⁵Botton-Champalimaud Pancreatic Cancer Centre, Lisbon Portugal

⁶Department of General and Pancreatic Surgery, The Pancreas Institute, University of Verona, Verona, Italy

⁷Division of General and Hepatobiliary Surgery, Department of Surgical Sciences, University of Verona, Verona, Italy

⁸Section of Medical Oncology, Department of Medicine, University of Verona, Verona, Italy

⁹Department of Diagnostics and Public Health, University of Verona, Verona, Italy

¹⁰Department of Surgery, Universitätsklinikum Erlangen, Erlangen, Germany.

¹¹Cold Spring Harbor Laboratory, Cold Spring Harbor, NY, USA

* co-first authors

^ co-last authors

§ corresponding authors

4.1. Introduction

Oncogene dosage variation is a major determinant of tumour progression and phenotypic heterogeneity (Bielski *et al.*, 2018; Mueller *et al.*, 2018; Marusyk, Janiszewska and Polyak, 2020). Focal oncogene amplifications and rearrangements have been demonstrated to underpin oncogene dosage variation and can exist as linear amplifications of contiguous genomic segments or as circular extrachromosomal DNAs (ecDNAs). ecDNAs lack centromeres and consequently segregate unevenly between daughter cells during mitosis (Levan *et al.*, 1976; Yi *et al.*, 2022). This non-Mendelian pattern of inheritance enables individual cells to accumulate large numbers of ecDNA-bearing oncogenes in response to specific microenvironmental changes (Lange *et al.*, 2022). Rapid depletion of ecDNAs is also observed when cancer cells are no longer exposed to the selective pressure, for which they confer enhanced fitness (Haber and Schimke, 1981; Schulte *et al.*, 2012; Nathanson *et al.*, 2014; Lange *et al.*, 2022).

Oncogenic amplifications of genes including *GATA6*, *KRAS* and *MYC* have been shown to shape PDAC cancer phenotypes (Notta *et al.*, 2016; Peter Bailey *et al.*, 2016; Martinelli *et al.*, 2017; Mueller *et al.*, 2018; Chan-Seng-Yue *et al.*, 2020; Miyabayashi *et al.*, 2020). Elevated *MYC* activity promotes biologically aggressive PDAC phenotypes by driving proliferation and remodelling of the tumour microenvironment (Hayashi *et al.*, 2020; Maddipati *et al.*, 2022). *MYC* amplifications are specifically enriched in PDAC liver metastases and are associated with basal-like and squamous subtypes (Hayashi *et al.*, 2020). Therefore, identifying the genetic events driving transcriptional *MYC* heterogeneity is critical to advance our understanding of disease progression and metastasis. To overcome the limitation of poor neoplastic cellularity of PDAC tissues and enable modelling the dynamics of endogenous oncogene amplifications, we comprehensively characterised a large array of patients derived organoids (PDOs). The integration of PDOs genomes, transcriptomes, and *in situ* analyses with functional studies revealed the role of ecDNA-based *MYC* amplification in driving extensive copy-number heterogeneity and the adaptation of PDAC cells to the depletion of stromal niche factors.

4.2. Materials and methods

Human specimens and clinical data

PDAC tissues were obtained from the General and Pancreatic Surgery Unit at the University of Verona. Written informed consent was obtained from patients preceding the acquisition of the specimens. The fresh tissues used to establish PDOs were collected under a study approved by the Integrated University Hospital Trust (AOUI) Ethics Committee (Comitato Etico Azienda Ospedaliera Universitaria Integrata): approval number 1911 (Prot. n 61413, Prog 1911 on 19/09/2018). Formalin-fixed and paraffin-embedded tissues were collected under protocol number 1885 approved by the AOUI Ethics Committee and retrieved from the ARC-NET Biobank.

Patient-derived organoid (PDOs) establishment and culture

PDAC PDOs were established following previously published procedures (Boj et al., 2015). The specimens used to generate PDOs were examined by pathologists to confirm the presence of neoplastic cells. Briefly, tissue specimens were minced and digested with Collagenase II (5 mg/ml, Gibco) and Dispase I (1.25 mg/ml, Gibco) in human splitting medium (HSM) [Advanced Dulbecco's Modified Eagles Medium with Nutrient Mixture F-12 Hams (Gibco) supplemented with HEPES (10 mM, Gibco), Glutamax™ (2 mM, Gibco), and Primocin® (1 mg/ml, InvivoGen)] at 37°C for a maximum of two hours, followed by an additional 15-minute digestion with TrypLE (Gibco) at 37°C. The digested material was embedded in Growth factor reduced Matrigel® (Corning) and overlaid with human complete medium (+WR) [Mouse Epidermal Growth Factor (Gibco, 50 ng/ml), B-27 Supplement (Gibco, 1X), Nicotinamide (Sigma-Aldrich, 10 mM), N-Acetylcysteine (Sigma-Aldrich, 1.25 mM), FGF10 (Peprotech, 100 ng/ml), Y-27632 Dihydrochloride (Sigma, 10.5 µM), Gastrin (Tocris, 10 nM), TGFβ Receptor inhibitor A83-01 (Tocris, 500 nM), WNT3A Conditioned media (50 % v/v), RSPO1 Conditioned media (10 % v/v), and mNoggin (Peprotech, 100 ng/ml)]. Media were refreshed every 3-4 days. For organoid propagation, confluent organoids were removed from Matrigel®, dissociated into small clusters of cells by pipetting, and resuspended in an appropriate volume of fresh Matrigel®. All organoid models

were acquired as part of the Human Cancer Model Initiative (HCMI, <https://ocg.cancer.gov/programs/HCMI>) and are available for access from ATCC. The corresponding IDs, along with the clinical data are listed in Table S1. Dependency of organoid cultures to WNT3A and RSPO1 was assessed on nine PDOs (VR01, VR02, VR06, VR09, VR20, VR21, VR23, VR29, and VR32). Organoid cultures were passaged once a week with a splitting ratio of 1:3 in +WR or Human Depleted Media (-WR) [Mouse Epidermal Growth Factor (Gibco, 50 ng/ml), B-27 Supplement (Gibco, 1X), Nicotinamide (Sigma-Aldrich, 10 mM), N-Acetylcysteine (Sigma-Aldrich, 1.25 mM), FGF10 (Peprotech, 100 ng/ml), Y-27632 Dihydrochloride (Sigma-Aldrich, 10.5 μ M), and Gastrin (Tocris, 10 nM)]. To establish WR independent PDOs, organoids established and propagated in +WR were placed and maintained in -WR for several passages. Due to the cell death induced by -WR, the media were refreshed every three days and Matrigel® every 14 days without propagating the cultures, until the emergence of WR independent PDOs. Growth curve of WR independent PDOs was obtained by plotting the number of domes (one dome refers to 50 μ l of Matrigel®) at different days of culture in -WR. Adapted PDOs were reintroduced in +WR or maintained in -WR (control) for five passages before collection of metaphase spreads and proteins. To obtain “Late passage” PDOs, organoids were passaged 40 times post-establishment in +WR medium. For Wnt-C59 experiment, baseline and adapted organoids were passaged every seven days with a splitting ratio of 1:3 in the presence of Wnt-C59 (100 nM, Selleckchem). Wnt-C59 was added to the culture at the day of splitting and after three days of culture. Organoids were routinely tested for the presence of *Mycoplasma* contamination using Mycoalert Mycoplasma Detection kit (Lonza).

Single cells dissociation from organoids

Organoids were incubated with Dispase I diluted in HSM (Dispase I solution, 2 mg/ml) for 20 minutes at 37°C to digest Matrigel®. Following this, organoids were dissociated using TrypLE (Gibco) for 10 minutes at 37°C, incubated in Dispase I solution for additional 10 minutes at 37°C, and pipetted to obtain single cells suspension.

Assessing *MYC* activation by WR media

VR01-O was dissociated into single cells as previously described and plated in Matrigel® in +WR (100,000 viable cells/condition). Following organoids' reformation in +WR, PDOs were starved overnight in HSM. Post-starvation, PDOs were stimulated with +WR, -WR, or HSM for eight hours, before collection and isolation of RNA.

JQ1 *in vitro* treatment

Organoids were dissociated into single cells as previously described. One thousand viable cells were plated in 100 µl 10% Matrigel®/media per well in a 96-well plate in triplicates. JQ1 (500 nM, Selleckchem, S7110) or vehicle were added 40 hours after plating once the organoids were reformed. After 72 hours of treatment, cell viability was assessed using CellTiter-Glo® (Promega) following manufacturer's instructions. Results were normalised to the vehicle control of each PDO. In parallel, 20,000 viable cells/50 µl Matrigel®, were plated and supplemented with media. Following organoids reformation, cells were treated with JQ1 (500 nM) or vehicle control, and RNA, protein, and metaphase spreads were collected after 72 hours.

Lentiviral production and infection of organoids

To overexpress *MYC*, we used a lentiviral vector carrying an open-reading frame for *MYC* (mGFP tagged, Origene, cat# RC201611L4). Lentivirus was produced by transfecting the plasmid containing *MYC*, and the packaging plasmid VSV-G with X-tremeGENE9 (Roche, 063665110101) in HEK293T cells. The viral supernatant was harvested 48 hours post-transfection and quantified using Lenti-XTM qRT-PCR Titration kit (Takara Bio) according to manufacturer's instructions. pLenti-C-Myc-DDK-P2A-Puro lentiORF control particles (Origene, PS100092V) were used as non-targeting control (NTC). For infection, organoids were dissociated into single cells, resuspended in infection media (Dulbecco's Modified Eagle Medium (DMEM, Gibco), 5 % Foetal Bovine Serum (FBS, Gibco), 1 % Penicillin/Streptomycin (P/S, Gibco)), supplemented with 1 µg/mL polybrene and lentiviral particles (MOI 10). Cells were then spinoculated for one hour at room

temperature (RT) and incubated at 37°C for 16 hours. Infected cells were then collected, embedded in Matrigel®, and overlaid with +WR media. Antibiotic selection was started 48 hours after infection using 2 µg/ml puromycin (Gibco).

Organoids' metaphase spreads and interphase nuclei

Organoids were incubated with Colcemid (1 µg/ml, Gibco) in culture media at 37°C and 5 % CO₂ overnight. Following incubation, organoids were dissociated into single cells as previously described. Single cells were incubated in hypotonic solution (potassium chloride 0.56 % and sodium citrate 0.8 %) for 20 minutes at RT. Nuclei were then fixed in ice cold methanol- acetic acid (3:1), washed with methanol-acetic acid (2:1), and dropped on adhesion microscope slides.

DNA Fluorescence *in situ* hybridisation (FISH)

DNA FISH on methanol-acetic acid fixed nuclei was performed using the ZytoLight SPEC MYC/CEN8 Dual Color FISH probe (ZytoVision) while FISH on nuclei from formalin-fixed paraffin-embedded tissues and organoids was performed using a Vysis LSI MYC Break Apart Rearrangement Probe kit (Abbott). Before hybridisation, tissues were deparaffinised and rehydrated, pre-treated with 0.1 citrate buffer (pH 6) solution at 85°C for 30 minutes, followed by pepsin treatment (4 mg/ml in 0.9% NaCl, pH 1.5) for four minutes at 37°C. For both tissues and PDOs, the probes were applied to the slides and sealed with rubber cement and incubated in a humidified atmosphere (Thermobrite System) at 80°C for 10 minutes to allow denaturation of the probes and of the DNA target. Slides were then incubated overnight at 37°C to allow for hybridisation. The rubber cement and the coverslip were then removed, and the slides were washed in 2X SSC/0,3% NP40 for 15 minutes at RT and then at 72°C for two minutes. Following post-hybridisation washes, slides were counterstained with DAPI 1 µg/ml (Kreatech, Leica).

For tissues and embedded organoids, images were acquired on Leica DM4B Fluorescent microscope. *MYC*-targeting probe was acquired in red (Rhodamine) and pseudo-coloured as green to match *MYC* signal from PDOs. Nuclei were acquired and visualised in blue (DAPI).

For PDOs, images were acquired either on Leica DM4B, ZEISS Axio Imager 2 or Leica TCS SP5 Fluorescent microscopes. The *MYC*-targeting probe was acquired and shown in green (L5 for Leica, GFP for ZEISS). For the Leica microscopes, the *CEN8*-targeting probe was acquired and shown in red (Rhodamine). For ZEISS, the *CEN8*-targeting probe was acquired in Orange (DsRed) and pseudo-coloured as red to match the *CEN8* signal from Leica. Nuclei were acquired and visualised in blue (DAPI). Number of fluorescent signals for each probe for each nucleus, for both tissues and PDOs, was quantified with FIJI (ImageJ2 version 2.9.0/1.53t). Number of ecDNA+ metaphases were counted by visual inspection of slides. To quantify hubs of overlapping signal, a scoring system (0-3) was devised, where each score corresponded to a level of overlapping signal. Representative images for each score are shown in Figure S7.

Histology and immunostaining

For histopathological analysis, organoids were released from Matrigel® using Dispase I solution as previously described, fixed with 10% neutral buffered formalin for 20 minutes, and embedded in Histogel Processing Gel (FisherScientific). Histogel-embedded organoids were processed according to routine histology procedures and embedded in paraffin. To account for effect of the media, +WR PDOs were put in -WR for 24 hours prior to embedding and fixation. Haematoxylin and Eosin (H&E) and immunostainings were performed on sections of formalin-fixed, paraffin-embedded tissues and organoids, following established procedures using the reported primary antibodies: c-Myc (Abcam, cat# ab32072), GATA6 (R&D Systems, cat#AF1700), Δ Np63 (Leica, clone BC28, cat#PA0163), CK5 (Novocastra, clone XM26, cat# PA0468), Ki67 (Abcam, cat#ab16667), and γ -H2AX (eBioscience, clone CR55T33, cat#14-9865-82). Immunohistochemistry slides were then scanned and digitalised using the Aperio Scan-Scope XT Slide Scanner (Aperio Technologies). In tissues, c-Myc staining was quantified as a percentage of positive nuclei per neoplastic duct using Aperio ImageScope. In organoids, c-Myc, Ki67, and GATA6 staining were quantified as percentage of positive nuclei per organoid, using Aperio ImageScope. For immunofluorescence,

images were acquired by Leica TCS SP5 Fluorescent microscope and quantify using ImageJ (<https://imagej.nih.gov/>).

Immunoblotting

Proteins were prepared using Cell Lysis Buffer (Cell Signaling Technology) supplemented with Protease inhibitor cocktail (Sigma) and Phosphatase inhibitor PhosphoSTOP (Roche). Protein lysates were separated on 4-12 % Bis-Tris NuPAGE gels (Life technologies), transferred to a PDVF membrane (Millipore) and then incubated with the reported antibodies: c-Myc (Abcam, cat# ab32072), γ -H2AX (Abcam, cat# ab81299), GAPDH (Cell Signaling Technologies, cat# 5174), and vinculin (Cell Signaling Technologies, cat# 4650). To account for effect of the media, +WR PDOs were put in -WR for 24 hours prior to collection of the cells' pellet.

DNA Isolation

Organoids were incubated in Cell Recovery Solution (Corning) for 30 minutes at 4°C to remove Matrigel®, and were pelleted by centrifuging 10,000 g for 5 minutes at 4°C. For tissues, slices from snap frozen PDAC tissues were assessed by a pathologist for percent neoplastic cellularity and only tissues with higher than 20 % neoplastic cellularity were used. For WGS and panel DNA sequencing, DNA isolation was performed using DNeasy Blood & Tissue kit (Qiagen). For CIRCLE-Seq, high molecular weight DNA was extracted using the MagAttract HMW DNA Kit (Qiagen).

Whole genome sequencing (WGS)

DNA quality was assessed by DNF-467 Genomic DNA 50 kb Kit on a Bioanalyzer 2100 (Agilent). Libraries were prepared and sequenced using NovaSeq 6000 S4 Reagent Kit v1.5 (300 cycles) at 15x coverage 160 million reads/sample.

Data pre-processing and alignment

Sequencing data were pre-processed and mapped to the reference genome using the nf-core/sarek pipeline (version 3.0.2) (Garcia *et al.*, 2020). In short, Fastp (version 0.23.2) (Chen *et al.*, 2018) removed low-quality bases and adapters, BWA Mem

(version 0.7.17-r1188) (Li, 2013) mapped trimmed reads to the reference genome GRCh38, provided by the Genome Reference Consortium (<https://www.ncbi.nlm.nih.gov/grc>), mapped reads were marked for duplicates using Picard MarkDuplicates, and read base quality scores were recalibrated using GATK BaseRecalibrator and GATK ApplyBQSR (McKenna *et al.*, 2010).

Amplicon Characterisation

The nf-core/circdna (version 1.0.1, <https://github.com/nf-core/circdna>) pipeline branch 'AmpliconArchitect' was used to define amplicon classes in each WGS sample. Nf-core/circdna calls copy number using cnvkit (version 0.9.9) (Talevich *et al.*, 2016) and prepares amplified segments with a copy number greater than 4.5 for AmpliconArchitect by utilising functionality of the AmpliconSuite-Pipeline (<https://github.com/jluebeck/AmpliconSuite-pipeline>) AmpliconArchitect (version 1.3_r1) (Deshpande *et al.*, 2019) was ran on the aligned reads and the amplified seeds to delineate the amplicon structures. Identified amplicons were then classified using AmpliconClassifier (version v.0.4.11) (Luebeck *et al.*, 2023) into circular (ecDNA), linear (linear amplicon), complex (complex amplicon), or BFB (amplicon with a breakage-fusion-bridge signature). Samples containing at least one circular amplicon (ecDNA) were termed "ecDNA+", whereas samples without ecDNA amplicons were termed "ecDNA-". Samples were also classified into 'Circular', 'Linear', 'Complex', 'BFB', or 'no-fSCNA' (no-focal somatic copy number amplification detected) by the types of amplicons they contained (see Kim *et al.* (Kim *et al.*, 2020). Samples with multiple amplicons were classified based on the amplicon with the highest priority. The priority is: Circular > BFB > Complex > Linear.

Copy number calling

Copy number calls of the WGS samples were generated by cnvkit (version 0.9.9) (Talevich *et al.*, 2016). The identified segments were then classified as gain (copy number ≥ 3), loss (copy number ≤ 1), or deep loss (copy number ≤ 0.25).

Chromosomal instability signatures

Chromosomal instability signatures, including the CX9 replication stress signature, were assessed from the WGS copy number profiles using the R-package CINSignatureQuantification (Drews *et al.*, 2022).

Ploidy analysis

Sample ploidy was derived using PURPLE (Priestley *et al.*, 2019), which estimates copy number and ploidy by using read depth ratio and tumour- B-allele frequency (BAF) from COBALT and AMBER, respectively (<https://github.com/hartwigmedical/hmftools>). COBALT, AMBER, and PURPLE were used in tumour-only mode using their default parameters. Notably, PURPLE was used with a fixed parameter value of purity set to 1 for all samples, ensuring consistency in the analysis.

Circularisation for *in vitro* reporting of cleavage effects by sequencing (CIRCLE-seq)

To enrich circular DNA for sequencing, each DNA sample was digested for seven consecutive days with ATP-dependent Plasmid-Safe DNase (Lucigen) to remove linear/chromosomal DNA. Each day 20 units of enzyme and 4 µl of a 25 mM ATP solution were added. After seven days, the DNase was heat-inactivated for 30 minutes at 70°C. The fold change reduction in linear DNA was assessed by qPCR targeting the chromosomal gene *HBB* and the mitochondrial gene *MT-COI*. Amplification of circular DNA was performed with a Phi29 polymerase as described in (Koche *et al.*, 2020). Amplified circular DNAs were then prepared for sequencing. In short, around 550 ng of DNA were sheared to a mean length of around 400-450 base pairs (bp) and subjected to library preparation using the NEBNext Ultra II DNA Library Prep Kit for illumina (NEB), which included sequencing adapter addition, and amplification. DNA Clean-up was performed using the Agencourt AMPure XP magnetic beads. All prepared libraries were sequenced using the Illumina NextSeq500 with the NextSeq 500/550 Mid Output Kit v2.5 (300 Cycles), generating around 10M paired end 150bp reads per sample.

Data processing

Sequencing reads were trimmed for both quality and adaptor sequences using cutadapt (version 3.4) (Martin, 2011). Trimmed reads were aligned to the GRCh38 reference genome using BWA Mem (version 0.7.17-r1188) (Li, 2013).

Identification of sequencing coverage

Sequencing read coverage per 50 bp bin was calculated using deeptools 'bamCoverage' (version 3.5.1) (Ramirez *et al.*, 2014) with default values. For visualisation, the 50 bp read coverage values were combined into 10,000 bp bins using the function 'ScoreMatrixBin' of the genomation (version 1.2.6) R-package (Akalın *et al.*, 2015).

DNA Panel Sequencing

Library preparation was performed using SureSelectXT HS Target Enrichment System (Agilent). Panel pair-end 2x150 sequencing was performed on NextSeq 550 (Illumina). Genes present in the panel are reported in Table S2.

RNA Sequencing (RNA-seq)

RNA from organoids were isolated using the TRIzol® Reagent (Life Technologies), followed by the column based PureLink RNA Mini Kit (Thermo Fisher Scientific). Purified RNA quality was evaluated using RNA 6000 Nano kit on a Bioanalyzer 2100 (Agilent) and only RNA with an RNA Integrity Number (RIN) greater than 9 were used. RNA-seq library were obtained using poly(A) enrichment with TrueSeq Stranded mRNA Library Prep kit (Illumina). Libraries obtained from PDOs at baseline (n = 14, analyses displayed in Figure 1) were sequenced to a depth of 30M fragments and 150 base paired end reads on an Illumina NextSeq 500 sequencer. For comparison between +WR and adapted to -WR PDOs, +WR PDOs were put in -WR for 24 hours prior to RNA collection, to account for the effect of the media. The resulting libraries were sequenced to a depth of 11M fragments for organoids and 75 base paired end reads on an Illumina NextSeq 500 sequencer.

RNA-Seq Analysis

For downstream analyses, the raw counts were normalised using the 'rlog' function of the DESeq2 R-package. Genes with less than a total of 20 counts across all PDOs were removed prior to normalisation. To compare gene expression values across amplicon types, the normalised gene values were Z-score normalised.

Gene Set Enrichment Analysis

Differential gene expression analysis was conducted using 'DESeq2' (Love et al., 2014). Log2 fold change shrinkage was applied using the 'lfcShrink' function in 'DESeq2' with the 'ashr' method (Stephens, 2017). Gene set enrichment analysis (GSEA) was performed using the 'fgsea' R-package (Korotkevich *et al.*, 2021) with the Hallmark pathways database provided by the 'msigdb' R-package (Liberzon *et al.*, 2011).

Subtyping

The subtyping was performed scoring the samples according to the Raghavan signatures (Raghavan et al., 2021) with the gsva function and assigning the subtype according to what signature (basal or classical) achieved the highest score.

Fusion analysis

The nf-core/rnafusion pipeline was used to evaluate gene fusion from our RNAseq data; the pipeline was run under default parameters using all the fusion detection tools provided (arriba, fusioncatcher, pizzly, squid, starfusion and stringtie). Only fusions detected by at least two tools were considered as confident.

Quantitative real time polymerase chain reaction (qRT-PCR) analysis

RNA was isolated as previously described. Reverse transcription of 1 µg of RNA was performed using the TaqMan® Reverse Transcription reagents (Applied Biosystems), and 20 ng of cDNA was used in the PCR reaction. The following TaqMan® probes *HPRT1* (Hs02800695_m1) and *LGR5* (Hs00173664_m1) were used in the project. The following primers (Eurofins) were used with SYBR™ Green PCR master mix (ThermoFisher):

MYC Forward: CCTGGTGCTCCATGAGGAGAG

MYC Reverse: CAGACTCTGACCTTTTGCCAG

GAPDH Forward: ACAGTTGCCATGTAGACC

GAPDH Reverse: TTTTGGTTGAGCACAGG

Relative gene expression quantification was performed using the $\Delta\Delta C_t$ method with the Sequence Detection Systems Software, Version 1.9.1 (Applied Biosystems).

Survival analysis

Patient survival data were utilised for Kaplan-Meier survival analysis. This data encompassed the patients' vital status, the number of days to death or to the last follow-up point. The analysis was performed using the R-packages 'survival' (v3.4-0) and 'survminer' (v0.4.9). Patients who died due to 'Surgical complications' or 'Infection' were excluded from the analysis.

Statistical analyses

All statistical analyses were carried out using R (v4.1.2) or GraphPadPrism (v9.5.1). A Fisher's exact test and Chi Square were used to evaluate the significance in contingency tables. The Wilcoxon rank-sum test was used in two-group comparisons and the relationship between two quantitative variables was measured using the Pearson correlation. Other statistical tests performed are described in the figures or in the figure legends.

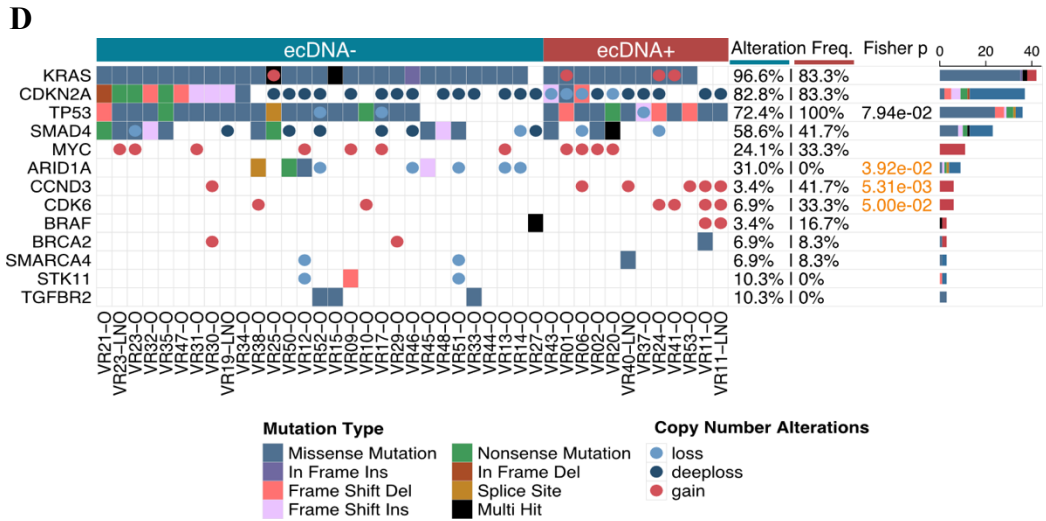
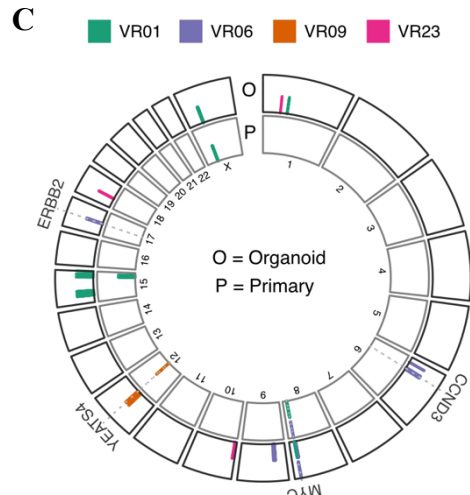
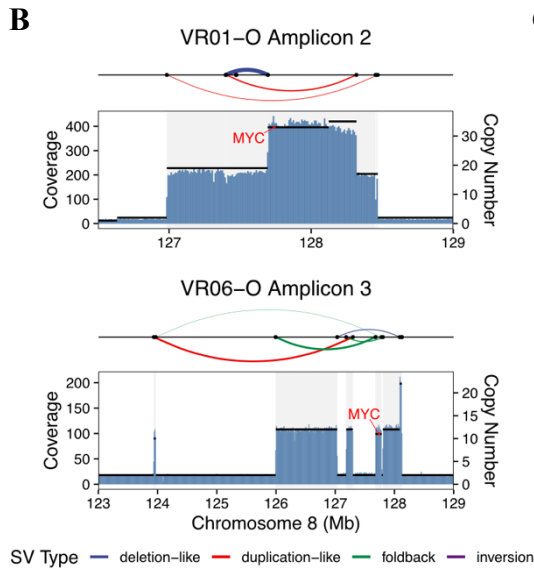
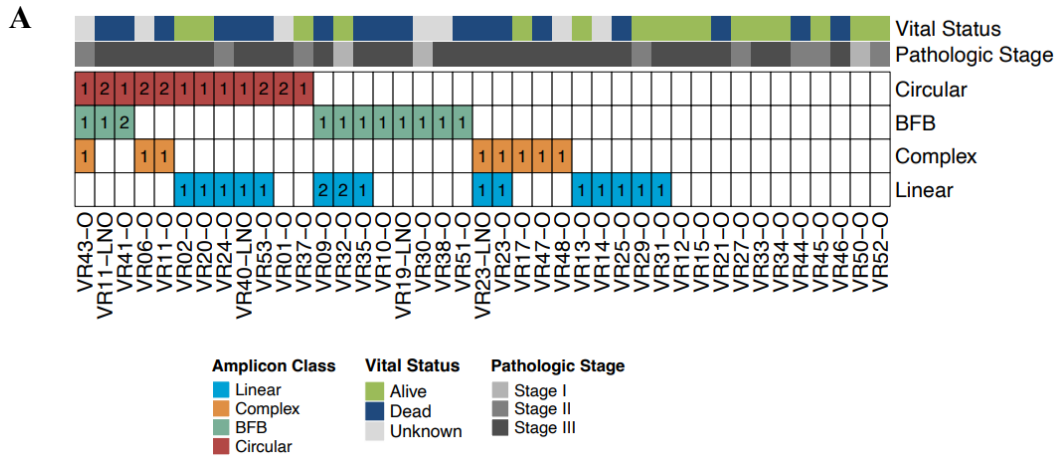
Public Datasets

Amplicon information for the International Cancer Genome Consortium (ICGC) PACA-CA and PACA-AU whole-genome sequencing (WGS) samples were obtained from (Kim et al., 2020). Additional matching ploidy data was retrieved from the ICGC Data Portal (<https://dcc.icgc.org/releases/PCAWG>). To focus on PDAC specifically, only PDAC tumours with histological types '8500/3', '8560/3', '8140/3', 'Adenosquamous carcinoma' and 'Pancreatic Ductal Adenocarcinoma' were used in the downstream analysis.

4.3. Results

ecDNAs are a major source of focal oncogene amplifications in PDAC

To characterise the genomic rearrangements that underpin copy number variation in PDAC, we performed whole genome sequencing (WGS) on 41 early passage Patient-Derived Organoids (PDOs) established from 39 tumours (Table S1). The majority of PDOs were established from treatment naive (38/39) and localised tumours. Histologically, the majority of PDAC tumours from which PDOs were established displayed a conventional morphological pattern (36/39), were mostly defined as classical PDAC (36/39), with two containing squamous elements (defined as adenosquamous), and one classified as a signet-ring tumour (Table S1). Consistent with earlier studies (Boj et al., 2015; Tiriach et al., 2018; Driehuis et al., 2019), PDOs exhibited frequent copy-number alterations in canonical PDAC genes including copy number loss of *CDKN2A*, *TP53*, and *SMAD4* and copy number gains in *KRAS* and *MYC* (Figure S1A). AmpliconArchitect (Deshpande *et al.*, 2019) was used to reconstruct genomic regions associated with high copy number gains classifying them as either linear, break-fusion-bridge (BFB), complex, or circular extrachromosomal DNA (ecDNA) amplicons (Figure 1A). This analysis revealed that 12 out of 41 PDOs harboured at least one distinct ecDNA (Figure 1A). The identification of ecDNAs in PDOs is consistent with earlier whole genome analyses derived from resected PDAC patient material (Kim et al., 2020). We observed higher fractions of tumours bearing amplifications in PDOs (73.17 % vs 66.1 %), including ecDNA amplifications (29.3 % vs 14.2 %), which may be due to increased detection in pure neoplastic populations (Figure S1B). Importantly, the presence of BFB and/or ecDNA amplifications was associated with poor patients' outcomes in our cohort (Figure S1C).



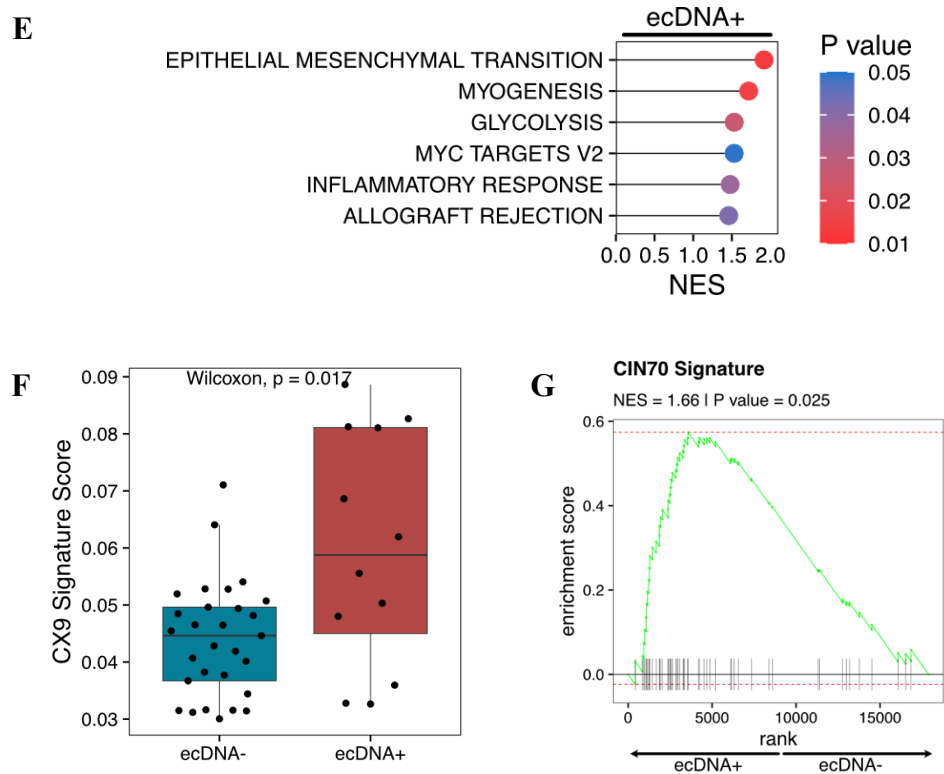


Figure 1. Gene amplification landscape of PDAC. **A.** Amplicon classification based on AA of the 41 PDOs subjected to WGS. Number of identified amplicons for each sample is indicated in the plot. Patients' pathological stage at time of resection and vital status at follow-up is colour coded. **B.** Genomic view of AA reconstructed amplicon structures spanning the *MYC* locus for the organoids VR01-O and VR06-O with *MYC* on circular amplicons. The genomic view shows coverage depth, copy number segments and structural variant (SV) connections (curves above copy number and coverage view). **C.** Circular plot showing that amplicon regions identified in four patients' primary tumours (P) are retained in the matched organoids (O). **D.** Oncoplot showing the altered genes in 41 PDAC PDOs classified as ecDNA+ (red) and ecDNA- (blue). Mutations were identified using targeted sequencing and copy number calls were derived from the WGS data analysis. The types of alterations are colour- and shape-coded. Gain, copy number ≥ 3 ; loss, copy number ≤ 1 , deeploss, copy number ≤ 0.25 . Fisher's exact test was utilised to identify associations with genomic alterations in specific genes and ecDNA+ or ecDNA- status. P values below 0.1 are displayed and significance (p value < 0.05) is highlighted in orange. **E.** Lollipop plot showing gene set enrichment analysis (GSEA) results focused on Hallmark pathways that are significantly enriched among ranked differentially expressed genes of ecDNA+ PDOs compared to ecDNA- PDOs (n = 7). **F.** Box plot showing the CX9 chromosomal instability signature enriched in ecDNA+ compared to ecDNA- PDOs. Statistical significance was evaluated using a Wilcoxon rank-sum test. **G.** Gene set enrichment analysis (GSEA) of differentially expressed genes between ecDNA+ (n = 7) and ecDNA- (n = 7) PDOs in the CIN70 transcriptomic signature.

CCND3 and *MYC* were the most recurrently amplified genes in our cohort of PDOs, while linear amplicons were the most common AA-reconstructed amplicon type (Figure 1A and Figure S1D). Amplifications of *CCND3* were identified in 6 out of 41 PDOs and described as either circular, BFB, or complex amplicons (Figure S1D-E). Amplifications of *MYC* were identified in 11 PDOs with 2 PDOs harbouring *MYC* on ecDNA (Figure 1B). Circularisation for *in vitro* reporting of cleavage effects by sequencing (CIRCLE-seq) (Tsai *et al.*, 2017) validated the circular amplicon containing *MYC* in VR01-O (Figure S2A). *MYC* ecDNAs were derived from contiguous genomic regions on chromosome 8 comprising *MYC* and adjacent genes *PVT1* and *CASC11*. AA analysis of four primary PDAC samples with matched PDOs demonstrated that the structure of PDO *MYC* ecDNA amplicons between parental tissue and derived PDOs were highly concordant (Figure 1C and Figure S2B).

To link patterns of ecDNA gene amplification to key mutational drivers, we performed high-coverage targeted sequencing (Table S2). PDOs containing ecDNAs displayed bi-allelic inactivation of *TP53* (Figure 1D) and were enriched for copy number loss of *CDKN2A* on chromosome 9 and for copy number gains on chromosomes 6 (*CCND3*) and 7 (*CDK6*) (Figure 1D and Figure S2C). Moreover, the presence of an ecDNA was inversely associated with inactivating alterations of the TGF β pathway (Figure S2D). Whole genome duplications were also more frequently observed in PDOs harbouring an ecDNA (Figure S2E). Consistent with earlier findings (Turner *et al.*, 2017; Wu *et al.*, 2019), genes residing on ecDNAs exhibited significantly elevated levels of expression when compared to those associated with other amplicon types (Figure S2F).

Gene expression programmes commonly linked to biologically aggressive tumours, such as Epithelial-to-Mesenchymal Transition and glycolysis, were significantly enriched in ecDNA PDOs (n = 7) as opposed to non-ecDNA PDOs (n = 7) (Figure 1E). ecDNA⁺ PDOs were also enriched for copy number signatures defining patterns of mid-level amplifications which have been associated with replication

stress (CX9, Figure 1F) (Drews *et al.*, 2022). Endogenous replication stress can cause genomic instability which in turn may result in ecDNA formation (Takahashi *et al.*, 2022). Consistent with this idea, ecDNA+ PDOs showed enrichment for a transcriptomic signature (CIN70) of chromosomal instability (Carter *et al.*, 2006) (Figure 1G). Overall, we found a heterogeneous landscape of genomic amplifications in PDOs and that ecDNA tumours display features of a more biologically aggressive disease.

ecDNAs are a major source of *MYC* intratumor heterogeneity

To understand how ecDNA might contribute to PDAC intratumor heterogeneity, we focused on *MYC* amplifications representing either extra- (*ecMYC*) or linear intra-chromosomal amplification (*icMYC*). The two high-level amplifications of *MYC* identified in our cohort were predicted to reside on ecDNAs for both PDOs and paired primary tissues (Figure S3A). Next, we performed DNA FISH for *MYC* and *Centromere 8 (CEN8)* on metaphase spreads from the two *ecMYC* and from three *icMYC* PDOs. None of the metaphase spreads from the *icMYC* PDOs contained *MYC* positive ecDNAs (Figure S3B). In contrast, ten to hundreds of individual *MYC* positive ecDNA per nucleus were observed in metaphases prepared from the *ecMYC* PDOs (Figure 2A). Next, we examined interphase nuclei to observe the spatial organisation of FISH positive signals and estimate the cell-to-cell variation for the number of *MYC* copies. In the *ecMYC* PDOs, FISH positive signals tended to cluster in defined regions of the nucleus (Figure 2B). Compared to *icMYC* PDOs (Figure S3B), *ecMYC* PDOs displayed a more heterogeneous distribution of *MYC* amplifications per cell (Figure 2B). Significant variability of *MYC* copy-number states was even observed in individual organoids (Figure 2C). We then analysed the primary tissues from which the PDOs were established and confirmed the significant cell-to-cell variation of *MYC* FISH foci in the ecDNA bearing tumours (Figure 2D). In agreement with existing literature, the presence of ecDNA was associated with higher mRNA levels of *MYC* in the *ecMYC* PDOs (Figure S3C) and *MYC* protein expression in paired primary tissues (Figure S3D). Altogether,

our data indicate that ecDNA contribute to extensive copy-number intratumor heterogeneity and drive higher *MYC* expression in PDAC tissues.

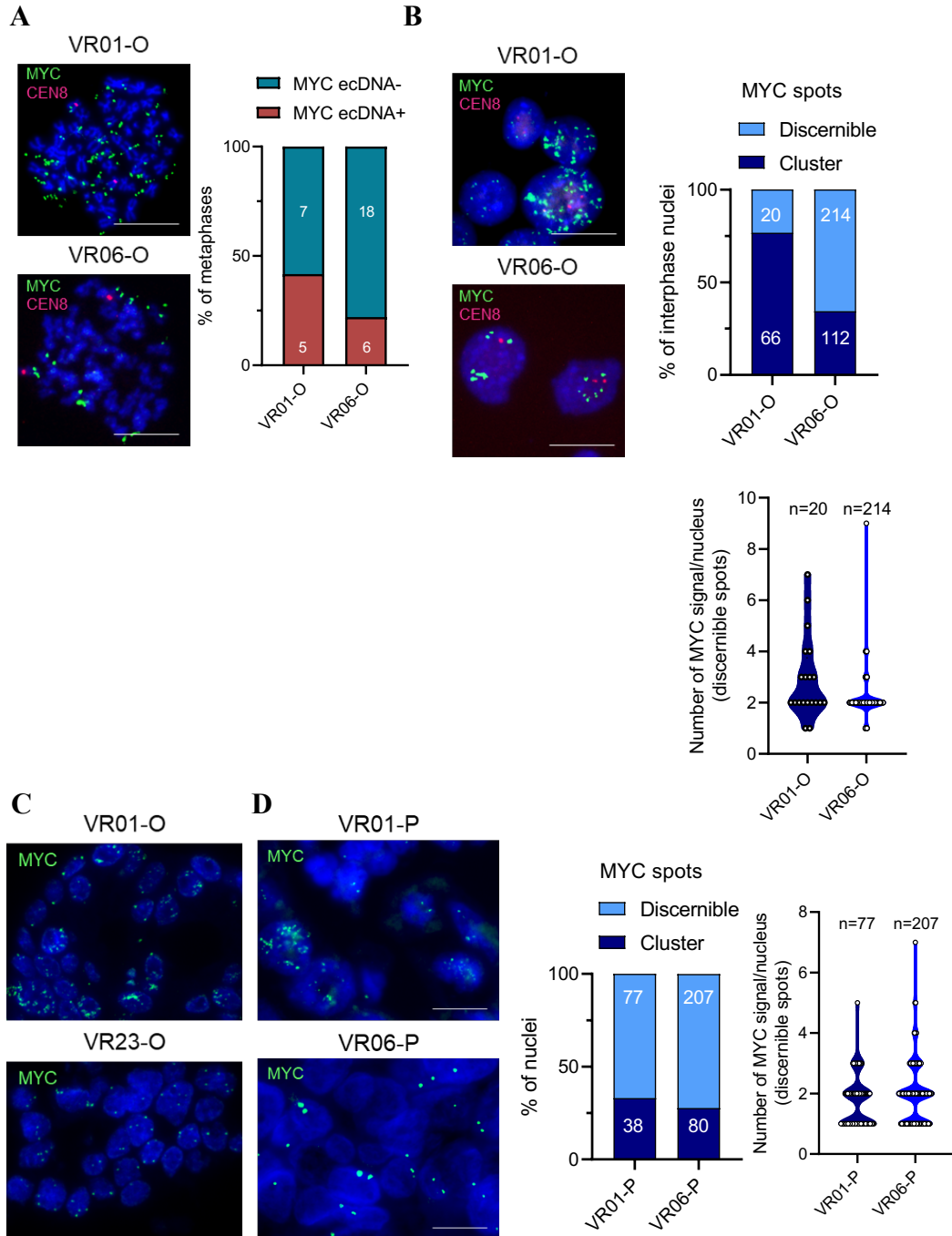


Figure 2. ecDNA promotes intratumor heterogeneity of *MYC* copy number in PDAC. A. Representative FISH images validating the presence of *MYC* on ecDNA in VR01 and VR06 PDOs. Scale bar: 20 μ m (left). Stacked bar plot displaying the frequency of ecDNA+ metaphase spreads in VR01-O and VR06-O (right). **B.** Representative FISH images of interphase nuclei of VR01-O and VR06-O. Scale bar: 20 μ m (left). Frequency of clustered *MYC* spots in interphase nuclei (right).

Quantification of discernible *MYC* spots per nucleus is provided on the bottom. C. Representative FISH images of one *ecMYC* (VR01-O, top) and one *icMYC* (VR23-O, bottom) embedded organoids. D. Representative FISH images of embedded VR01 and VR06 primary tissues (P). Scale bar: 20 μm (left). Frequency of clustered *MYC* spots in primary tumours' nuclei (middle). Quantification of discernible *MYC* spots per nucleus is provided on the right.

ecDNA amplifications of *MYC* drive rapid adaptation to stress

Next, we sought to understand how oncogene-bearing ecDNA dynamically respond to microenvironmental stressors. We took advantage of the well-known dependency of PDAC PDOs on WNT-signalling to impose an artificial selective pressure by removing WNT3A and RSPO1 (Boj et al., 2015; Seino et al., 2018) from PDO growth media. ecDNA dynamics were then assessed before and after WNT and RSPO removal (Figure 3A). In agreement with previous work (Seino et al., 2018), none of the PDOs tested ($n = 9$) survived serial passaging in a culture medium lacking both WNT3A and RSPO1 (-WR, Figure S4A). *MYC* is a well-established WNT pathway target gene (He *et al.*, 1998) and *MYC* expression was rapidly induced in PDOs treated with WNT agonists (Figure S4B). Strikingly, we found that *MYC* overexpression was sufficient to bypass the requirement of exogenous WNT3A/RSPO in PDO culture medium (Figure S4C-D). These results implicated *MYC* as an important driver of WNT-gated survival in PDOs. Therefore, we cultivated *ecMYC* ($n = 2$), *icMYC* ($n = 3$), and an individual non-*MYC* amplified PDO in the absence of WR (Figure 3A). All PDOs were established from classical PDAC except for the non-*MYC* amplified PDO (VR09-O), which was derived from a tumour containing signet-ring cells.

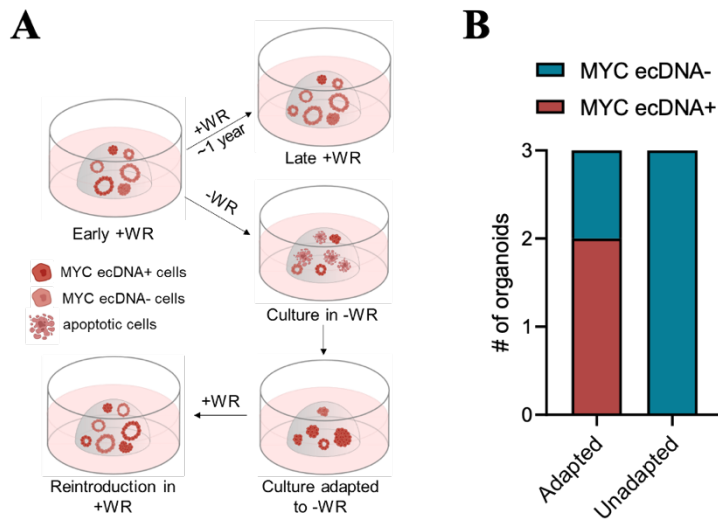
The withdrawal of WR from the medium led to the rapid extinction of three cultures, including two with low-level copy number gains of *MYC* (VR02 and VR20). Conversely, the two *ecMYC* and one *icMYC* PDOs consistently adapted (aPDOs) to the niche-factors depleted conditions (Figure 3B). Then, we performed a detailed molecular characterisation of both parental and adapted PDOs. To minimise the confounding effect of the organoid culture medium (Raghavan et al., 2021), both parental and adapted PDOs were cultivated in the same medium lacking WR and TGF- β /BMP inhibitors (A83-01 and Noggin) before RNA-seq analysis and immunophenotyping. The integrated analysis of genomic and transcriptomic data

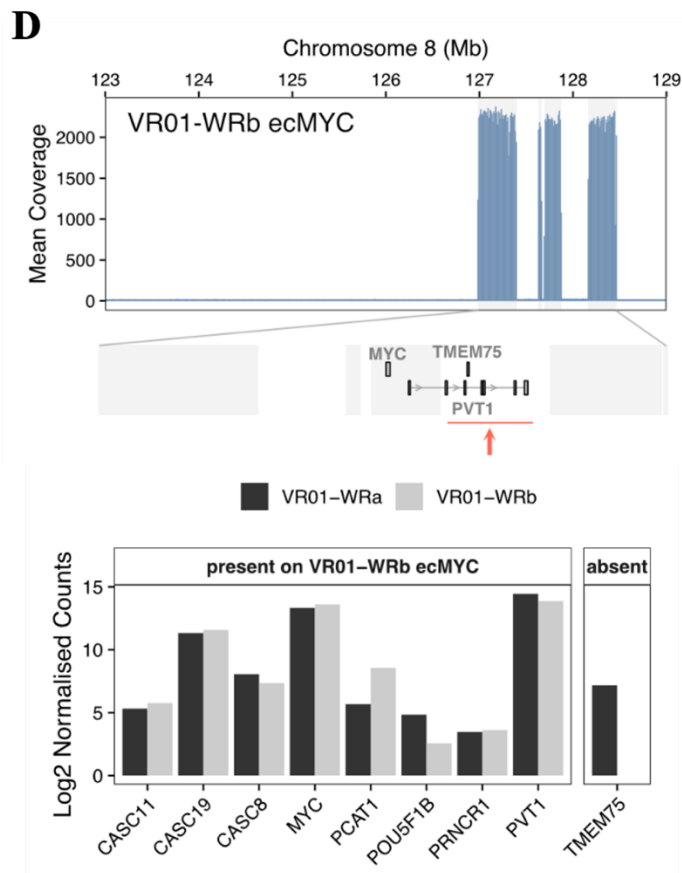
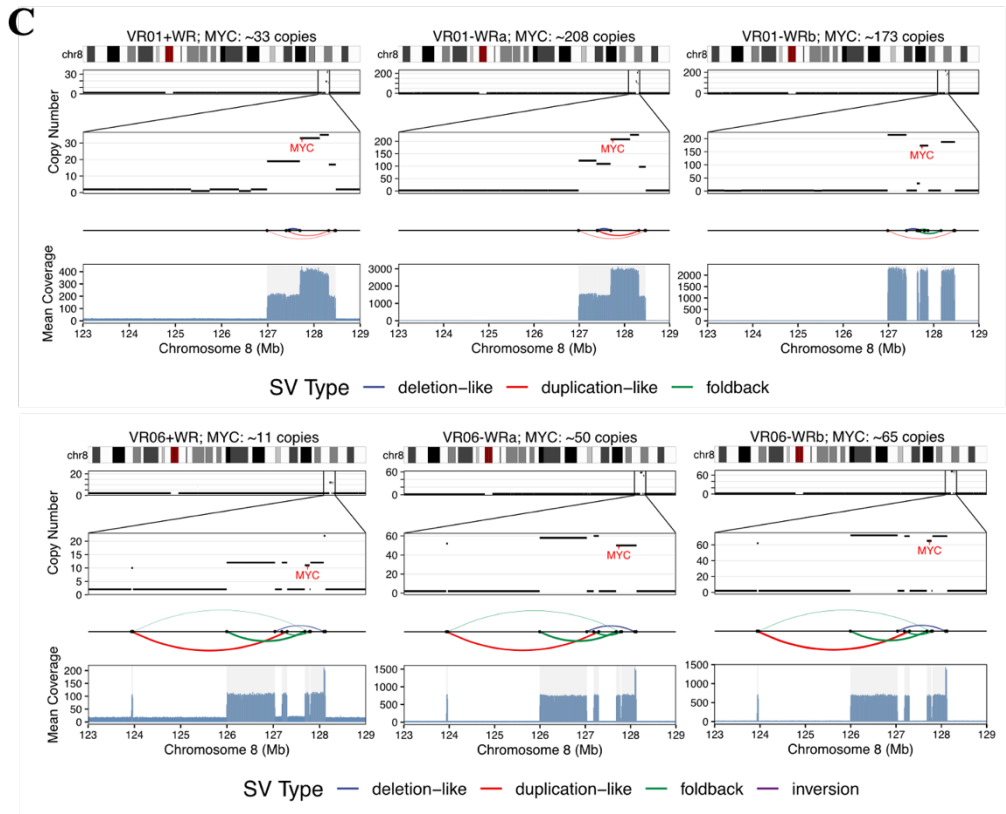
excluded that PDOs adaptation to WR withdrawal was associated with alternative activation of the WNT pathway (Figures S4E-I). Previous work has established that PDOs can create their own niche through the endogenous production of Wnt ligands (Seino et al., 2018). To further confirm niche independence for the adapted PDOs, we treated PDOs with the porcupine inhibitor C59, which blocks endogenous production of biologically active Wnt ligands. In keeping with the niche independence, the adapted PDOs were completely insensitive to porcupine inhibition (Figure S4J).

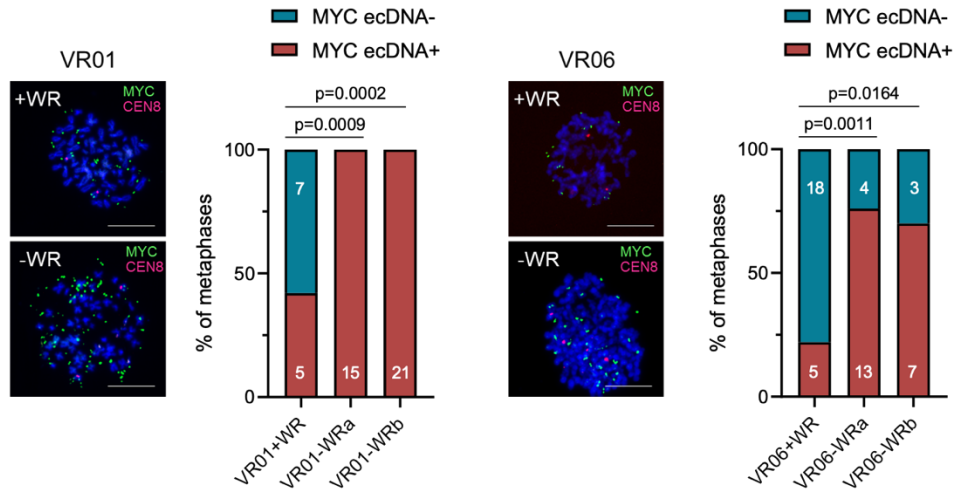
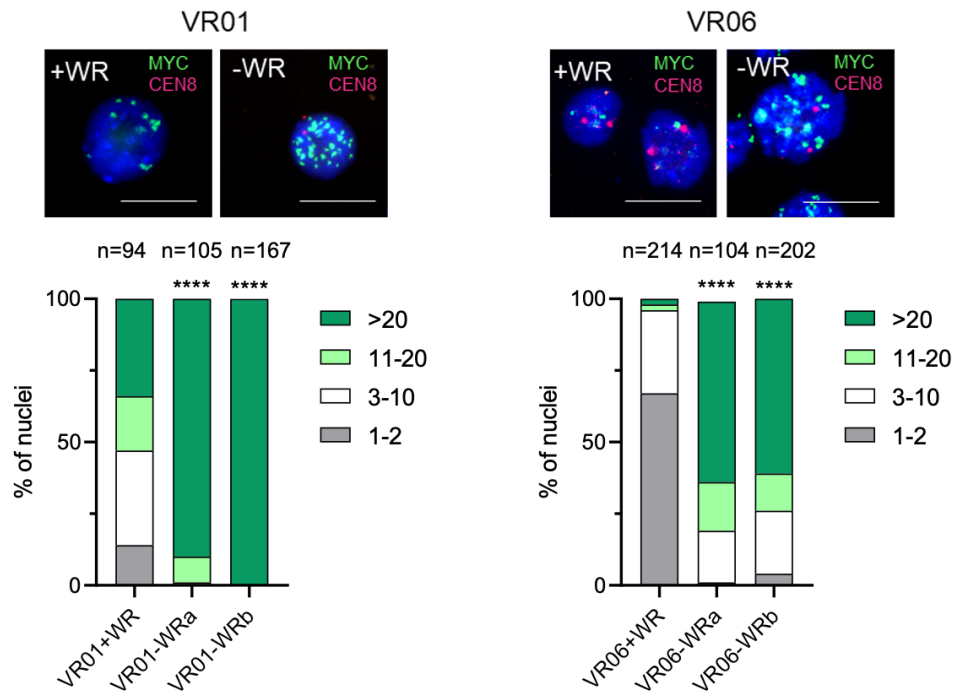
To determine how the microenvironmental stress affected chromosomal and extrachromosomal *MYC* dynamics, we initially applied AA to WGS from two adapted cultures from each PDOs (Figure 3C and Figure S5A). EcDNA containing *MYC* persisted in adapted PDOs, increased their integer copy number, and in one instance evolved its structure. No evidence for circular amplicons was found in VR23-O (*icMYC* PDO) (Figure S4A). The AA-reconstructed circular amplicons for the adapted VR06-O were highly concordant with the circular amplicon described for the parental culture. Compared to the circular amplicon described in the parental culture and persisting in one of the aPDO, an individual genomic locus (*TMEM75*) was not included in the ecDNA structure described in VR01-WRb (Figure 3D). Accordingly, RNA-seq did not detect expression of *TMEM75* in the corresponding aPDO (Figure 3D).

The accumulation of *MYC*-containing ecDNA in aPDOs was confirmed by FISH on metaphase spreads. Every metaphase and almost all the metaphase spreads from the adapted VR01-O and VR06-O, respectively, exhibited copy number accumulation of ecDNAs (Figure 3E). The adaptation was also associated with a dramatic increase in the mean *MYC* copy-number and per cell-distribution which indicates that the ecDNA is under positive selection (Figure 3F). In the *icMYC* PDO, adaptation was associated with either a mild increase in *MYC* copy-number (VR23-WRa) or polysomy of chromosome 8 (VR23-WRb) (Figure S5B) in the absence of changes in ploidy (Figure S5C). Upregulation of *MYC* at mRNA and protein levels in adapted PDOs was consistent with increased *MYC* copy-number and was more dramatic in *ecMYC* than *icMYC* PDO (Figure S5D-E).

We then compared RNA-seq data from parental and adapted *ecMYC* PDOs to gain further insights into the transcriptional changes associated with the accumulation of ecDNAs. For almost all genes on the ecDNA amplicons, the increased mRNA levels in adapted organoids mirrored the increased ecDNA copy-number (Figure 3G). However, the effect size for the increase of *MYC* and other genes between the two cultures was not always consistent with the predicted copy-number changes, suggesting additional regulatory mechanisms controlling gene expression. A known tumour suppressor element that acts *in cis* to reduce *MYC* expression is the promoter of the long-noncoding RNA *PVT1* (Cho *et al.*, 2018). The AA-predicted structure for the *MYC* ecDNA in VR06-O lacked the promoter and the first exons of *PVT1*, thereby providing an explanation for the higher level of *MYC* in VR06-O as compared to VR01-O (Figure 3G). Based on our results, we postulated that *MYC* on ecDNA would enable more rapid adaptation than possible through chromosomal inheritance. Therefore, we cultivated parental PDOs in WR depleted media and monitored the dynamics of niche independency acquisition. Consistent with the rapid accumulation of ecDNA and the increase in *MYC* output, the adaptation to the imposed stress was more rapid for VR06 (Figure 3H).





E**F**

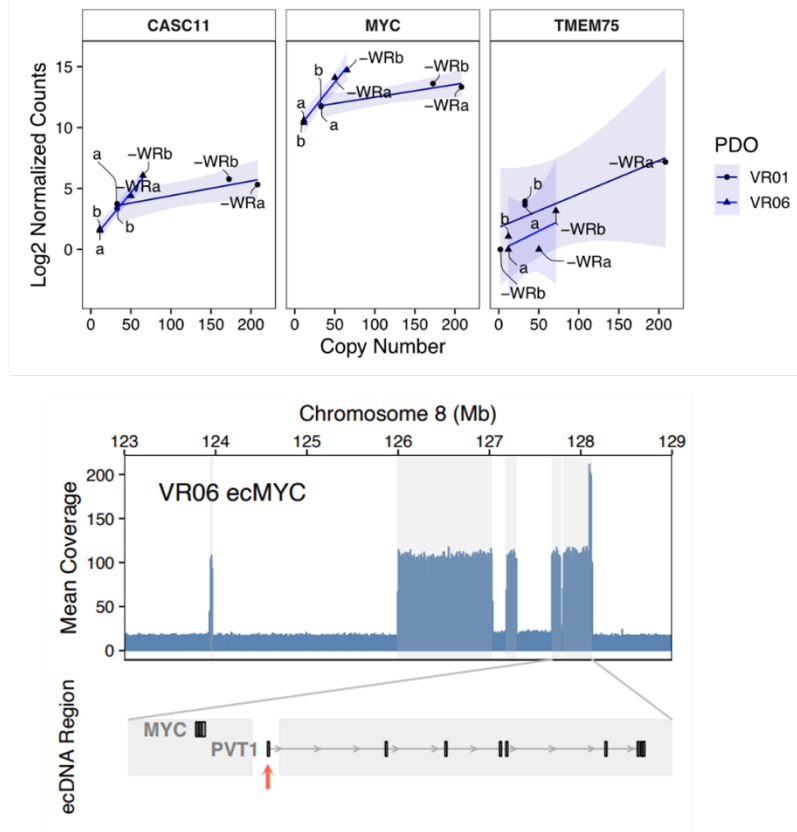
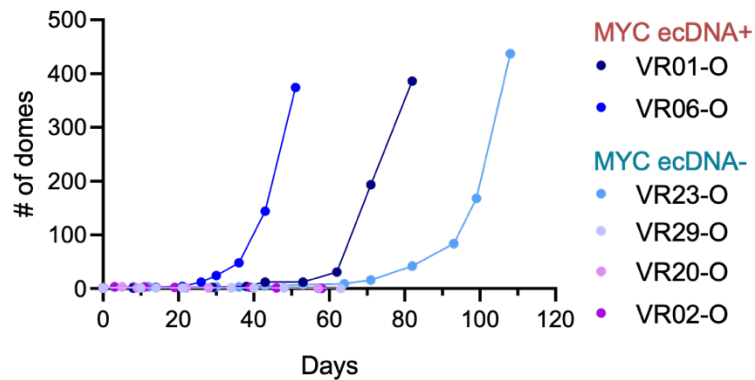
G**H**

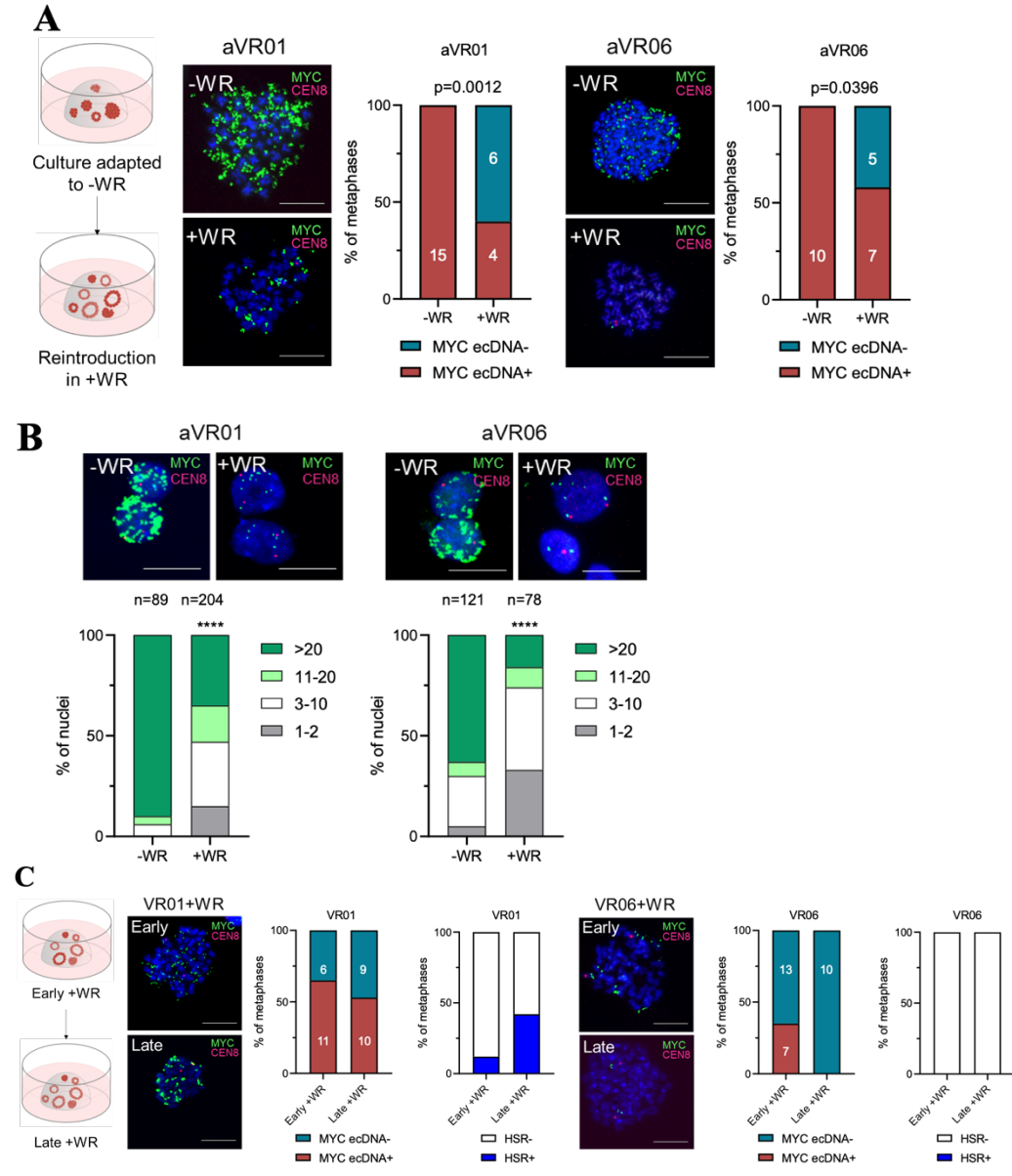
Figure 3. Extrachromosomal *MYC* promotes rapid adaptation to niche factors withdrawal. A. Schematic representation of the experimental workflow. **B.** Stacked bar plot displaying proportion of PDOs, classified as *MYC* ecDNA+ or *MYC* ecDNA-, that did or did not adapt to grow in depleted media. **C.** Copy number alterations on chromosome 8 with a focus on *MYC* region, of ec*MYC* organoids, VR01 (top) and VR06 (bottom), at baseline (+WR) and adapted to depleted media (-WR, 2 biological replicates). SVs that connect amplified regions and form ecDNA and WGS Coverage are displayed below the copy number levels. **D.** Structural difference between putative ecDNAs in VR01-WRa and VR01-WRb (top). The evolved ecDNA structure of VR01-WRb lacks the gene

TMEM75. Log2 normalised expression levels of genes that are either present or absent on the ecDNA in VR01-WRb as compared to VR01-WRa (bottom). **E.** Representative FISH metaphases images for VR01 (left) and VR06 (right), at baseline (+WR) and after adaptation to depleted media (-WR). Scale bar: 20 μ m. The stacked bar plots show the frequency of *MYC* ecDNA+ metaphases at baseline and after adaptation (two biological replicates). P value was calculated using Fisher's exact test. **F.** Representative FISH interphases images for VR01 (left) and VR06 (right) at baseline (+WR) and after adaptation to depleted media (-WR). Scale bar: 20 μ m. Quantification is provided as frequency of nuclei with different ranges of *MYC* spots. ****, $p < 0.0001$ as determined by Chi-square. **G.** Copy number and expression levels of the genes *MYC*, *CASC11*, and *TMEM75*, in VR01 and VR06 at baseline (a, b) and after adaptation (-WRa, -WRb) (top). Genomic view of VR06 ec*MYC* segments (highlighted in grey) and the location of *MYC* and *PVT1*. The *PVT1* starting region is absent on the VR06 ec*MYC*. **h.** Growth curve of *MYC* ecDNA+ (n = 2) and *MYC* ecDNA- (n = 4) organoids in -WR media. Culture growth is represented as number of domes (50 μ l Matrigel/dome).

Maintenance of ec*MYC* in PDAC organoids

EcDNAs can be lost by cancer cells in the absence of a selective pressure or upon microenvironmental changes (i.e., drug treatment) that impose negative fitness (Haber and Schimke, 1981; Schulte *et al.*, 2012; Nathanson *et al.*, 2014; Lange *et al.*, 2022). Elimination of ecDNA can occur through the integration of an ecDNA into a chromosomal location to form a homogeneously staining region (HSR) (Carroll *et al.*, 1988; Ruiz and Wahl, 1990; Nathanson *et al.*, 2014), which are considered as a latent reservoir of ecDNAs. Therefore, we assessed whether ecDNAs are selectively maintained by reversing the selective pressure imposed on PDOs. We reintroduced WR in the culture medium of aPDOs and performed long-term passaging (over one year of continuous culture) of parental PDOs in standard medium. After few passages (~5) in a medium supplemented with WR, we observed a rapid decrease in the number of metaphases containing *MYC* on ecDNA and accordingly of the mean *MYC* copy-number and per cell distribution in aPDOs (Figure 4A and B). Following extensive cultivation of parental PDOs in standard organoid medium, *MYC* containing ecDNAs were lost (VR06-O) or substantially reduced (VR01-O) (Figure 4C and D). The reduction of ecDNA in VR01-O was associated with the emergence of HSR (Figure 4C), which were instead not observed in VR06-O. Accordingly, the reintroduction of the selection pressure (i.e., WR withdrawal) to the high-passage VR06-O cultures led to rapid extinction of the

culture after few weeks with no evidence for the generation of ecDNA containing *MYC* (Figure 4E). Altogether, our results suggest that the loss of the selective pressure can have different outputs on ecDNA-containing cells.



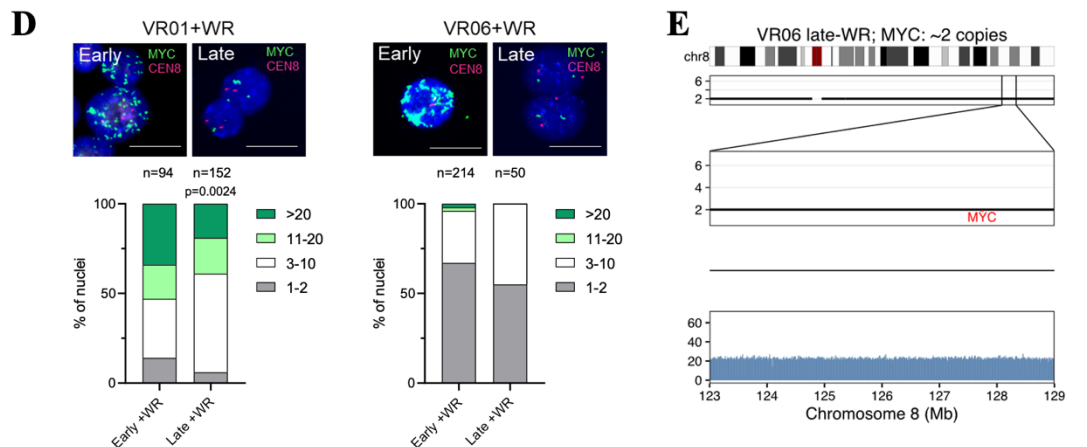


Figure 4. Depletion of ecDNA from PDOs culture upon removal of selection pressure. A. Representative FISH metaphase for adapted VR01 and VR06 (aVR01 and aVR06) cultured in +WR media for five passages, -WR condition is used as control. Scale bar: 20 μ m. Quantification is provided as changes in frequency of *MYC* ecDNA+ metaphase spreads. Significance was assessed by Fisher's exact test. **B.** Representative FISH interphases for aVR01 and aVR06 cultured in +WR media for five passages, -WR condition is used as control. Scale bar: 20 μ m. Quantification is provided as frequency of nuclei with different range of *MYC* spots. ****, $p < 0.0001$ by Chi-square. **C.** Representative FISH metaphase for VR01-O and VR06-O cultured in +WR at early and late passages. Scale bar: 20 μ m. Quantification is provided as changes in frequency of *MYC* ecDNA+ and HSR+ metaphases. **D.** Representative FISH interphases for VR01-O and VR06-O cultured in +WR at early and late passages. Scale bar: 20 μ m. Quantification is provided as frequency of nuclei with different range of *MYC* spots. Significance was assessed by Chi-square **E.** Copy number alterations on chromosome 8 with a focus on *MYC* region, of VR06 late passage after few passages in depleted media (-WR). WGS Coverage is displayed below the copy number level.

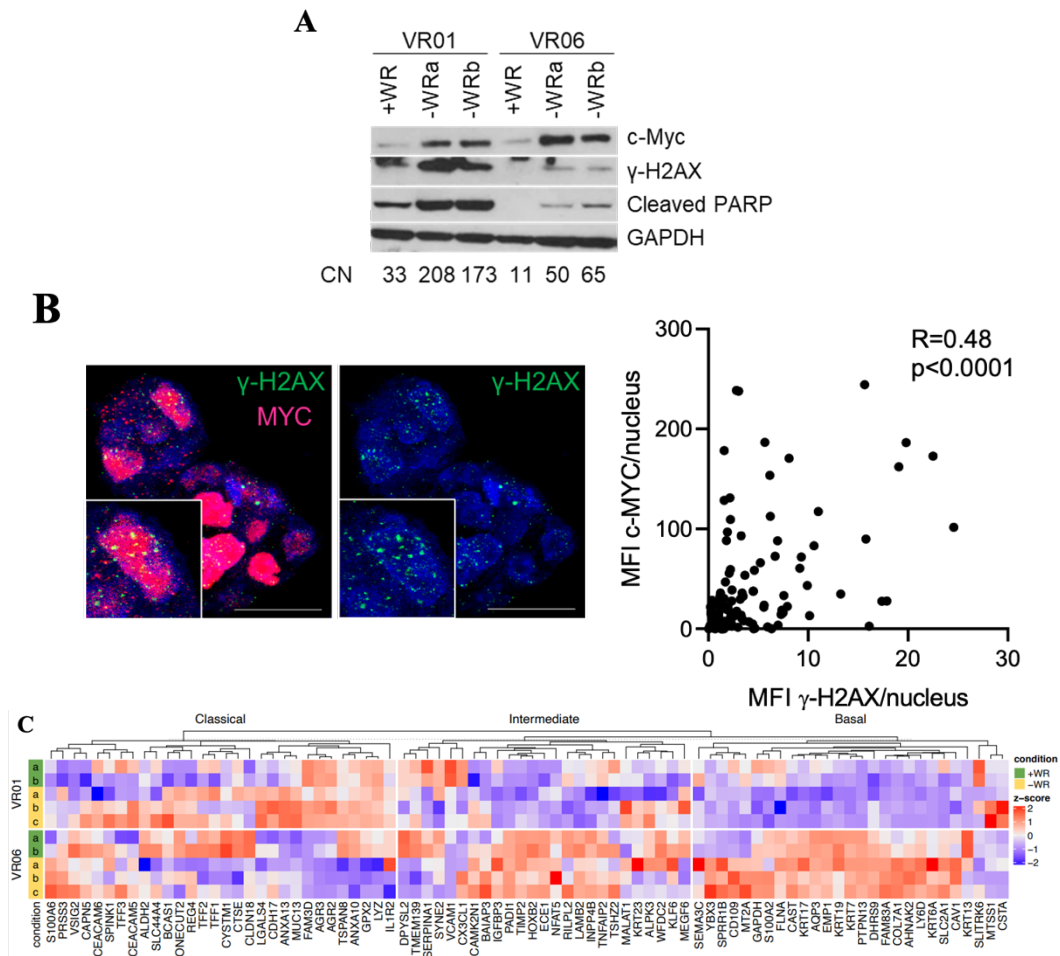
ecDNAs and cell phenotypes in PDAC

Both immunophenotyping (Figure S6A) and pathway analysis from RNA-seq data demonstrated reduced proliferation index for PDOs with accumulation of ecDNAs (Figure S6B). Together with the observation that ecDNA are spontaneously lost in the absence of or upon neutralisation of the selection pressure, our results suggest a fitness cost for the maintenance of *MYC* on extrachromosomal DNA in PDOs. EcDNA driven cancer cells have been shown to display increased levels of phosphorylated histone H2AX (Takahashi *et al.*, 2022), which is required for the assembly of DNA damage response as well as for the activation of checkpoint proteins which might arrest cell cycle progression (Turinetto and Giachino, 2015).

Moreover, anti-neoplastic treatments known to activate the DNA damage sensing machinery have been shown to promote the loss of ecDNA through yet uncharacterised mechanism (Von Hoff, 1991; Raymond *et al.*, 2002; Schoenlein *et al.*, 2003). In PDOs, the levels of phosphorylated H2AX (γ H2AX) was positively correlated with ecDNA copy-number but not with *MYC* levels (Figure 5A). Accordingly, the reduction of ecDNA copies due to the removal of the imposed artificial selection was associated with reduced levels of γ H2AX (Figure S6C). In a heterogeneous organoid culture, *MYC* protein expression might serve as a proxy for *ecMYC* copy number. We found that γ H2AX foci were particularly prominent in *MYC*^{high} nuclei and *MYC* expression positively correlated with the intensity of γ H2AX staining (Figure 5B). Nonetheless, neither the forced overexpression of *MYC* through a lentiviral vector nor the adaptation of a non *ecMYC* PDOs induced elevation of γ H2AX in PDOs (Figure S6D-E). EcDNA copy-number also correlated with increased levels of the apoptotic marker cleaved PARP (cPARP) (Figure 5A), thereby suggesting that accumulation of ecDNA might not be beneficial for cancer cells unless providing a survival advantage.

We then sought to assess the phenotypic consequences of ecDNA accumulation in PDAC organoids. The aPDOs bearing *ecMYC* and displaying the highest *MYC* expression showed marked morphological changes (Figure S7A). As opposed to the *icMYC* PDOs (VR23), the two *ecMYC* PDOs lost their characteristic cystic-like structure to display a solid growth pattern with cytological sign of less differentiated tumours (Figure S7A). In agreement with previous studies (Hung *et al.*, 2021; Zhu *et al.*, 2021), targeting of *MYC* transcription with 500nM of the BRD4 inhibitor JQ1 (Delmore *et al.*, 2011) dramatically reduced *MYC*-ecDNA interphase hubs (Figure S7B) and lowered the level of *MYC* mRNA (Figure S7C) in *ecMYC* aPDOs. Conversely, levels of *MYC* were almost unaffected by the JQ1 treatment in the *icMYC* aPDOs (Figure S7C). Furthermore, JQ1 preferentially reduced cell viability of *ecMYC* PDOs over *icMYC* PDO (Figure S7D). Elevated *MYC* expression and *MYC* related gene programs are significantly enriched in tumours with basal-like/squamous identity (Bailey *et al.*, 2016; Hayashi *et al.*, 2020). Therefore, we evaluated whether *ecMYC* accumulation affected the cell states of the adapted PDOs. The accumulation of *ecMYC* was not associated with shifts in PDO cell

states (Figure 5C). The accumulation of *ecMYC* rather strengthened the classical and the basal programs (Moffitt et al., 2015; Raghavan et al., 2021). in VR01-O and VR06-O, respectively (Figure 5D). Conversely, adaptation of *icMYC* PDO to WR withdrawal was associated with more dramatic changes in cell states (Figure S6D). Changes in transcriptional cell states were concordant with immunophenotypic data, with the PDOs displaying the highest *MYC* dosage (VR06) showing expression, although heterogeneous, of squamous markers (CK5 and Δ Np63) and reduction of the classical marker GATA6 compared to the parental culture (Figure 5E and 5F). In summary, *ecMYC* dosage had cell context dependant effects.



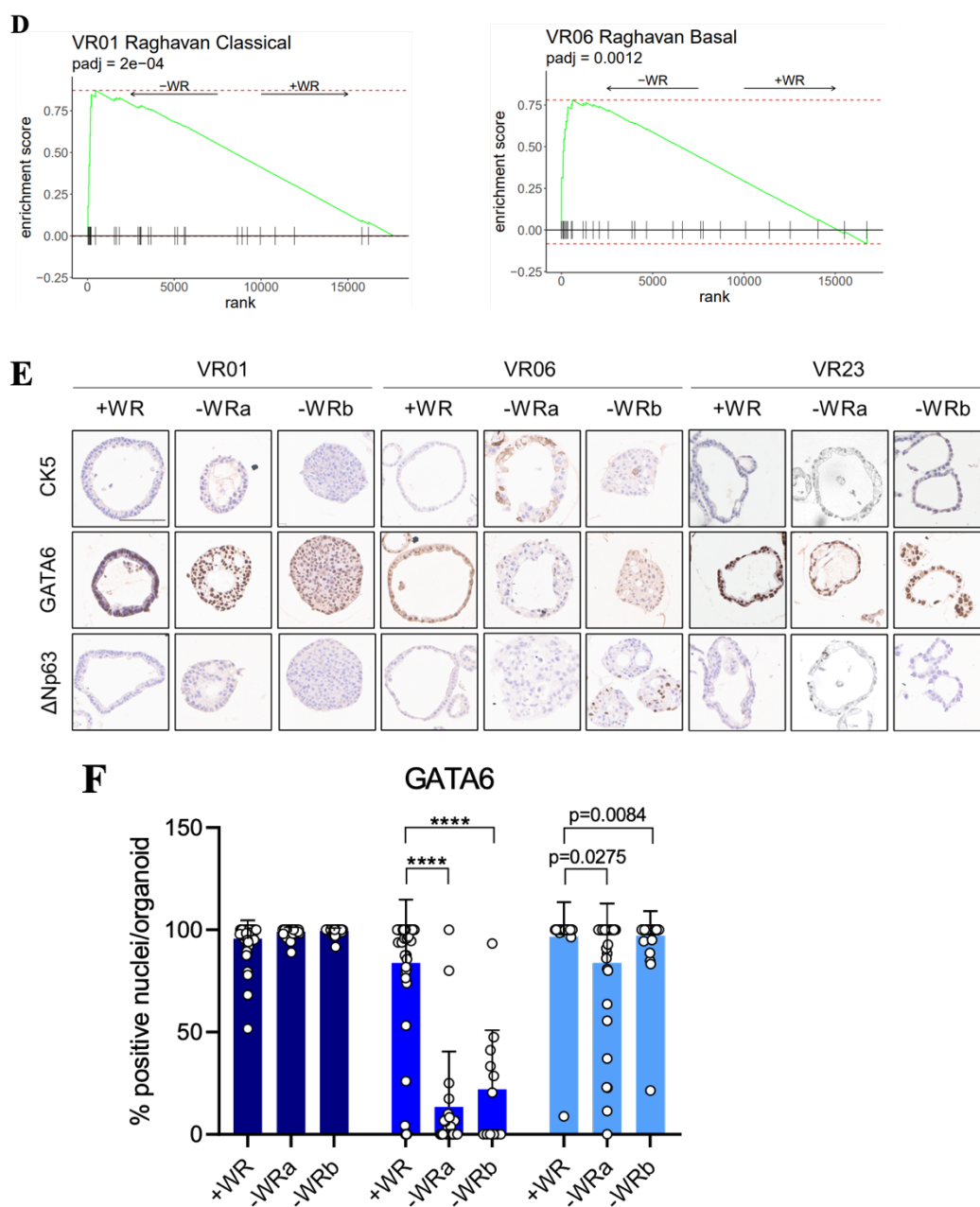


Figure 5. MYC levels and neoplastic cell states. **A.** Immunoblot analysis in whole cell lysate of *ecMYC* organoids at baseline and after adaptation to -WR. GAPDH was used as loading control. CN: WGS-based copy number. **B.** Representative confocal microscopy images of anti-c-Myc and anti- γ H2AX immunofluorescence in one *ecMYC* organoid at baseline. Scale bar: 20 μ m. Pearson R coefficient was used to calculate the correlation between the mean fluorescent intensity (MFI) of c-Myc and γ -H2AX. **C.** Heatmap displaying the expression of Classical, Intermediate, and Basal genes from Raghavan et al. (Raghavan et al., 2021) in baseline (two biological replicas) and adapted (three biological replicas) *ecMYC* organoids. **D.** Gene set enrichment analysis (GSEA). Left panel, enrichment of Classical gene set from Raghavan et al. (Raghavan et al., 2021) computed over the

ranked lists of VR01 differentially expressed genes, derived from the comparison of -WR and +WR samples. Right panel enrichment of Basal gene set from Raghavan et al. (Raghavan et al., 2021) computed over the ranked lists of VR06 differentially expressed genes, derived from the comparison of -WR and +WR samples. **E.** Representative immunohistochemistry for cytokeratin 5 (CK5), GATA6, and Δ Np63 of parental (+WR) and adapted (-WR) organoids. Scale bar: 100 μ m. Quantification for GATA6 is provided in **F** as frequency of GATA6⁺ nuclei per organoid, at least 20 organoids were analysed for each condition.

4.4. Discussion

Intratumor heterogeneity and phenotypic plasticity drive tumour progression and therapy resistance. Oncogene dosage variation contributes to cell state transition and phenotypic heterogeneity (Bielski *et al.*, 2018; Mueller *et al.*, 2018; Marusyk, Janiszewska and Polyak, 2020), thereby providing a substrate for somatic evolution. Nonetheless, the genetic mechanisms underlying phenotypic heterogeneity are still poorly understood. While the transcriptional output of an oncogene can be specified by either genetic or non-genetic mechanisms, oncogenic activation is often driven by focal amplifications (Beroukhim *et al.*, 2010). ecDNAs are emerging as important mediators of intratumor heterogeneity and therapy resistance in cancer (Lange *et al.*, 2022). Thousands of ecDNA copies may accumulate in a cancer cell and supercharge oncogene expression due to increased chromatin accessibility and enhancer hijacking (Sihan Wu *et al.*, 2019; Hung *et al.*, 2021).

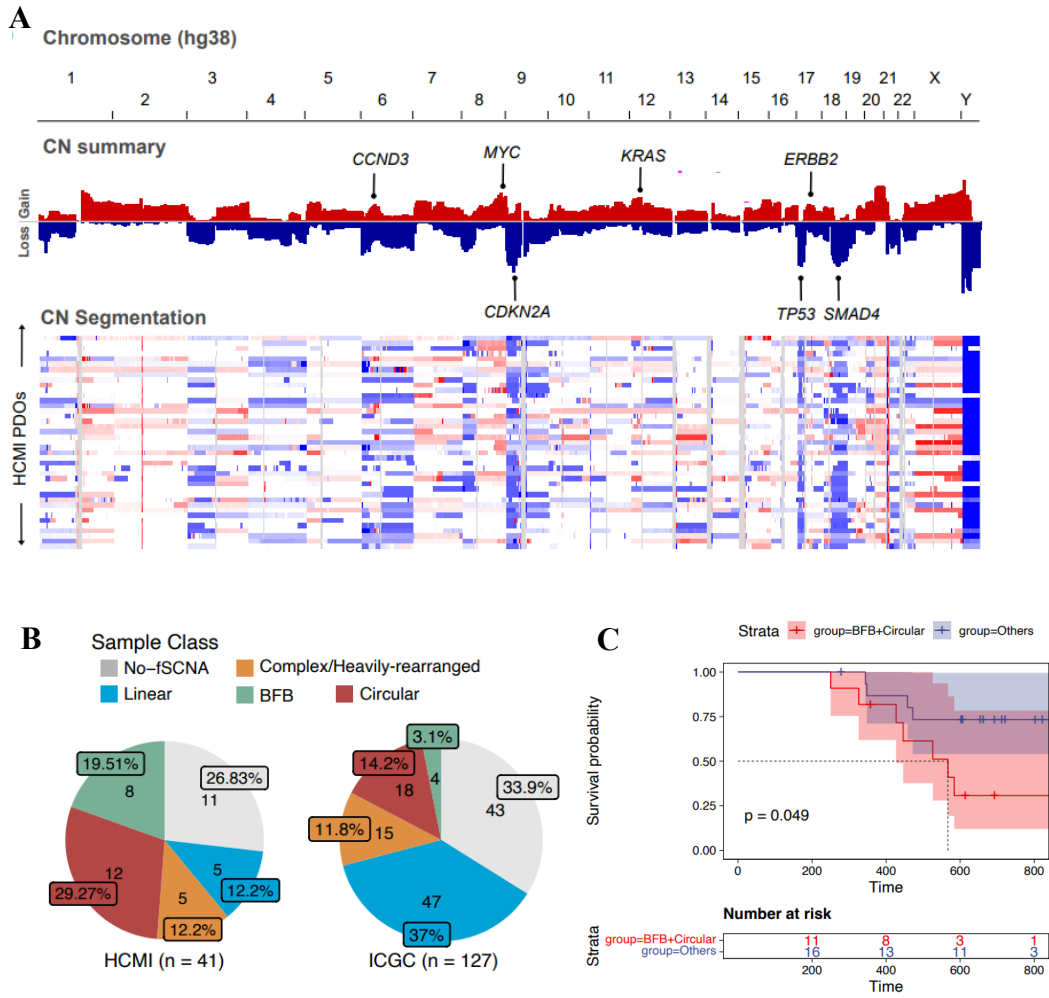
In PDAC, the emergence of copy number amplifications in oncogenes, such as *GATA6*, *KRAS* and *MYC* define the evolutionary trajectory of the tumour (Mueller *et al.*, 2018; Baslan *et al.*, 2022). Sustained *MYC* activity is required for maintenance and progression of PDAC (Hayashi *et al.*, 2020; Sodikin *et al.*, 2020; Maddipati *et al.*, 2022). Elevated *MYC* expression defines a subset of PDAC cells with high metastatic capability and amplifications of *MYC* are specifically enriched in metastatic PDAC (Hayashi *et al.*, 2020; Maddipati *et al.*, 2022).

Here, we provide the first detailed analysis of ecDNA in PDAC. We demonstrate that ecDNA is a major source of high-level amplifications in key PDAC oncogenes and a major contributor of *MYC* heterogeneity in PDAC. We observed different mechanisms of *MYC* amplification. PDOs and tissues harbouring *MYC* on ecDNA displayed significant heterogeneity of *MYC* copy number and higher *MYC*

expression compared with tumours having *MYC* on chromosomal DNA. Nonetheless, we found that the transcriptional output of an oncogene from ecDNA cannot be simply inferred from the ecDNA copy-number and *cis*-regulatory elements on the amplicon (e.g., *PVT1* promoter) need to be considered. The combined analysis of tissues and PDOs suggest that the generation of ecDNA is likely a late event in the history of pancreatic cancer. EcDNA were reported in tumours displaying genomic and transcriptomic features of advanced diseases. In line with previous reports (Takahashi *et al.*, 2022), ecDNA in PDOs correlated with the levels of γ H2AX, a well-established marker of DNA damage and mitotic checkpoint activation (Turinetto and Giachino, 2015). In agreement with that, the accumulation of ecDNAs, but not oncogene levels *per se*, was associated with abundant γ H2AX foci, reduced proliferative index, and increased apoptotic cell death. Our result suggests that the large number of ecDNA might not be tolerated unless providing enhanced fitness in specific microenvironmental conditions. Accordingly, the removal of the selection pressure was associated with the rapid reduction of ecDNA elements and of the levels of γ H2AX. Similarly, the extensive cultivation of PDOs in the absence of a selection pressure led to either the incorporation of ecDNA into HSR or the irreversible loss of ecDNA.

Mimicking the depletion of stromal niche factors (Boj *et al.*, 2015; Seino *et al.*, 2018), we show that ecDNAs represent important genomic adaptations that endow tumour cells with the ability to rapidly elevate oncogene expression in response to microenvironmental stressors. Our data further suggest that elevated *MYC* activity is fundamental to the acquisition of stromal independence in pancreatic cancer. While showing that ecDNA is a major source of *MYC* expression heterogeneity in PDAC, we did not conclusively demonstrate the impact of elevated *MYC* levels on neoplastic cell states. Elevation of *MYC* expression due to ecDNA affected PDOs morphology, created cancer cell addiction to transcriptional *MYC* output, but did not induce a molecular class switch. Additional cell intrinsic or cell extrinsic factors might be crucial to the definition of neoplastic cell states. Therefore, further studies will need to address the interaction between ecDNA and cell extrinsic inputs.

4.5. Supplementary Data



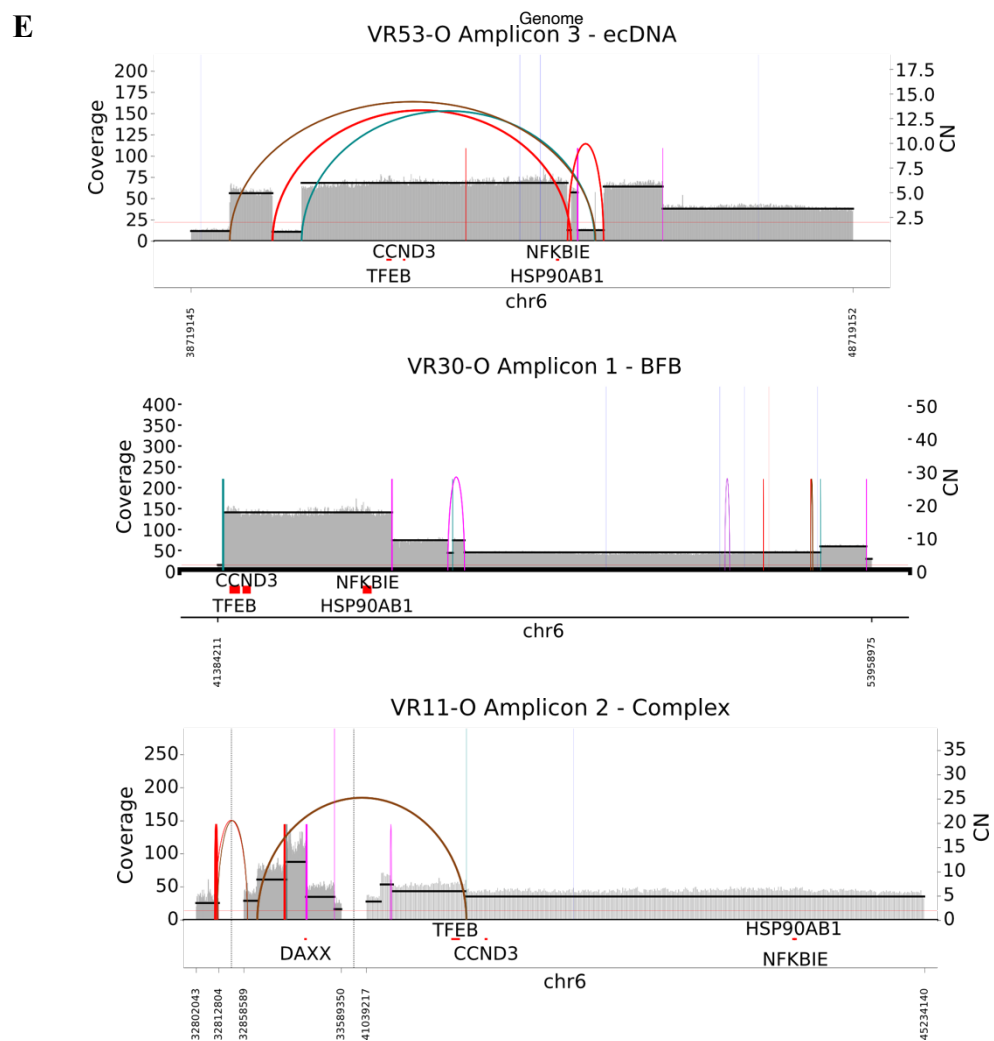
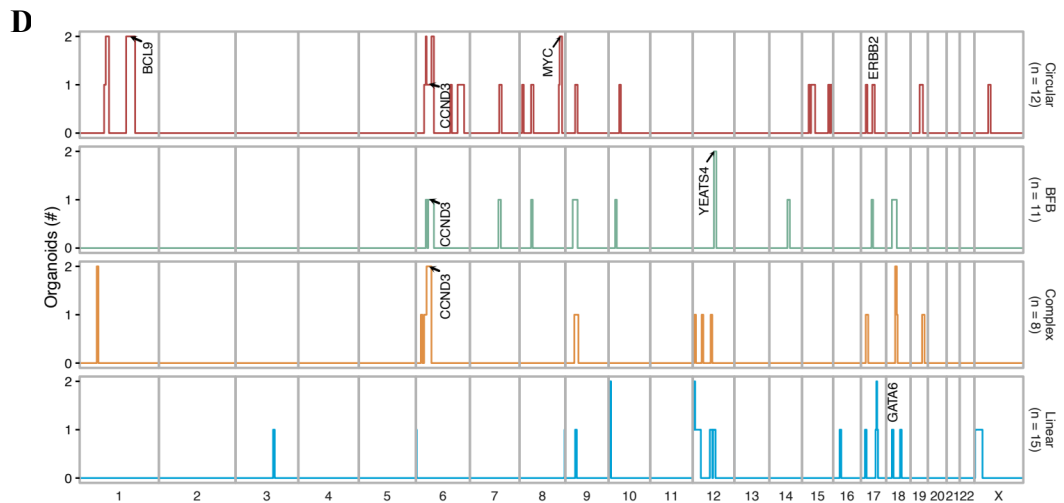
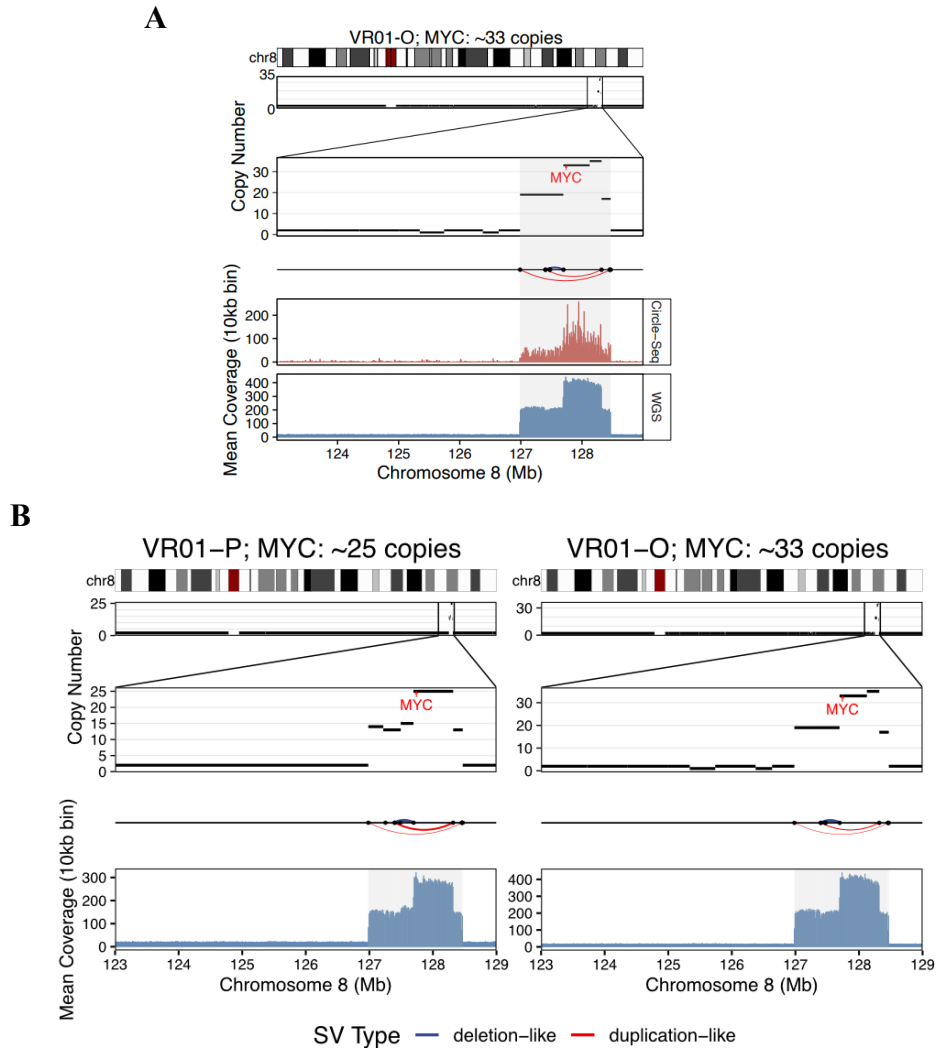


Figure S1. Frequency of ecDNA based amplifications in PDAC. A. Copy number (CN) analysis showing in the top panel, CN frequency plot displaying the frequency of copy number gains (0.1) and losses (-0.1) observed across the genome (segmentation mean) for the HCMI PDOs. Representative genes are shown on the plot at their genomic location; bottom panel, CN calls for

individual samples. Red represents CN gain and blue represents CN loss. **B.** Pie charts showing proportion of primary tumours (ICGC) and PDOs (HCMI) falling in each sample class based on their existing amplicon types. If a sample contained multiple amplicons, it was classified based on the following order: Circular > BFB > Complex > Linear. If no amplicons were detected, the sample was classified as no-focal somatic copy number amplification detected (No-fSCNA). **C.** Kaplan Meier survival plot comparing the overall survival of patients from the HCMI cohort (n = 27) according to AA-base amplicon classification. Survival curves are compared using the log-rank test. **D.** Genome-wide distribution of amplicons in PDOs. Amplicon regions were counted in a 5 Mbp bin and are shown respective to the occurrence in individual organoids. Recurring or PDAC driver genes are highlighted. **E.** Structural variant (SV) view of AA reconstructed amplicon structures containing the *CCND3* locus for three PDOs with different amplicon classifications. SV view shows coverage depth, copy number segments and discordant genomic connections (curves spanning copy number segments).



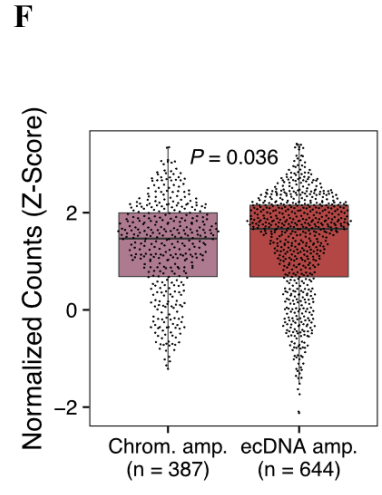
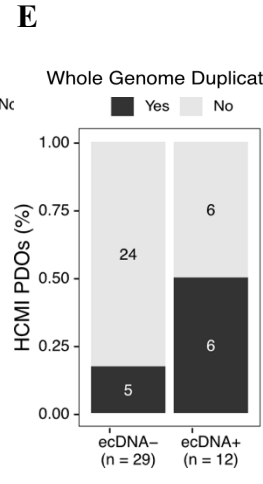
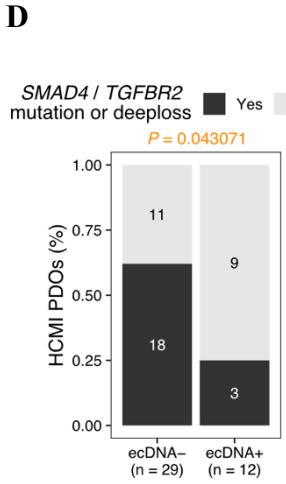
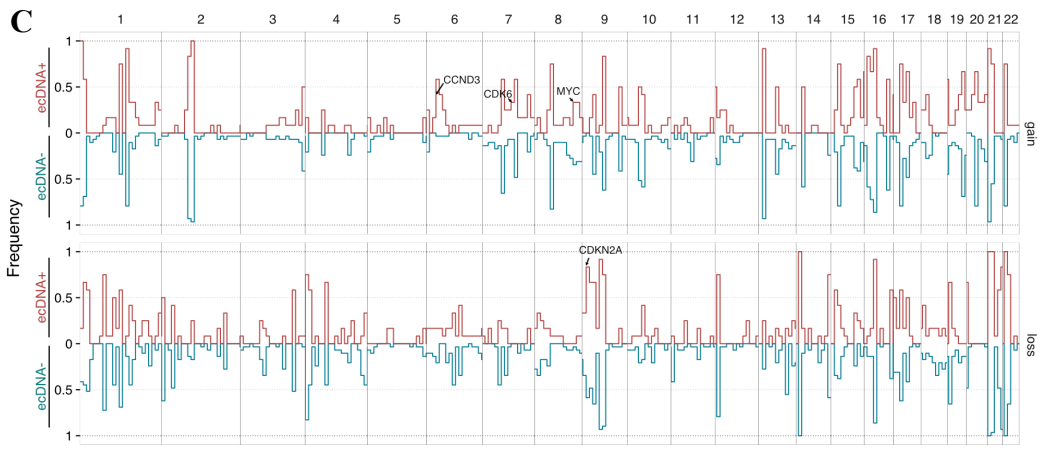
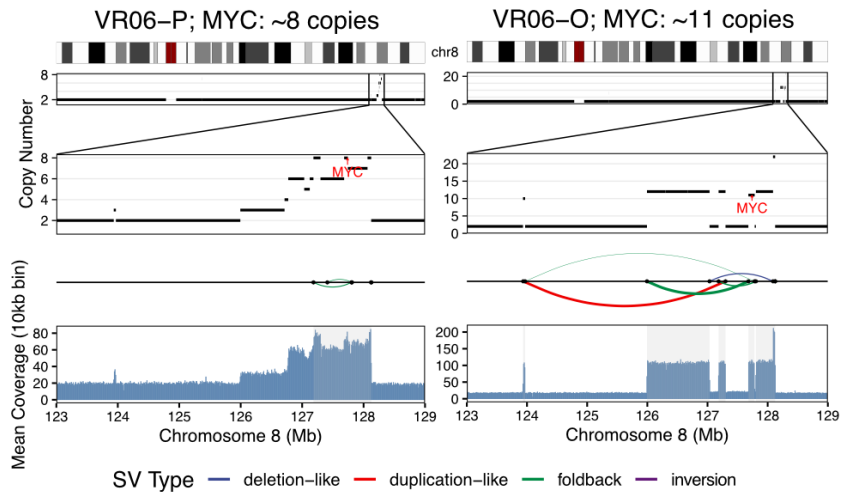


Figure S2. Extrachromosomal *MYC* amplifications are conserved between tissues and paired models.

A. Validation of the presence of *MYC* on ecDNA by Circle-Seq for VR01-O. The amplified ecDNA segments are highlighted in grey. Mean sequencing coverage was calculated for 10 kb bins.

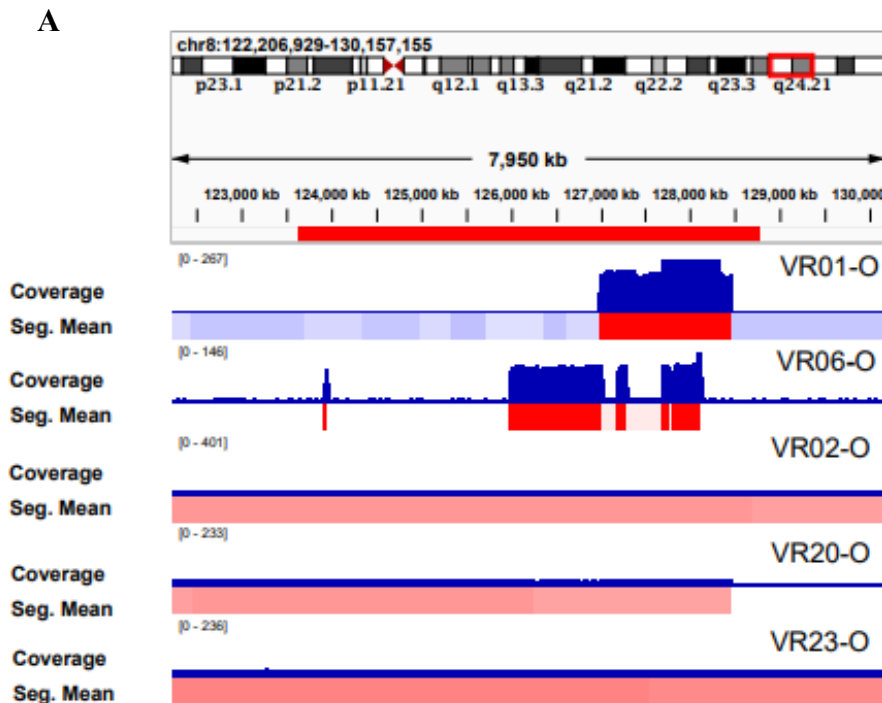
B. Copy number alterations on chromosome 8 with a focus on the *MYC* region of primary tissues (P) and matched organoids (O) for VR01 (left) and VR06 (right). SVs that connect amplified regions and form ecDNAs are displayed below copy number levels. WGS Coverage is depicted at the bottom.

C. Genomic overview of copy number alterations. Gain and loss frequency of ecDNA+ (n = 12) and ecDNA- (n = 29) organoids. *CDKN2A* was found to be lost in 10/12 ecDNA+ organoids in comparison to 14/29 ecDNA- organoids (Fisher p-value = 0.0026). *CCND3* gain was more common in ecDNA+ organoids (5/12) than ecDNA- organoids (1/29) (Fisher p-value = 0.0053) and *CDK6* gain was identified in 4/12 ecDNA+ and 2/29 ecDNA- organoids (Fisher p-value = 0.05). Binsize = 10Mbp; Loss: copy number ≤ 1 ; Gain: copy number ≥ 3 .

D. Bar plot showing enrichment for *SMAD4/TGFBR2* inactivating mutations or deep loss in ecDNA- HCMI PDOs. P values were calculated using a two-sided Fisher's exact test

E. Bar plot displaying enrichment of whole genome duplication in ecDNA+ ICGC primary tumour and ecDNA+ HCMI PDOs. P values were calculated using a two-sided Fisher's exact test. Significant association (p value < 0.05) is displayed in orange.

F. Boxplot showing normalised expression of genes (Z-scores) located on circular amplicons (ecDNA amp) or chromosomally amplified (chrom. amp). Statistical significance was evaluated using a Wilcoxon rank sum test.



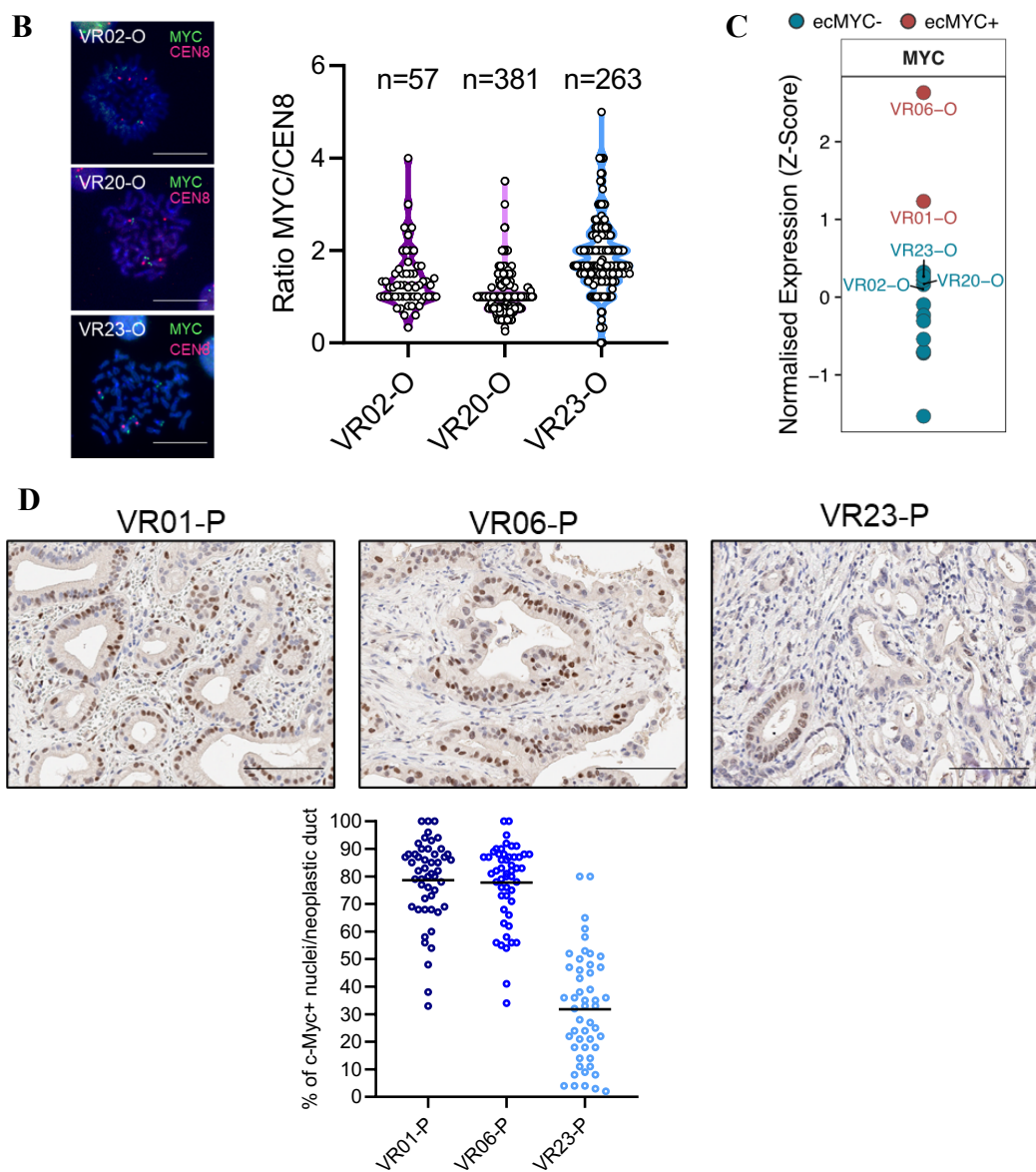


Figure S3. MYC copy number heterogeneity in PDAC. **A.** Coverage and segmentation mean histograms spanning the *MYC* locus for the samples indicated. **B.** Representative FISH images of ic*MYC* PDOs metaphases. Scale bar: 20 μ m (left). Scattered dot plot showing *MYC/CEN8* ratio for VR02-O, VR20-O, and VR23-O (right). **C.** *MYC* normalised expression values (Z-score) of ec*MYC* PDOs (red) and of *MYC* ecDNA- PDOs (blue). **D.** Representative immunohistochemistry for c-Myc in VR01, VR06, and VR23 patients' primary tumours. Scale bar: 100 μ m (left). Quantification is provided on the right as frequency of c-MYC+ nuclei per neoplastic duct, 50 neoplastic ducts were analysed for each case.

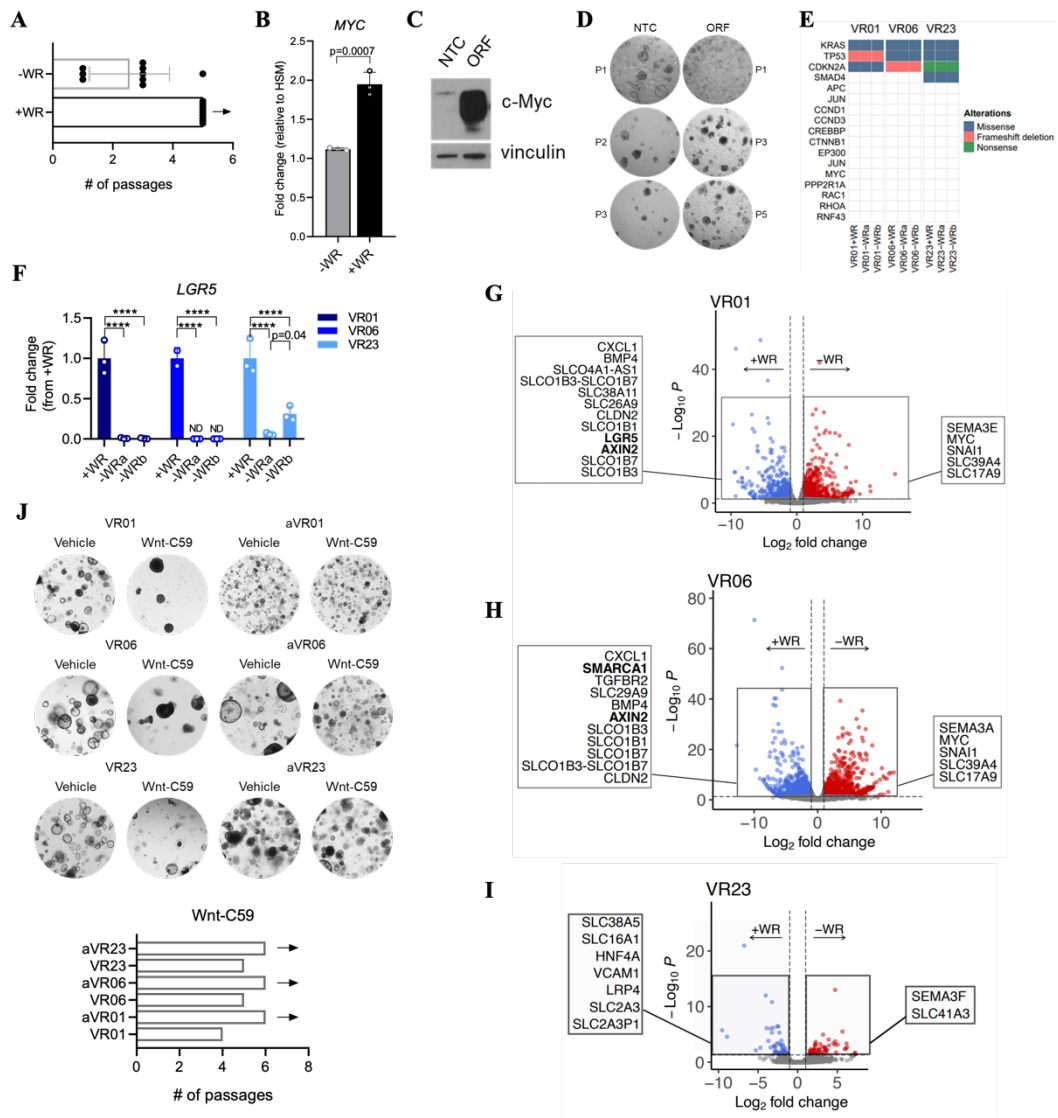
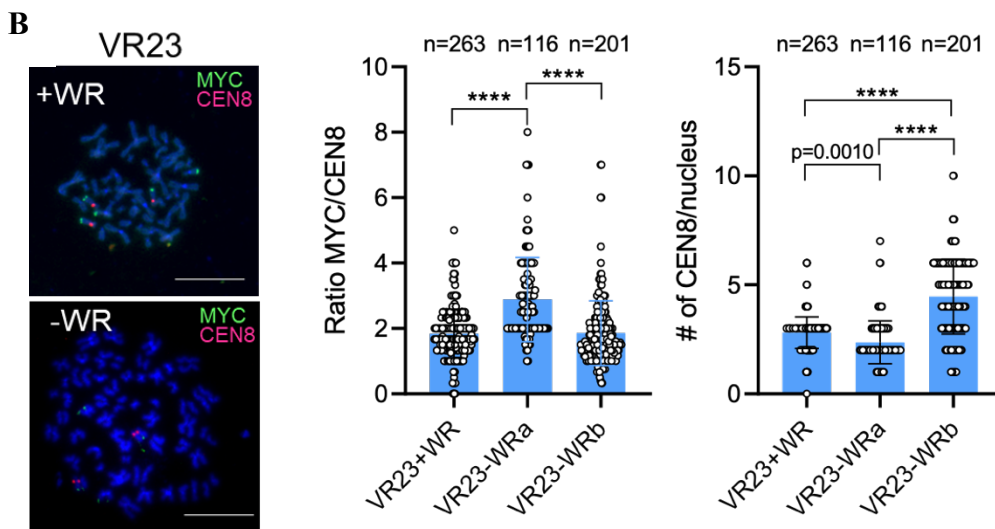
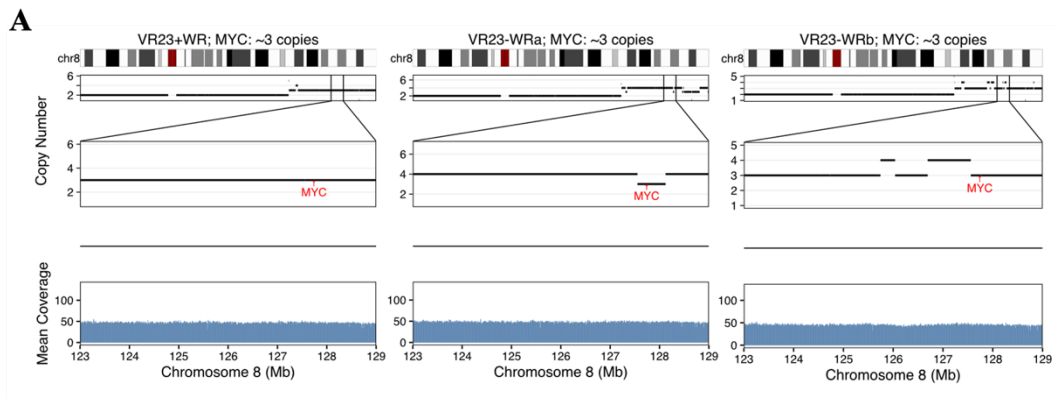


Figure S4. Elevated *MYC* activity enables PDO adaptation to Wnt agonists withdrawal. **A.** Bar plot showing number of passages at which organoid cultures ($n = 9$) passaged every week with a splitting ratio of 1:3 in -WR media reach extinction, compared to +WR media. **B.** Changes in relative expression levels of *MYC* of starved organoids (HSM) after culture in -WR and +WR media for eight hours. Results shown as mean \pm SD of three replicates. P value is reported in the figure as determined by Student's t-test. *GAPDH* was used as a housekeeping control gene to normalise results. **C.** Immunoblot analysis of c-Myc in whole cell lysate of VR01-O transfected with NTC (non-targeting control) and *MYC* ORF (open reading frame). Vinculin was used as loading control. **D.** Representative brightfield images of VR01-O transfected with NTC and *MYC* ORF passaged in -WR media with a splitting ratio of 1:3 every week, showing that VR01-ORF organoids could be propagated in -WR media without extinction of the culture. **E.** Oncoplot displaying absence of mutations in genes involved in Wnt pathway that could explain the acquisition of WR independence of -WR adapted organoids. **F.** Changes in the relative expression levels of *LGR5* in organoids

adapted to -WR media compared to baseline (+WR). Results shown as mean \pm SD of three replicates. ****, $p < 0.0001$ as determined by Two-way ANOVA. *HPRT1* was used as a control. ND, not determined. **G.** Volcano plot showing differentially expressed genes between VR01-O at baseline and after adaptation to grow in -WR media. Upregulated genes were showed as red dots ($\text{padj} < 0.05$ and $\log_2\text{foldchange} > 1$). Downregulated genes were showed as blue dots ($\text{padj} < 0.05$ and $\log_2\text{foldchange} < -1$). **H.** Volcano plot showing differentially expressed genes between VR06-O at baseline and after adaptation to grow in -WR media. Upregulated genes were showed as red dots ($\text{padj} < 0.05$ and $\log_2\text{foldchange} > 1$). Downregulated genes were showed as blue dots ($\text{padj} < 0.05$ and $\log_2\text{foldchange} < -1$). **I.** Volcano plot showing differentially expressed genes between VR23-O at baseline and after adaptation to grow in -WR media. Upregulated genes were showed as red dots ($\text{padj} < 0.05$ and $\log_2\text{foldchange} > 1$). Downregulated genes were showed as blue dots ($\text{padj} < 0.05$ and $\log_2\text{foldchange} < -1$). **J.** Representative brightfield images of baseline (+WR) and adapted organoids (-WR) cultured in the presence of Wnt-C59 (100 nM, PORCN inhibitor) or appropriate vehicle (left). Bar plot showing the number of passages at which each organoid could be propagated in the presence of Wnt-C59 (right).



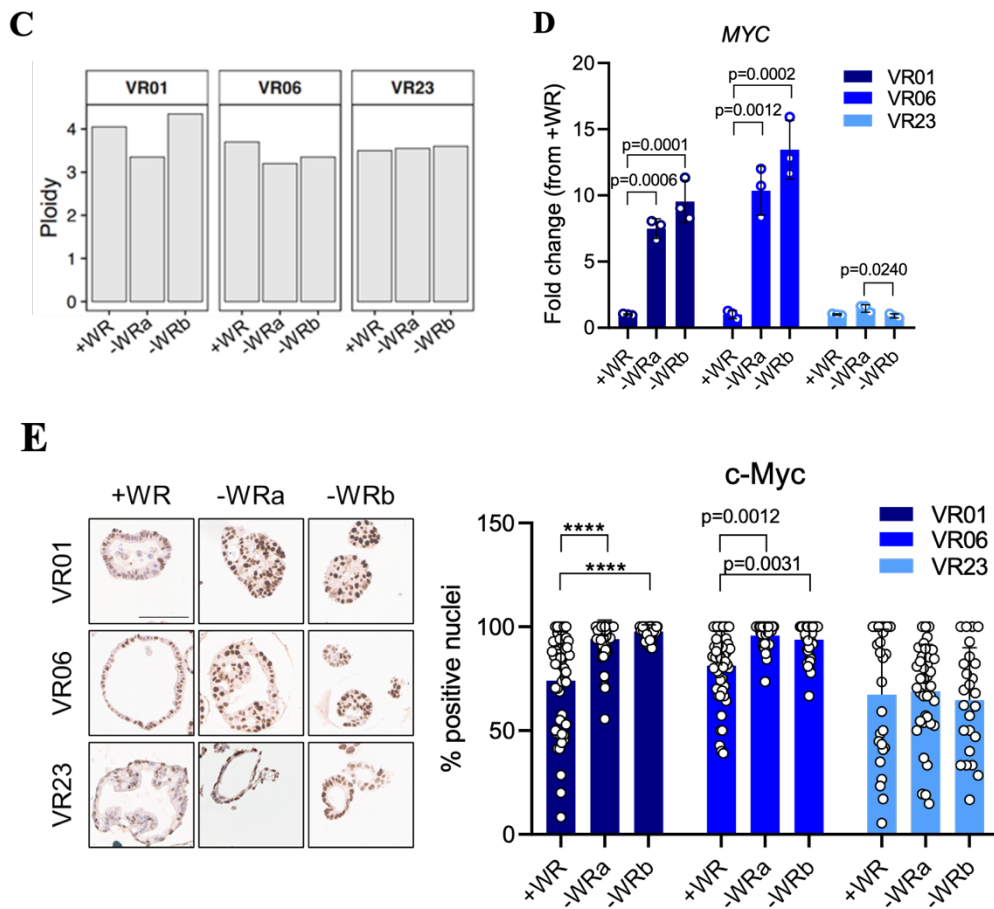


Figure S5. ecDNA supercharges *MYC* expression in adapted PDOs. **A.** Copy number alterations on chromosome 8 with a focus on *MYC* region, of ic*MYC* organoid VR23, at baseline (+WR) and adapted to depleted media (-WR). WGS Coverage is displayed below the copy number level. **B.** Representative FISH metaphases of VR23 at baseline (+WR) and after adaptation to depleted media (-WR). Scale bar: 20 μ m (left). Bar plot showing the ratio of *MYC* signal over *CEN8* and the number of *CEN8* in VR23 at baseline and after adaptation (-WR, 2 biological replicates) (right). P value by One-way ANOVA. ****, $p < 0.0001$. **C.** Ploidy analysis of organoids at baseline (+WR) and adapted to grow in depleted media (-WR). Ploidy was assessed from the WGS data using AMBER, COBALT, and PURPLE in tumour only mode (<https://github.com/hartwigmedical/hmftools>). **D.** Changes in the relative expression levels of *MYC* in organoids adapted to depleted media compared to baseline. Results shown as mean \pm SD of three replicates. P value determined by Two-way ANOVA. ****, $p < 0.0001$. *GAPDH* was used as housekeeping control gene to normalise results. **E.** Representative immunohistochemistry for c-Myc of formalin-fixed paraffin-embedded organoids at baseline and adapted to grow in -WR media. Scale bar: 100 μ m (left). Quantification is provided on the right as frequency of positive nuclei per organoid. A minimum of 25 organoids per sample were analysed. P values determined by Two-way ANOVA. ****, $p < 0.0001$.

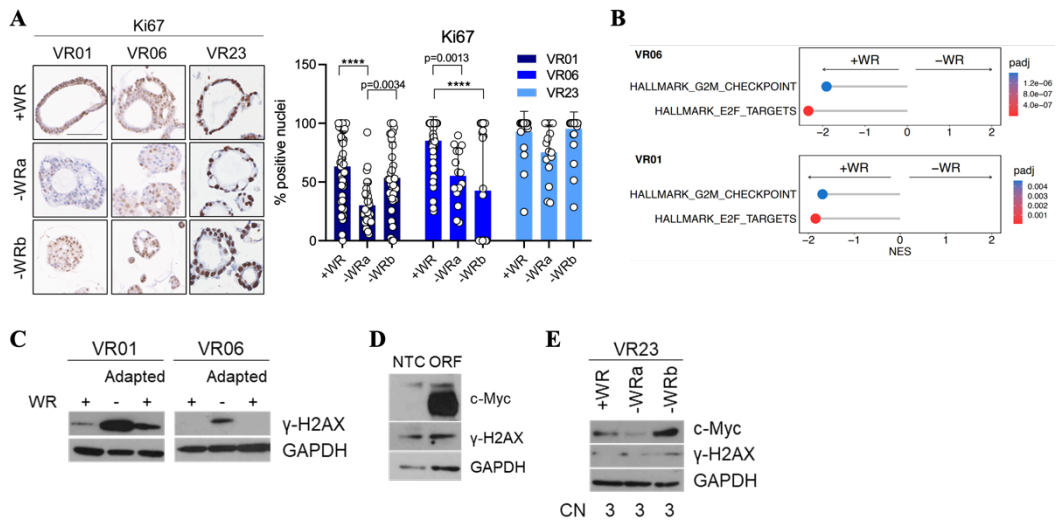
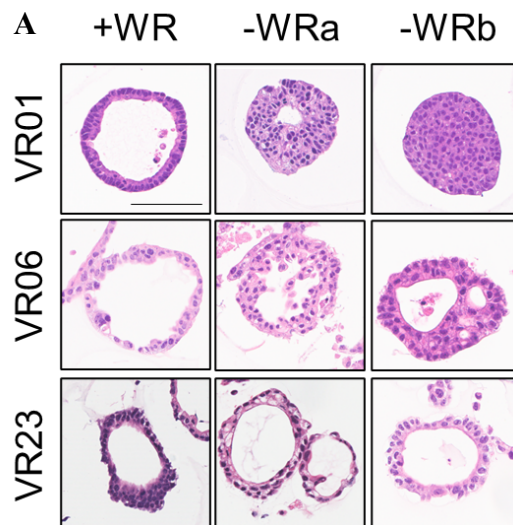


Figure S6. Accumulation of ecDNA leads to increased gH2AX foci **A.** Representative immunohistochemistry for Ki67 of parental (+WR) and adapted (-WR, two biological replicates) organoids. Scale bar: 100 μ m. Quantification for Ki67 is provided on the right as frequency of Ki67+ nuclei per organoid, at least 15 organoids were analysed for each condition. Significance was assessed by Two-way ANOVA. ****, $p < 0.0001$. **B.** Enrichment analysis of proliferation-related pathways of ecMYC organoids adapted (-WR, NES >0) and at baseline (+WR, NES <0). **C.** Immunoblot of ecMYC adapted organoids before and after removal of the imposed pressure. Baseline conditions are included for reference level of proteins expression. GAPDH was used as loading control. **D.** Immunoblot analysis for c-Myc and γ -H2AX in whole cell lysate of VR01-O transfected with NTC (non-targeting control) and MYC ORF (open reading frame). GAPDH was used as loading control. **E.** Immunoblot analysis of VR23 at baseline and after adaptation to -WR condition. GAPDH was used as loading control.



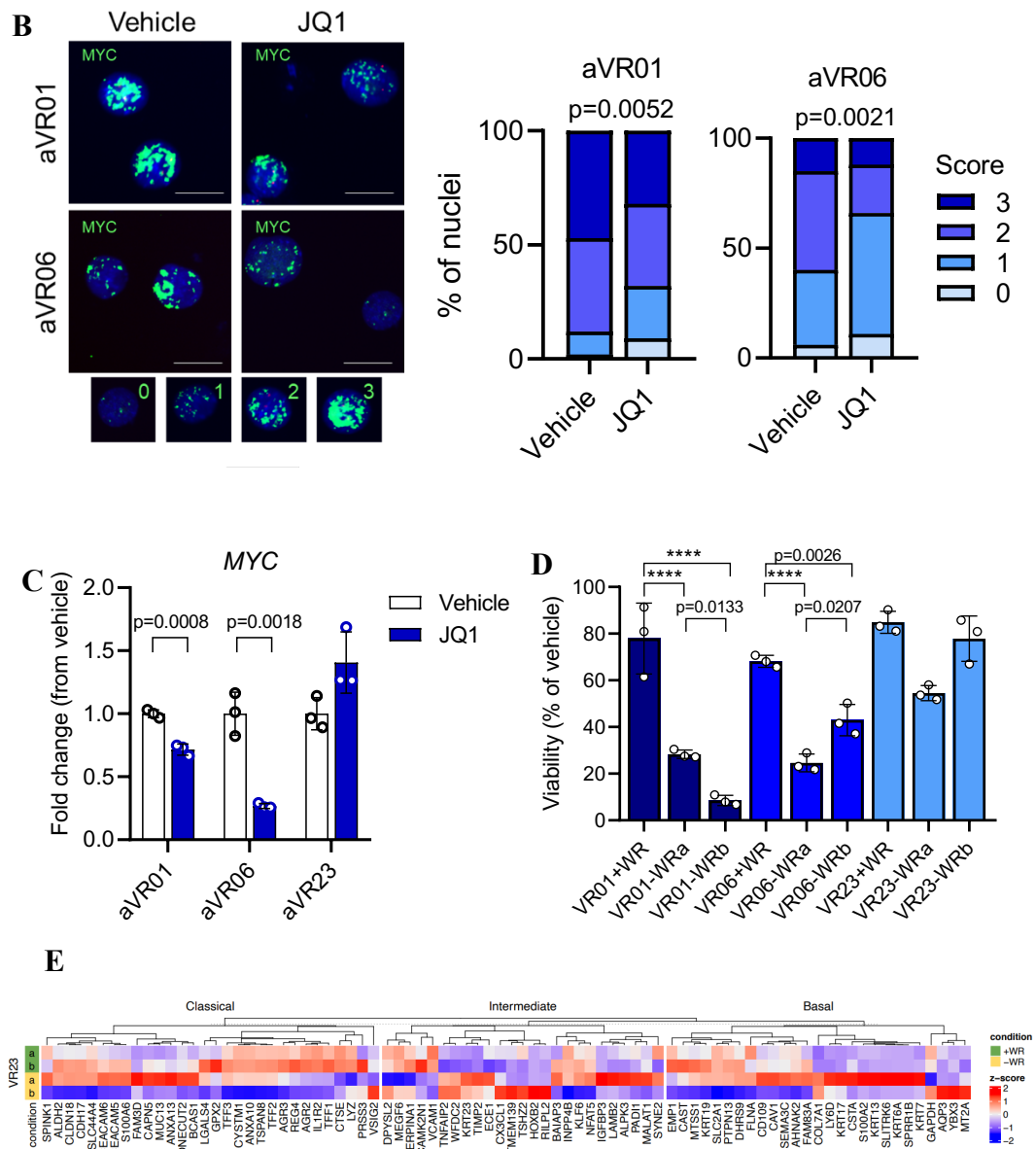


Figure S7. Accumulation of ecDNA is associated with morphological and phenotypic changes.

A. Representative haematoxylin and eosin (H&E) staining of formalin-fixed paraffin-embedded organoids at baseline and adapted to grow in -WR media. Scale bar: 100 μ m. **B.** Representative FISH interphase nuclei of adapted organoids treated with JQ1 (500nM) or appropriate vehicle control for 72 hours showing reduction of *MYC* hubs upon treatment. Scale bar: 20 μ m. Representative FISH interphase nuclei for the four different scores (0 to 3) used for the quantification are provided on the bottom. Quantification is provided on the right as frequency of nuclei with different hubs score. Significance was assessed by Chi-square. **C.** Changes in the relative expression levels of *MYC* in adapted organoids treated with JQ1 (500nM) for 72 hours. P value determined by Two-way ANOVA. Results shown as mean \pm SD of three replicates. *GAPDH* was used as housekeeping control gene to normalise results. **D.** Bar plot showing cell viability of baseline (+WR) and adapted (-WR) organoids upon 72 hours of JQ1 treatment (500nM). P value determined by Two-

way ANOVA. ****, $p < 0.0001$. **E.** Heatmap displaying the expression of Classical, Intermediate, and Basal genes from Raghavan et al. (Raghavan et al., 2021) in baseline (two biological replicas) and adapted (two biological replicas) VR23 organoids.

Table S1. Clinical data for PDOs

HCM ID	ID	Age	Sex	AJCC pathologic stage	Treatment Status	Vital status	Cause of death	Days to last follow up/days to death	Tissue Source	Histology
HCM-CSHL-0074-C25	VR17-O	54	male	Stage III	no	Alive	N/A	802	Primary tumour	PDAC
HCM-CSHL-0189-C25	VR51-O	64	male	Stage III	no	Dead	Surgical Complications	4	Primary tumour	PDAC
HCM-CSHL-0191-C25	VR46-O	75	male	Stage II	no	Dead	Cancer Related	472	Primary tumour	Adenosquamous carcinoma
HCM-CSHL-0193-C25	VR52-O	46	female	Stage IIB	no	Alive	N/A	606	Primary tumour	PDAC
HCM-CSHL-0073-C25	VR14-O	55	male	Stage III	no	Unknown	N/A	856	Primary tumour	PDAC
HCM-CSHL-0187-C25	VR29-O	67	male	Stage IIB	no	Alive	N/A	654	Primary tumour	PDAC
HCM-CSHL-0371-C25	VR44-O	74	female	Stage IIB	no	Dead	Cancer Related	344	Primary tumour	PDAC
HCM-CSHL-0088-C25	VR34-O	75	male	Stage III	no	Alive	N/A	712	Primary tumour	PDAC
HCM-CSHL-0181-C25	VR33-O	60	female	Stage III	no	Alive	N/A	721	Primary tumour	PDAC
HCM-CSHL-0092-C25	VR20-O	69	male	Stage III	no	Alive	N/A	358	Primary tumour	PDAC
HCM-CSHL-0089-C25	VR23-LNO	62	male	Stage III	no	Dead	Cancer Related	N/A	Lymph Node Metastasis	PDAC
HCM-CSHL-0089-C25	VR23-O	62	male	Stage III	no	Dead	Cancer Related	N/A	Primary tumour	PDAC
HCM-CSHL-0081-C25	VR09-O	57	male	Stage III	no	Dead	Cancer Related	250	Primary tumour	PDAC Signet ring
HCM-CSHL-0192-C25	VR32-O	67	male	Stage IIB	no	Alive	N/A	614	Primary tumour	PDAC
HCM-CSHL-0177-C25	VR48-O	64	female	Stage III	no	Unknown	N/A	N/A	Primary tumour	PDAC
HCM-CSHL-0078-C25	VR11-O	72	male	Stage III	no	Dead	Cancer Related	526	Primary tumour	Pancreatic carcinoma from IPMN
HCM-CSHL-0078-C25	VR11-LNO	72	male	Stage III	no	Dead	Cancer Related	526	Lymph Node Metastasis	Pancreatic carcinoma from IPMN
HCM-CSHL-0076-C25	VR25-O	74	female	Stage III	no	Dead	Cancer Related	458	Primary tumour	PDAC
HCM-CSHL-0182-C25	VR30-O	74	male	Stage IIB	no	Unknown	N/A	N/A	Primary tumour	PDAC
HCM-CSHL-0183-C25	VR38-O	63	female	Stage III	no	Unknown	N/A	N/A	Primary tumour	PDAC
HCM-CSHL-0180-C25	VR37-O	64	female	Stage IIB	no	Alive	N/A	693	Primary tumour	PDAC
HCM-CSHL-0084-C25	VR06-O	73	female	Stage III	no	Unknown	N/A	N/A	Primary tumour	PDAC
HCM-CSHL-0374-C25	VR53-O	74	male	Stage III	no	Dead	Surgical Complications	13	Primary tumour	PDAC
HCM-CSHL-0077-C25	VR02-O	66	male	Stage III	no	Alive	N/A	865	Primary tumour	PDAC
HCM-CSHL-0178-C25	VR35-O	71	male	Stage III	no	Dead	Cancer Related	326	Primary tumour	PDAC
HCM-CSHL-0090-C25	VR21-O	64	female	Stage III	no	Dead	Cancer Related	N/A	Primary tumour	Adenosquamous carcinoma
HCM-CSHL-0186-C25	VR43-O	74	male	Stage IIB	no	Unknown	N/A	N/A	Primary tumour	PDAC
HCM-CSHL-0179-C25	VR47-O	60	female	Stage III	no	Dead	Cancer Related	348	Primary tumour	PDAC
HCM-CSHL-0094-C25	VR31-O	61	female	Stage III	no	Alive	N/A	278	Primary tumour	PDAC
HCM-CSHL-0372-C25	VR45-O	70	female	Stage IIB	no	Alive	N/A	662	Primary tumour	PDAC
HCM-CSHL-0093-C25	VR12-O	71	female	Stage III	no	Alive	N/A	602	Primary tumour	PDAC
HCM-CSHL-0176-C25	VR10-O	59	female	Stage III	no	Dead	Cancer Related	427	Primary tumour	PDAC
HCM-CSHL-0079-C25	VR15-O	75	male	Stage III	no	Alive	N/A	822	Primary tumour	PDAC
HCM-CSHL-0075-C25	VR24-O	74	female	Stage IIB	no	Dead	Infection	549	Primary tumour	PDAC
HCM-CSHL-0184-C25	VR41-O	77	female	Stage III	no	Dead	Cancer Related	446	Primary tumour	PDAC
HCM-CSHL-0373-C25	VR50-O	71	female	Stage IA	no	Alive	N/A	605	Primary tumour	PDAC poorly differentiated
HCM-CSHL-0080-C25	VR03-O	60	female	Stage III	no	Unknown	N/A	N/A	Primary tumour	PDAC
HCM-CSHL-0091-C25	VR27-O	63	female	Stage IIB	no	Alive	N/A	692	Primary tumour	PDAC
HCM-CSHL-0082-C25	VR13-O	77	male	Stage III	no	Alive	N/A	856	Primary tumour	PDAC
HCM-CSHL-0601-C25	VR40-LNO	61	female	Stage III	yes	Dead	N/A	584	Lymph Node Metastasis	PDAC
HCM-CSHL-0600-C25	VR19-LNO	72	male	Stage III	no	Dead	N/A	567	Lymph Node Metastasis	PDAC

Table S2. Genes covered in panel sequencing for all coding exons.

<i>AKT1</i>	<i>BRCA2</i>	<i>EP300</i>	<i>HIST1H3B</i>	<i>MAP2K4</i>	<i>NOTCH3</i>	<i>RAC1</i>	<i>STAG2</i>
<i>AKT2</i>	<i>CBL</i>	<i>EPHA3</i>	<i>HIST1H3C</i>	<i>MAP3K1</i>	<i>NOTCH4</i>	<i>RAD21</i>	<i>STAT3</i>
<i>AKT3</i>	<i>CCND1</i>	<i>ERBB2</i>	<i>HIST2H3C</i>	<i>MAPK1</i>	<i>NPM1</i>	<i>RAD50</i>	<i>STAT5B</i>
<i>ALK</i>	<i>CCND3</i>	<i>ERBB3</i>	<i>HLA-A</i>	<i>MAX</i>	<i>NRAS</i>	<i>RAF1</i>	<i>STK11</i>
<i>AMER1</i>	<i>CD274</i>	<i>ERBB4</i>	<i>HLA-B</i>	<i>MED12</i>	<i>NTRK1</i>	<i>RBI</i>	<i>SYK</i>
<i>APC</i>	<i>CD58</i>	<i>ERG</i>	<i>HLA-C</i>	<i>MEN1</i>	<i>PALB2</i>	<i>RET</i>	<i>TGFBR2</i>
<i>APLN</i>	<i>CDK12</i>	<i>ESR1</i>	<i>HNF1A</i>	<i>MET</i>	<i>PBRM1</i>	<i>RHOA</i>	<i>TP53</i>
<i>AR</i>	<i>CDK4</i>	<i>ETV6</i>	<i>HRAS</i>	<i>MLH1</i>	<i>PDCD1LG2</i>	<i>RNF43</i>	<i>TSC1</i>
<i>ARAF</i>	<i>CDKN1A</i>	<i>EZH2</i>	<i>IDH1</i>	<i>MSH2</i>	<i>PDGFRA</i>	<i>ROS1</i>	<i>TSC2</i>
<i>ARID1A</i>	<i>CDKN1B</i>	<i>FAS</i>	<i>IDH2</i>	<i>MSH6</i>	<i>PDGFRB</i>	<i>RPL5</i>	<i>U2AF1</i>
<i>ARID1B</i>	<i>CDKN2A</i>	<i>FBXW7</i>	<i>JAK1</i>	<i>MTOR</i>	<i>PHF6</i>	<i>RUNX1</i>	<i>VHL</i>
<i>ARID2</i>	<i>CDKN2B</i>	<i>FGFR1</i>	<i>JAK2</i>	<i>MUTYH</i>	<i>PIK3CA</i>	<i>SETBP1</i>	<i>WT1</i>
<i>ASXL1</i>	<i>CHEK2</i>	<i>FGFR2</i>	<i>JAK3</i>	<i>MYB</i>	<i>PIK3CB</i>	<i>SETD2</i>	
<i>ATM</i>	<i>CIITA</i>	<i>FGFR3</i>	<i>JUN</i>	<i>MYC</i>	<i>PIK3R1</i>	<i>SF3B1</i>	
<i>ATR</i>	<i>CREBBP</i>	<i>FGFR4</i>	<i>KDR</i>	<i>MYCN</i>	<i>PMS2</i>	<i>SMAD4</i>	
<i>ATRX</i>	<i>CTCF</i>	<i>GATA3</i>	<i>KIT</i>	<i>NBN</i>	<i>POLE</i>	<i>SMARCA4</i>	
<i>B2M</i>	<i>CTNNB1</i>	<i>GNAI1</i>	<i>KLF4</i>	<i>NF1</i>	<i>POLQ</i>	<i>SMARCB1</i>	
<i>BAP1</i>	<i>DAXX</i>	<i>GNAQ</i>	<i>KMT2A</i>	<i>NF2</i>	<i>PPP2R1A</i>	<i>SMO</i>	
<i>BLM</i>	<i>DICER1</i>	<i>GNAS</i>	<i>KRAS</i>	<i>NFE2L2</i>	<i>PTCH1</i>	<i>SOCS1</i>	
<i>BRAF</i>	<i>DNMT3A</i>	<i>H3F3A</i>	<i>MAP2K1</i>	<i>NOTCH1</i>	<i>PTEN</i>	<i>SPOP</i>	
<i>BRCA1</i>	<i>EGFR</i>	<i>H3F3B</i>	<i>MAP2K2</i>	<i>NOTCH2</i>	<i>PTPN11</i>	<i>STAG1</i>	

5. Concluding remarks

PDAC has the lowest 5-year survival rate out of all cancers, and despite extensive research into the disease, there have been very few recent breakthroughs that have increased patients' outcomes (Hosein *et al.*, 2022; Siegel *et al.*, 2023). In part, this is due to the inter- and intra-patient heterogeneity, which is not faithfully recapitulated by animal models and conventional 2D *in vitro* cultures. Additionally, studying PDAC cancer cells in patients has been hindered by the stroma-rich microenvironment and low neoplastic cellularity, which are hallmarks of the disease. To overcome these limitations, we used PDOs, a 3D *in vitro* models, which have been shown to recapitulate the molecular features of their nascent tissues and the intratumor heterogeneity, found in patients.

We first aimed to establish a library of PDOs, with a particular focus on establishing models from pre-treated patients due to the increase of using chemotherapies in a neo-adjuvant setting. We found higher transcriptional heterogeneity in PDOs from tumour-treated samples, as well as enrichment for inactivating mutations in *RNF43* and gains of cyclin-encoding genes. Further experiments on matched models are required to understand if these events are induced or their initial presence dictates therapy resistance.

We then focused on the WR dependency established previously as a surrogate for stromal independence (Seino *et al.*, 2018). In our cohort, RSPO, rather than WNT was the limiting factor, in contrast with previous reports. We found that RSPO was produced by endothelial cells and supports cancer cells *in vitro*. Further functional and co-culturing experiments are required to understand whether RSPO acts via the canonical WNT pathways or whether it acts through different molecular mechanisms. Endothelial cells appear to not just play a role in vessel formation, but also as providing essential cytokines to cancer cells. Finally, as CAFs and immune cells have been previously subtyped, it is entirely possible that different types of endothelial cells with various roles might exist within the TME.

Finally, we explored whether PDOs can survive without WNT and RSPO, and we found that resistance to their removal was mediated by *ecMYC* enrichment. We modelled the dynamics of nascent *ecMYCs* in PDOs and found how they can mediate cancer cells' survival and disease progression. Further studies are required

to understand if other genes, important for therapy resistance, can also play a role in PDAC, opening avenues for new therapeutic targets.

6. References

- Abraham, S.C. *et al.* (2001) ‘Distinctive molecular genetic alterations in sporadic and familial adenomatous polyposis-associated pancreatoblastomas: frequent alterations in the APC/beta-catenin pathway and chromosome 11p’, *The American journal of pathology*, 159(5), pp. 1619–1627. Available at: [https://doi.org/10.1016/S0002-9440\(10\)63008-8](https://doi.org/10.1016/S0002-9440(10)63008-8).
- Abraham, S.C. *et al.* (2002) ‘Genetic and Immunohistochemical Analysis of Pancreatic Acinar Cell Carcinoma : Frequent Allelic Loss on Chromosome 11p and Alterations in the APC/ β -Catenin Pathway’, *The American Journal of Pathology*, 160(3), p. 953. Available at: [https://doi.org/10.1016/S0002-9440\(10\)64917-6](https://doi.org/10.1016/S0002-9440(10)64917-6).
- A-Kader, H.H. and Ghishan, F.K. (2012) ‘The Pancreas’, *Textbook of Clinical Pediatrics*, p. 1925. Available at: https://doi.org/10.1007/978-3-642-02202-9_198.
- Akalin, A. *et al.* (2015) ‘Genomation: a toolkit to summarize, annotate and visualize genomic intervals’, *Bioinformatics*. 2014/11/25, 31(7), pp. 1127–1129. Available at: <https://doi.org/10.1093/bioinformatics/btu775>.
- Alexandrov, L.B. *et al.* (2013) ‘Signatures of mutational processes in human cancer’, *Nature* 2013 500:7463, 500(7463), pp. 415–421. Available at: <https://doi.org/10.1038/nature12477>.
- Aran, D. *et al.* (2019) ‘Reference-based analysis of lung single-cell sequencing reveals a transitional profibrotic macrophage’, *Nature Immunology* 2019 20:2, 20(2), pp. 163–172. Available at: <https://doi.org/10.1038/s41590-018-0276-y>.
- Arina, A. *et al.* (2016) ‘Tumor-associated fibroblasts predominantly come from local and not circulating precursors’, *Proceedings of the National Academy of Sciences of the United States of America*, 113(27), pp. 7551–7556. Available at: https://doi.org/10.1073/PNAS.1600363113/SUPPL_FILE/PNAS.1600363113.SM02.MOV.
- Bailey, J. *et al.* (2016) ‘p53 mutations cooperate with oncogenic Kras to promote adenocarcinoma from pancreatic ductal cells’, *Oncogene*, 35(32), pp. 4282–4288. Available at: <https://doi.org/10.1038/onc.2015.441>.
- Bailey, Peter *et al.* (2016) ‘Genomic analyses identify molecular subtypes of pancreatic cancer’, *Nature*, 531(7592), pp. 47–52. Available at: <https://doi.org/10.1038/nature16965>.

- Bailey, P *et al.* (2016) ‘Genomic analyses identify molecular subtypes of pancreatic cancer’, *Nature*. 2016/02/26, 531(7592), pp. 47–52. Available at: <https://doi.org/10.1038/nature16965>.
- Baker, L.A. *et al.* (2016) ‘Modeling pancreatic cancer with organoids’, *Trends in cancer*, 2(4), p. 176. Available at: <https://doi.org/10.1016/J.TRECAN.2016.03.004>.
- Baslan, T. *et al.* (2022) ‘Ordered and deterministic cancer genome evolution after p53 loss’, *Nature*. 2022/08/18, 608(7924), pp. 795–802. Available at: <https://doi.org/10.1038/s41586-022-05082-5>.
- Basturk, O. *et al.* (2015) ‘A revised classification system and recommendations from the Baltimore consensus meeting for neoplastic precursor lesions in the pancreas’, in *American Journal of Surgical Pathology*. Lippincott Williams and Wilkins, pp. 1730–1741. Available at: <https://doi.org/10.1097/PAS.0000000000000533>.
- Bekkali, N.L.H. and Oppong, K.W. (2017) ‘Pancreatic ductal adenocarcinoma epidemiology and risk assessment: Could we prevent? Possibility for an early diagnosis’, *Endoscopic Ultrasound*, 6(Suppl 3), p. S58. Available at: https://doi.org/10.4103/EUS.EUS_60_17.
- Beroukhim, R. *et al.* (2010) ‘The landscape of somatic copy-number alteration across human cancers’, *Nature*. 2010/02/19, 463(7283), pp. 899–905. Available at: <https://doi.org/10.1038/nature08822>.
- Bhattacharjee, S. *et al.* (2021) ‘Tumor restriction by type I collagen opposes tumor-promoting effects of cancer-associated fibroblasts’, *The Journal of Clinical Investigation*, 131(11), p. 33905375. Available at: <https://doi.org/10.1172/JCI146987>.
- Biankin, A. V. *et al.* (2012) ‘Pancreatic cancer genomes reveal aberrations in axon guidance pathway genes’, *Nature*, 491(7424), pp. 399–405. Available at: <https://doi.org/10.1038/nature11547>.
- Bielski, C.M. *et al.* (2018) ‘Widespread Selection for Oncogenic Mutant Allele Imbalance in Cancer’, *Cancer Cell*, 34(5), pp. 852-862.e4. Available at: <https://doi.org/10.1016/j.ccell.2018.10.003>.

Biffi, G. *et al.* (2019) 'Il1-induced Jak/STAT signaling is antagonized by TGF β to shape CAF heterogeneity in pancreatic ductal adenocarcinoma', *Cancer Discovery*, 9(2), pp. 282–301. Available at: <https://doi.org/10.1158/2159-8290.CD-18-0710>.

Boj, Sylvia F., Hwang, C. Il, Baker, L.A., Chio, I.I.C., Engle, D.D., Corbo, V., Jager, M., Ponz-Sarvisé, M., Tiriác, H., Spector, Mona S, *et al.* (2015) 'Organoid models of human and mouse ductal pancreatic cancer', *Cell*, 160(1–2), pp. 324–338. Available at: <https://doi.org/10.1016/J.CELL.2014.12.021>.

Boj, Sylvia F., Hwang, C. Il, Baker, L.A., Chio, I.I.C., Engle, D.D., Corbo, V., Jager, M., Ponz-Sarvisé, M., Tiriác, H., Spector, Mona S., *et al.* (2015) 'Organoid Models of Human and Mouse Ductal Pancreatic Cancer', *Cell*, 160(1–2), pp. 324–338. Available at: <https://doi.org/10.1016/J.CELL.2014.12.021>.

Boj, S F *et al.* (2015) 'Organoid models of human and mouse ductal pancreatic cancer', *Cell*. 2015/01/06, 160(1–2), pp. 324–338. Available at: <https://doi.org/10.1016/j.cell.2014.12.021>.

Bourne, H.R., Sanders, D.A. and McCormick, F. (1990) 'The GTPase superfamily: A conserved switch for diverse cell functions', *Nature*, 348(6297), pp. 125–132. Available at: <https://doi.org/10.1038/348125a0>.

Brar, G. *et al.* (2019) 'Multi-omic molecular comparison of primary versus metastatic pancreatic tumours', *British journal of cancer*, 121(3), pp. 264–270. Available at: <https://doi.org/10.1038/S41416-019-0507-5>.

Brunton, H. *et al.* (2020) 'HNF4A and GATA6 Loss Reveals Therapeutically Actionable Subtypes in Pancreatic Cancer', *Cell Reports*, 31(6), p. 107625. Available at: <https://doi.org/10.1016/j.celrep.2020.107625>.

Buchholz, S.M. *et al.* (2020) 'Depletion of Macrophages Improves Therapeutic Response to Gemcitabine in Murine Pancreas Cancer', *Cancers*, 12(7), p. 1978. Available at: <https://doi.org/10.3390/CANCERS12071978>.

Bulle, A. and Lim, K.H. (2020) 'Beyond just a tight fortress: contribution of stroma to epithelial-mesenchymal transition in pancreatic cancer', *Signal Transduction and Targeted Therapy* 2020 5:1, 5(1), pp. 1–12. Available at: <https://doi.org/10.1038/s41392-020-00341-1>.

- Cambier, L. *et al.* (2014) 'Nkx2-5 regulates cardiac growth through modulation of Wnt signaling by R-spondin3', *Development (Cambridge)*, 141(15), pp. 2959–2971. Available at: <https://doi.org/10.1242/DEV.103416/-/DC1>.
- Candido, J.B. *et al.* (2018) 'CSF1R+ Macrophages Sustain Pancreatic Tumor Growth through T Cell Suppression and Maintenance of Key Gene Programs that Define the Squamous Subtype', *Cell Reports*, 23(5), pp. 1448–1460. Available at: <https://doi.org/10.1016/J.CELREP.2018.03.131>.
- Cao, Y. *et al.* (2017) 'The use of human umbilical vein endothelial cells (HUVECs) as an in vitro model to assess the toxicity of nanoparticles to endothelium: a review', *Journal of applied toxicology: JAT*, 37(12), pp. 1359–1369. Available at: <https://doi.org/10.1002/JAT.3470>.
- Carroll, S.M. *et al.* (1988) 'Double minute chromosomes can be produced from precursors derived from a chromosomal deletion', *Molecular and cellular biology*, 8(4), pp. 1525–1533. Available at: <https://doi.org/10.1128/MCB.8.4.1525-1533.1988>.
- Carter, S L *et al.* (2006a) 'A signature of chromosomal instability inferred from gene expression profiles predicts clinical outcome in multiple human cancers', *Nat Genet.* 2006/08/22, 38(9), pp. 1043–1048. Available at: <https://doi.org/10.1038/ng1861>.
- Carter, Scott L *et al.* (2006) 'A signature of chromosomal instability inferred from gene expression profiles predicts clinical outcome in multiple human cancers', *Nat Genet.* 2006/08/22, 38(9), pp. 1043–1048. Available at: <https://doi.org/10.1038/ng1861>.
- Carter, S L *et al.* (2006b) 'A signature of chromosomal instability inferred from gene expression profiles predicts clinical outcome in multiple human cancers', *Nat Genet.* 2006/08/22, 38(9), pp. 1043–1048. Available at: <https://doi.org/10.1038/ng1861>.
- Cesmebasi, A. *et al.* (2015) 'The surgical anatomy of the lymphatic system of the pancreas', *Clinical Anatomy*, 28(4), pp. 527–537. Available at: <https://doi.org/10.1002/CA.22461>.

- Chang, X.Y. *et al.* (2020) ‘RNF43 Mutations in IPMN Cases: A Potential Prognostic Factor’, *Gastroenterology Research and Practice*, 2020. Available at: <https://doi.org/10.1155/2020/1457452>.
- Chan-Seng-Yue, M. *et al.* (2020) ‘Transcription phenotypes of pancreatic cancer are driven by genomic events during tumor evolution’, *Nature Genetics*, 52(2), pp. 231–240. Available at: <https://doi.org/10.1038/s41588-019-0566-9>.
- Chao, T., Furth, E.E. and Vonderheide, R.H. (2016) ‘CXCR2-Dependent Accumulation of Tumor-Associated Neutrophils Regulates T-cell Immunity in Pancreatic Ductal Adenocarcinoma’, *Cancer Immunology Research*, 4(11), pp. 968–982. Available at: <https://doi.org/10.1158/2326-6066.CIR-16-0188>.
- Chapman, B.C. *et al.* (2018) ‘Perioperative outcomes and survival following neoadjuvant stereotactic body radiation therapy (SBRT) versus intensity-modulated radiation therapy (IMRT) in pancreatic adenocarcinoma’, *Journal of Surgical Oncology*, 117(5), pp. 1073–1083. Available at: <https://doi.org/10.1002/JSO.25004>.
- Chen, S. *et al.* (2018a) ‘fastp: an ultra-fast all-in-one FASTQ preprocessor’, *Bioinformatics*, 34(17), pp. i884–i890. Available at: <https://doi.org/10.1093/bioinformatics/bty560>.
- Chen, S. *et al.* (2018b) ‘fastp: an ultra-fast all-in-one FASTQ preprocessor’, *Bioinformatics (Oxford, England)*, 34(17), pp. i884–i890. Available at: <https://doi.org/10.1093/BIOINFORMATICS/BTY560>.
- Chen, Y. *et al.* (2021) ‘Type I collagen deletion in α SMA+ myofibroblasts augments immune suppression and accelerates progression of pancreatic cancer’, *Cancer Cell*, 39(4), pp. 548–565.e6. Available at: <https://doi.org/10.1016/j.ccell.2021.02.007>.
- Cho, S.W. *et al.* (2018) ‘Promoter of lncRNA Gene PVT1 Is a Tumor-Suppressor DNA Boundary Element’, *Cell*. 2018/05/08, 173(6), pp. 1398–1412 e22. Available at: <https://doi.org/10.1016/j.cell.2018.03.068>.
- Choi, J. Il *et al.* (2021) ‘Cancer-initiating cells in human pancreatic cancer organoids are maintained by interactions with endothelial cells’, *Cancer Letters*, 498, pp. 42–53. Available at: <https://doi.org/10.1016/j.canlet.2020.10.012>.
- Ciccolini, J. *et al.* (2016) ‘Pharmacokinetics and pharmacogenetics of Gemcitabine as a mainstay in adult and pediatric oncology: an EORTC-PAMM perspective’,

- Cancer Chemotherapy and Pharmacology*, 78(1), p. 1. Available at: <https://doi.org/10.1007/S00280-016-3003-0>.
- Cingolani, P. *et al.* (2012) ‘A program for annotating and predicting the effects of single nucleotide polymorphisms, SnpEff’, *Fly*, 6(2), pp. 80–92. Available at: <https://doi.org/10.4161/fly.19695>.
- Collisson, E.A. *et al.* (2011) ‘Subtypes of pancreatic ductal adenocarcinoma and their differing responses to therapy’, *Nature Medicine*, 17(4), pp. 500–503. Available at: <https://doi.org/10.1038/nm.2344>.
- Conroy, T. *et al.* (2018) ‘FOLFIRINOX or Gemcitabine as Adjuvant Therapy for Pancreatic Cancer’, *The New England journal of medicine*, 379(25), pp. 2395–2406. Available at: <https://doi.org/10.1056/NEJMOA1809775>.
- Delmore, J.E. *et al.* (2011) ‘BET bromodomain inhibition as a therapeutic strategy to target c-Myc’, *Cell*. 2011/09/06, 146(6), pp. 904–917. Available at: <https://doi.org/10.1016/j.cell.2011.08.017>.
- Depristo, M.A. *et al.* (2011) ‘A framework for variation discovery and genotyping using next-generation DNA sequencing data’, *Nature Genetics* 2011 43:5, 43(5), pp. 491–498. Available at: <https://doi.org/10.1038/ng.806>.
- Deshpande, V. *et al.* (2019) ‘Exploring the landscape of focal amplifications in cancer using AmpliconArchitect’, *Nature Communications*, 10(1). Available at: <https://doi.org/10.1038/s41467-018-08200-y>.
- Díaz-Gay, M. *et al.* (2018) ‘Mutational Signatures in Cancer (MuSiCa): a web application to implement mutational signatures analysis in cancer samples’, *BMC Bioinformatics*, 19(1), p. 224. Available at: <https://doi.org/10.1186/s12859-018-2234-y>.
- Drews, R.M. *et al.* (2022) ‘A pan-cancer compendium of chromosomal instability’, *Nature*, 606(7916). Available at: <https://doi.org/10.1038/s41586-022-04789-9>.
- Driehuis, E. *et al.* (2019) ‘Pancreatic cancer organoids recapitulate disease and allow personalized drug screening’, *Proc Natl Acad Sci U S A*. 2019/12/11, 116(52), pp. 26580–26590. Available at: <https://doi.org/10.1073/pnas.1911273116>.
- Drost, J. and Clevers, H. (2018) ‘Organoids in cancer research’, *Nature Reviews Cancer*, 18(7), pp. 407–418. Available at: <https://doi.org/10.1038/s41568-018-0007-6>.

- Dunne, R.F. and Hezel, A.F. (2015) ‘Genetics and Biology of Pancreatic Ductal Adenocarcinoma’, *Hematology/oncology clinics of North America*, 29(4), pp. 595–608. Available at: <https://doi.org/10.1016/J.HOC.2015.04.003>.
- Elyada, E. *et al.* (2019) ‘Cross-Species Single-Cell Analysis of Pancreatic Ductal Adenocarcinoma Reveals Antigen-Presenting Cancer-Associated Fibroblasts’, *Cancer discovery*, 9(8), pp. 1102–1123. Available at: <https://doi.org/10.1158/2159-8290.CD-19-0094>.
- Erkan, M. *et al.* (2012) ‘The role of stroma in pancreatic cancer: diagnostic and therapeutic implications’, *Nature Reviews Gastroenterology & Hepatology*, 9(8), pp. 454–467. Available at: <https://doi.org/10.1038/nrgastro.2012.115>.
- Evan, T., Wang, V.M.Y. and Behrens, A. (2022) ‘The roles of intratumour heterogeneity in the biology and treatment of pancreatic ductal adenocarcinoma’, *Oncogene* 2022 41:42, 41(42), pp. 4686–4695. Available at: <https://doi.org/10.1038/s41388-022-02448-x>.
- Farshadi, E.A. *et al.* (2021) ‘Organoids derived from neoadjuvant FOLFIRINOX patients recapitulate therapy resistance in pancreatic ductal adenocarcinoma’, *Clinical Cancer Research*, 27(23), pp. 6602–6612. Available at: <https://doi.org/10.1158/1078-0432.CCR-21-1681/673938/AM/ORGANOIDS-DERIVED-FROM-NEOADJUVANT-FOLFIRINOX>.
- Favero, F. *et al.* (2015) ‘Sequenza: allele-specific copy number and mutation profiles from tumor sequencing data’, *Annals of Oncology*, 26(1), p. 64. Available at: <https://doi.org/10.1093/ANNONC/MDU479>.
- Ferreira, R.M.M. *et al.* (2017) ‘Duct- and Acinar-Derived Pancreatic Ductal Adenocarcinomas Show Distinct Tumor Progression and Marker Expression’, *Cell Reports*, 21(4), pp. 966–978. Available at: <https://doi.org/10.1016/J.CELREP.2017.09.093>.
- Fesinmeyer, M. *et al.* (2005) ‘Differences in Survival by Histologic Type of Pancreatic Cancer’, *Cancer Epidemiology, Biomarkers & Prevention*, 14(7), pp.1766-1773. Available at: <https://dx.doi.org/10.1158/1055-9965.EPI-05-0120>.
- Flowers, B.M. *et al.* (2021) ‘Cell of Origin Influences Pancreatic Cancer Subtype’, *Cancer Discovery*, 11(3), pp. 660–77. Available at: <https://doi.org/10.1158/2159-8290.CD-20-0633>.

- Garcia, J. *et al.* (2012) ‘Tie1 deficiency induces endothelial–mesenchymal transition’, *EMBO Reports*, 13(5), p. 431. Available at: <https://doi.org/10.1038/EMBOR.2012.29>.
- Garcia, M. *et al.* (2020) ‘Sarek: A portable workflow for whole-genome sequencing analysis of germline and somatic variants’, *F1000Research*, 9, p. 63. Available at: <https://doi.org/10.12688/F1000RESEARCH.16665.2>.
- Ghafouri-Fard, S. *et al.* (2022) ‘A review on the role of cyclin dependent kinases in cancers’, *Cancer Cell International* 2022 22:1, 22(1), pp. 1–69. Available at: <https://doi.org/10.1186/S12935-022-02747-Z>.
- Gorchs, L. and Kaipe, H. (2021) ‘Interactions between Cancer-Associated Fibroblasts and T Cells in the Pancreatic Tumor Microenvironment and the Role of Chemokines’, *Cancers (Basel)*, 13(12), p. 2995. Available at: <https://doi.org/10.3390/CANCERS13122995>.
- Goto, N. *et al.* (2022) ‘Lymphatics and fibroblasts support intestinal stem cells in homeostasis and injury’, *Cell Stem Cell*, 29(8), pp. 1246–1261.e6. Available at: <https://doi.org/10.1016/j.stem.2022.06.013>.
- Gradishar, W.J. (2006) ‘Albumin-bound paclitaxel: a next-generation taxane’, *Expert opinion on pharmacotherapy*, 7(8), pp. 1041–1053. Available at: <https://doi.org/10.1517/14656566.7.8.1041>.
- Grapin-Botton, A. (2005) ‘Ductal cells of the pancreas’, *The International Journal of Biochemistry & Cell Biology*, 37(3), pp. 504–510. Available at: <https://doi.org/10.1016/J.BIOCEL.2004.07.010>.
- Grün, D. *et al.* (2016) ‘De Novo Prediction of Stem Cell Identity using Single-Cell Transcriptome Data’, *Cell stem cell*, 19(2), pp. 266–277. Available at: <https://doi.org/10.1016/J.STEM.2016.05.010>.
- Guerra, C. *et al.* (2007) ‘Chronic pancreatitis is essential for induction of pancreatic ductal adenocarcinoma by K-Ras oncogenes in adult mice’, *Cancer cell*, 11(3), pp. 291–302. Available at: <https://doi.org/10.1016/J.CCR.2007.01.012>.
- Habbe, N. *et al.* (2008) ‘Spontaneous induction of murine pancreatic intraepithelial neoplasia (mPanIN) by acinar cell targeting of oncogenic Kras in adult mice’, *Proceedings of the National Academy of Sciences of the United States of America*,

- 105(48), pp. 18913–18918. Available at: <https://doi.org/10.1073/PNAS.0810097105>.
- Haber, D.A. and Schimke, R.T. (1981) ‘Unstable amplification of an altered dihydrofolate reductase gene associated with double-minute chromosomes’, *Cell*, 26(3 Pt 1), pp. 355–362. Available at: [https://doi.org/10.1016/0092-8674\(81\)90204-X](https://doi.org/10.1016/0092-8674(81)90204-X).
- Habtezion, A., Edderkaoui, M. and Pandol, S.J. (2016) ‘Macrophages and Pancreatic ductal adenocarcinoma’, *Cancer letters*, 381(1), p. 211. Available at: <https://doi.org/10.1016/J.CANLET.2015.11.049>.
- Hackert, T. and Büchler, M.W. (2013) ‘Pancreatic Cancer: Advances in Treatment, Results and Limitations’, *Digestive Diseases*, 31(1), pp. 51–56. Available at: <https://doi.org/10.1159/000347178>.
- Hanahan, D. and Weinberg, R.A. (2000) ‘The Hallmarks of Cancer’, *Cell*, 100(1), pp. 57–70. Available at: [https://doi.org/10.1016/S0092-8674\(00\)81683-9](https://doi.org/10.1016/S0092-8674(00)81683-9).
- Hänzelmann, S., Castelo, R. and Guinney, J. (2013) ‘GSVA: Gene set variation analysis for microarray and RNA-Seq data’, *BMC Bioinformatics*, 14(1), pp. 1–15. Available at: <https://doi.org/10.1186/1471-2105-14-7/FIGURES/7>.
- Hao, Y. *et al.* (2021) ‘Integrated analysis of multimodal single-cell data’, *Cell*, 184(13), pp. 3573–3587.e29. Available at: <https://doi.org/10.1016/J.CELL.2021.04.048>.
- Hayashi, A. *et al.* (2020) ‘A unifying paradigm for transcriptional heterogeneity and squamous features in pancreatic ductal adenocarcinoma’, *Nature Cancer*, 1(1), pp. 59–74. Available at: <https://doi.org/10.1038/s43018-019-0010-1>.
- He, T.C. *et al.* (1998) ‘Identification of c-MYC as a target of the APC pathway’, *Science*. 1998/09/04, 281(5382), pp. 1509–1512. Available at: <https://doi.org/10.1126/science.281.5382.1509>.
- Hegyí, P. *et al.* (2011) ‘Pancreatic Ductal Bicarbonate Secretion: Challenge of the Acinar Acid Load’, *Frontiers in Physiology*, 2. Available at: <https://doi.org/10.3389/FPHYS.2011.00036>.
- Hessmann, E. *et al.* (2020) ‘Microenvironmental determinants of pancreatic cancer’, *Physiological Reviews*, 100(4), pp. 1707–1751. Available at:

<https://doi.org/10.1152/PHYSREV.00042.2019/ASSET/IMAGES/LARGE/Z9J0042029550009.JPEG>.

Hezel, A.F. *et al.* (2006) ‘Genetics and biology of pancreatic ductal adenocarcinoma’, *Genes and Development*, 20(10), pp. 1218–1249. Available at: <https://doi.org/10.1101/gad.1415606>.

Hofer, M. and Lutolf, M.P. (2021) ‘Engineering organoids’, *Nature Reviews Materials* 2021 6:5, 6(5), pp. 402–420. Available at: <https://doi.org/10.1038/s41578-021-00279-y>.

Von Hoff, D.D. (1991) ‘New mechanisms of gene amplification in drug resistance (the episome model)’, *Cancer treatment and research*, 57, pp. 1–11. Available at: https://doi.org/10.1007/978-1-4615-3872-1_1.

Von Hoff, D.D. *et al.* (2013) ‘Increased survival in pancreatic cancer with nab-paclitaxel plus gemcitabine’, *The New England journal of medicine*, 369(18), pp. 1691–1703. Available at: <https://doi.org/10.1056/NEJMOA1304369>.

Hosein, A.N. *et al.* (2022) ‘Translational advances in pancreatic ductal adenocarcinoma therapy’, *Nature Cancer* 2022 3:3, 3(3), pp. 272–286. Available at: <https://doi.org/10.1038/s43018-022-00349-2>.

Hosoi, F. *et al.* (2009) ‘N-myc Downstream Regulated Gene 1/Cap43 Suppresses Tumor Growth and Angiogenesis of Pancreatic Cancer through Attenuation of Inhibitor of κ B Kinase β Expression’, *Cancer Research*, 69(12), pp. 4983–4991. Available at: <https://doi.org/10.1158/0008-5472.CAN-08-4882>.

Hu, H. *et al.* (2016) ‘The M2 phenotype of tumor-associated macrophages in the stroma confers a poor prognosis in pancreatic cancer’, *Tumour biology : the journal of the International Society for Oncodevelopmental Biology and Medicine*, 37(7), pp. 8657–8664. Available at: <https://doi.org/10.1007/S13277-015-4741-Z>.

Hu, J.X. *et al.* (2021) ‘Pancreatic cancer: A review of epidemiology, trend, and risk factors’, *World Journal of Gastroenterology*, 27(27), p. 4298. Available at: <https://doi.org/10.3748/WJG.V27.I27.4298>.

Hung, K.L. *et al.* (2021) ‘ecDNA hubs drive cooperative intermolecular oncogene expression’, *Nature* 2021 600:7890, 600(7890), pp. 731–736. Available at: <https://doi.org/10.1038/s41586-021-04116-8>.

- Hwang, W.L. *et al.* (2020) ‘Single-nucleus and spatial transcriptomics of archival pancreatic cancer reveals multi-compartment reprogramming after neoadjuvant treatment’, *bioRxiv* [Preprint]. Available at: <https://doi.org/10.1101/2020.08.25.267336>.
- Hwang, W.L. *et al.* (2022) ‘Single-nucleus and spatial transcriptome profiling of pancreatic cancer identifies multicellular dynamics associated with neoadjuvant treatment’, *Nature genetics*, 54(8), pp. 1178–1191. Available at: <https://doi.org/10.1038/S41588-022-01134-8>.
- Jin, L., Kim, H.S. and Shi, J. (2021) ‘Neutrophil in the Pancreatic Tumor Microenvironment’, *Biomolecules*, 11(8), p. 1170. Available at: <https://doi.org/10.3390/BIOM11081170>.
- Jones, S., Zhang, X., Parsons, D.W., *et al.* (2008) ‘Core signaling pathways in human pancreatic cancers revealed by global genomic analyses’, *Science*, 321(5897), pp. 1801–1806. Available at: <https://doi.org/10.1126/science.1164368>.
- Jones, S., Zhang, X., Williams Parsons, D., *et al.* (2008) ‘Core Signaling Pathways in Human Pancreatic Cancers Revealed by Global Genomic Analyses NIH Public Access’, *Science*, 321(5897), pp. 1801–1806. Available at: <https://doi.org/10.1126/science.1164368>.
- Juiz, N. *et al.* (2020) ‘Basal-like and classical cells coexist in pancreatic cancer revealed by single-cell analysis on biopsy-derived pancreatic cancer organoids from the classical subtype’, *The FASEB Journal*, 34(9), pp. 12214–12228. Available at: <https://doi.org/10.1096/FJ.202000363RR>.
- Kanda, M. *et al.* (2012) ‘Presence of somatic mutations in most early-stage pancreatic intraepithelial neoplasia’, *Gastroenterology*, 142(4), pp. 730-733.e9. Available at: <https://doi.org/10.1053/j.gastro.2011.12.042>.
- Kandoth, C. *et al.* (2018) ‘mskcc/vcf2maf: vcf2maf v1.6.16’. Available at: <https://doi.org/10.5281/ZENODO.1185418>.
- Katsuta, E. *et al.* (2019) ‘Pancreatic adenocarcinomas with mature blood vessels have better overall survival’, *Scientific Reports*, 9(1). Available at: <https://doi.org/10.1038/S41598-018-37909-5>.
- Kim, E.J. *et al.* (2014) ‘Pilot Clinical Trial of Hedgehog Pathway Inhibitor GDC-0449 (Vismodegib) in Combination with Gemcitabine in Patients with Metastatic

Pancreatic Adenocarcinoma’, *Clinical Cancer Research*, 20(23), pp. 5937–5945. Available at: <https://doi.org/10.1158/1078-0432.CCR-14-1269>.

Kim, Hoon *et al.* (2020) ‘Extrachromosomal DNA is associated with oncogene amplification and poor outcome across multiple cancers’, *Nature Genetics* 2020 52:9, 52(9), pp. 891–897. Available at: <https://doi.org/10.1038/s41588-020-0678-2>.

Kim, H *et al.* (2020) ‘Extrachromosomal DNA is associated with oncogene amplification and poor outcome across multiple cancers’, *Nat Genet.* 2020/08/19, 52(9), pp. 891–897. Available at: <https://doi.org/10.1038/s41588-020-0678-2>.

Kloesch, B. *et al.* (2021) ‘A GATA6-centred gene regulatory network involving HNFs and Δ Np63 controls plasticity and immune escape in pancreatic cancer’, *Gut*, p. 321397. Available at: <https://doi.org/10.1136/gutjnl-2020-321397>.

Ko, A.H. *et al.* (2016) ‘A Phase I Study of FOLFIRINOX Plus IPI-926, a Hedgehog Pathway Inhibitor, for Advanced Pancreatic Adenocarcinoma’, *Pancreas*, 45(3), pp. 370–375. Available at: <https://doi.org/10.1097/MPA.0000000000000458>.

Koche, R.P. *et al.* (2020) ‘Extrachromosomal circular DNA drives oncogenic genome remodeling in neuroblastoma’, *Nature genetics*, 52(1), p. 29. Available at: <https://doi.org/10.1038/S41588-019-0547-Z>.

Kopp, J.L. *et al.* (2012) ‘Identification of Sox9-dependent acinar-to-ductal reprogramming as the principal mechanism for initiation of pancreatic ductal adenocarcinoma’, *Cancer cell*, 22(6), p. 737. Available at: <https://doi.org/10.1016/J.CCR.2012.10.025>.

Korotkevich, G. *et al.* (2021) ‘Fast gene set enrichment analysis’, *bioRxiv*, p. 60012. Available at: <https://doi.org/10.1101/060012>.

Krieger, T.G. *et al.* (2021) ‘Single-cell analysis of patient-derived PDAC organoids reveals cell state heterogeneity and a conserved developmental hierarchy’, *Nature Communications* 2021 12:1, 12(1), pp. 1–13. Available at: <https://doi.org/10.1038/s41467-021-26059-4>.

Kühl, M. *et al.* (2000) ‘The Wnt/Ca²⁺ pathway A new vertebrate Wnt signaling pathway takes shape’, *Trends in Genetics*, 16(7), pp. 279–283. Available at: [https://doi.org/10.1016/S0168-9525\(00\)02028-X](https://doi.org/10.1016/S0168-9525(00)02028-X).

- Kuleshov, M. V *et al.* (2016) ‘Enrichr: a comprehensive gene set enrichment analysis web server 2016 update.’, *Nucleic acids research*, 44(W1), pp. W90-7. Available at: <https://doi.org/10.1093/nar/gkw377>.
- Lange, J.T. *et al.* (2022) ‘The evolutionary dynamics of extrachromosomal DNA in human cancers’, *Nature Genetics*, 54(10). Available at: <https://doi.org/10.1038/s41588-022-01177-x>.
- de Lau, W. *et al.* (2012) ‘Peyer’s patch M cells derived from Lgr5(+) stem cells require SpiB and are induced by RankL in cultured “miniguts”’, *Molecular and cellular biology*, 32(18), pp. 3639–3647. Available at: <https://doi.org/10.1128/MCB.00434-12>.
- Lawlor, N. *et al.* (2017) ‘Single-cell transcriptomes identify human islet cell signatures and reveal cell-type-specific expression changes in type 2 diabetes’, *Genome research*, 27(2), pp. 208–222. Available at: <https://doi.org/10.1101/GR.212720.116>.
- Lee, A.Y.L. *et al.* (2019) ‘Cell of origin affects tumour development and phenotype in pancreatic ductal adenocarcinoma’, *Gut*, 68(3), pp. 487–498. Available at: <https://doi.org/10.1136/gutjnl-2017-314426>.
- Lennon, A.M. *et al.* (2014) ‘The early detection of pancreatic cancer: What will it take to diagnose and treat curable pancreatic neoplasia?’, *Cancer Research*, 74(13), pp. 3381–3389. Available at: <https://doi.org/10.1158/0008-5472.CAN-14-0734/659484/P/THE-EARLY-DETECTION-OF-PANCREATIC-CANCER-WHAT-WILL>.
- Leung, C.M. *et al.* (2022) ‘A guide to the organ-on-a-chip’, *Nature Reviews Methods Primers* 2022 2:1, 2(1), pp. 1–29. Available at: <https://doi.org/10.1038/s43586-022-00118-6>.
- Levan, G. *et al.* (1976) ‘Double minute chromosomes are not centromeric regions of the host chromosomes’, *Hereditas*. 1976/01/01, 83(1), pp. 83–90. Available at: <https://doi.org/10.1111/j.1601-5223.1976.tb01573.x>.
- Li, H. (2013) ‘Aligning sequence reads, clone sequences and assembly contigs with BWA-MEM’, *arXiv: Genomics* [Preprint]. Available at: <https://doi.org/10.6084/M9.FIGSHARE.963153.V1>.

- Li, H. and Durbin, R. (2009) 'Fast and accurate short read alignment with Burrows–Wheeler transform', *Bioinformatics*, 25(14), pp. 1754–1760. Available at: <https://doi.org/10.1093/BIOINFORMATICS/BTP324>.
- Lianyuan, T. *et al.* (2020) 'Tumor associated neutrophils promote the metastasis of pancreatic ductal adenocarcinoma', *Cancer biology & therapy*, 21(10), pp. 937–945. Available at: <https://doi.org/10.1080/15384047.2020.1807250>.
- Liberzon, A. *et al.* (2011) 'Molecular signatures database (MSigDB) 3.0', *Bioinformatics*. 2011/05/07, 27(12), pp. 1739–1740. Available at: <https://doi.org/10.1093/bioinformatics/btr260>.
- Ligorio, M. *et al.* (2019) 'Stromal Microenvironment Shapes the Intratumoral Architecture of Pancreatic Cancer', *Cell*, 178(1), pp. 160-175.e27. Available at: <https://doi.org/10.1016/j.cell.2019.05.012>.
- Lodestijn, S.C. *et al.* (2021) 'Stem Cells in the Exocrine Pancreas during Homeostasis, Injury, and Cancer', *Cancers 2021, Vol. 13, Page 3295*, 13(13), p. 3295. Available at: <https://doi.org/10.3390/CANCERS13133295>.
- Logsdon, C.D. *et al.* (2013) 'The role of protein synthesis and digestive enzymes in acinar cell injury', *Nature Reviews Gastroenterology & Hepatology* 2013 10:6, 10(6), pp. 362–370. Available at: <https://doi.org/10.1038/nrgastro.2013.36>.
- Love, Michael I., Huber, W. and Anders, S. (2014) 'Moderated estimation of fold change and dispersion for RNA-seq data with DESeq2', *Genome Biol.* 2014/12/18, 15(12), p. 550. Available at: <https://doi.org/10.1186/s13059-014-0550-8>.
- Love, M I, Huber, W. and Anders, S. (2014) 'Moderated estimation of fold change and dispersion for RNA-seq data with DESeq2', *Genome Biol.* 2014/12/18, 15(12), p. 550. Available at: <https://doi.org/10.1186/s13059-014-0550-8>.
- Lowery, M.A. *et al.* (2018) 'Prospective Evaluation of Germline Alterations in Patients With Exocrine Pancreatic Neoplasms', *JNCI Journal of the National Cancer Institute*, 110(10), p. 1067. Available at: <https://doi.org/10.1093/JNCI/DJY024>.
- Luebeck, J. *et al.* (2023) 'Extrachromosomal DNA in the cancerous transformation of Barrett's oesophagus', *Nature* 2023 616:7958, 616(7958), pp. 798–805. Available at: <https://doi.org/10.1038/s41586-023-05937-5>.

- Maddipati, R. *et al.* (2022) ‘MYC Levels Regulate Metastatic Heterogeneity in Pancreatic Adenocarcinoma’, *Cancer discovery*, 12(2), pp. 542–561. Available at: <https://doi.org/10.1158/2159-8290.CD-20-1826>.
- Maitra, A. *et al.* (2003) ‘Multicomponent analysis of the pancreatic adenocarcinoma progression model using a pancreatic intraepithelial neoplasia tissue microarray’, *Modern pathology : an official journal of the United States and Canadian Academy of Pathology, Inc*, 16(9), pp. 902–912. Available at: <https://doi.org/10.1097/01.MP.0000086072.56290.FB>.
- Makena, M.R. *et al.* (2019) ‘Wnt/ β -Catenin Signaling: The Culprit in Pancreatic Carcinogenesis and Therapeutic Resistance’, *International Journal of Molecular Sciences*, 20(17). Available at: <https://doi.org/10.3390/IJMS20174242>.
- Malinova, A. *et al.* (2021) ‘Cell Lineage Infidelity in PDAC Progression and Therapy Resistance’, *Frontiers in Cell and Developmental Biology*, 9, p. 795251. Available at: <https://doi.org/10.3389/FCELL.2021.795251/BIBTEX>.
- Martin, M. (2011) ‘Cutadapt removes adapter sequences from high-throughput sequencing reads’, *EMBnet.journal*, 17(1), pp. 10–12. Available at: <https://doi.org/10.14806/EJ.17.1.200>.
- Martinelli, P. *et al.* (2017) ‘GATA6 regulates EMT and tumour dissemination, and is a marker of response to adjuvant chemotherapy in pancreatic cancer’, *Gut*, 66(9), pp. 1665–1676. Available at: <https://doi.org/10.1136/gutjnl-2015-311256>.
- Marusyk, A., Janiszewska, M. and Polyak, K. (2020) ‘Intratumor Heterogeneity: The Rosetta Stone of Therapy Resistance’, *Cancer cell*, 37(4), pp. 471–484. Available at: <https://doi.org/10.1016/J.CCELL.2020.03.007>.
- Mayakonda, A. *et al.* (2018) ‘Maftools: efficient and comprehensive analysis of somatic variants in cancer.’, *Genome research*, 28(11), pp. 1747–1756. Available at: <https://doi.org/10.1101/gr.239244.118>.
- McKenna, A. *et al.* (2010) ‘The Genome Analysis Toolkit: a MapReduce framework for analyzing next-generation DNA sequencing data’, *Genome research*, 20(9), pp. 1297–1303. Available at: <https://doi.org/10.1101/GR.107524.110>.
- Mermel, C.H. *et al.* (2011) ‘GISTIC2.0 facilitates sensitive and confident localization of the targets of focal somatic copy-number alteration in human

cancers’, *Genome Biology*, 12(4), pp. 1–14. Available at: <https://doi.org/10.1186/GB-2011-12-4-R41/FIGURES/7>.

Miyabayashi, K. *et al.* (2020) ‘Intraductal transplantation models of human pancreatic ductal adenocarcinoma reveal progressive transition of molecular subtypes’, *Cancer Discovery*, 10(10), pp. 1566–1589. Available at: <https://doi.org/10.1158/2159-8290.CD-20-0133>.

Moffitt, R.A. *et al.* (2015) ‘Virtual microdissection identifies distinct tumor- and stroma-specific subtypes of pancreatic ductal adenocarcinoma’, *Nature Genetics*, 47(10), pp. 1168–1178. Available at: <https://doi.org/10.1038/ng.3398>.

van Mourik, J.A. *et al.* (1985) ‘Vascular endothelial cells synthesize a plasma membrane protein indistinguishable from the platelet membrane glycoprotein IIa’, *Journal of Biological Chemistry*, 260(20), pp. 11300–11306. Available at: [https://doi.org/10.1016/s0021-9258\(17\)39180-9](https://doi.org/10.1016/s0021-9258(17)39180-9).

Mueller, S. *et al.* (2018) ‘Evolutionary routes and KRAS dosage define pancreatic cancer phenotypes’, *Nature* 2018 554:7690, 554(7690), pp. 62–68. Available at: <https://doi.org/10.1038/nature25459>.

Murakami, T. *et al.* (2019) ‘Role of the tumor microenvironment in pancreatic cancer’, *Annals of Gastroenterological Surgery*, 3(2), pp. 130–137. Available at: <https://doi.org/10.1002/ags3.12225>.

Muraro, M.J. *et al.* (2016) ‘A Single-Cell Transcriptome Atlas of the Human Pancreas’, *Cell systems*, 3(4), pp. 385-394.e3. Available at: <https://doi.org/10.1016/J.CELS.2016.09.002>.

Muratore, M., Santos, C. and Rorsman, P. (2021) ‘The vascular architecture of the pancreatic islets: A homage to August Krogh’, *Comparative Biochemistry and Physiology, Part A*, 252, p. 110846. Available at: <https://doi.org/10.1016/j.cbpa.2020.110846>.

Nathanson, D.A. *et al.* (2014) ‘Targeted therapy resistance mediated by dynamic regulation of extrachromosomal mutant EGFR DNA’, *Science (New York, N.Y.)*, 343(6166), pp. 72–76. Available at: <https://doi.org/10.1126/SCIENCE.1241328>.

Nicolle, R. *et al.* (2020) ‘Establishment of a pancreatic adenocarcinoma molecular gradient (PAMG) that predicts the clinical outcome of pancreatic cancer’,

EBioMedicine, 57, p. 102858. Available at: <https://doi.org/10.1016/J.EBIOM.2020.102858>.

Nielsen, S.R. *et al.* (2021) ‘Suppression of tumor-associated neutrophils by lorlatinib attenuates pancreatic cancer growth and improves treatment with immune checkpoint blockade’, *Nature Communications*, 12(1), p. 3414. Available at: <https://doi.org/10.1038/s41467-021-23731-7>.

Noll, E.M. *et al.* (2016) ‘CYP3A5 mediates basal and acquired therapy resistance in different subtypes of pancreatic ductal adenocarcinoma’, *Nature medicine*, 22(3), p. 278. Available at: <https://doi.org/10.1038/NM.4038>.

Notta, F. *et al.* (2016) ‘A renewed model of pancreatic cancer evolution based on genomic rearrangement patterns’, *Nature*, 538(7625), pp. 378–382. Available at: <https://doi.org/10.1038/NATURE19823>.

Nywening, T.M. *et al.* (2018) ‘Targeting both tumour-associated CXCR2+ neutrophils and CCR2+ macrophages disrupts myeloid recruitment and improves chemotherapeutic responses in pancreatic ductal adenocarcinoma’, *Gut*, 67(6), pp. 1112–1123. Available at: <https://doi.org/10.1136/GUTJNL-2017-313738>.

Oba, A. *et al.* (2020) ‘Neoadjuvant Treatment in Pancreatic Cancer’, *Frontiers in Oncology*, 10, p. 245. Available at: <https://doi.org/10.3389/FONC.2020.00245>.

Öhlund, D. *et al.* (2017) ‘Distinct populations of inflammatory fibroblasts and myofibroblasts in pancreatic cancer’, *The Journal of experimental medicine*, 214(3), pp. 579–596. Available at: <https://doi.org/10.1084/jem.20162024>.

Öhlund, D., Elyada, E. and Tuveson, D. (2014) ‘Fibroblast heterogeneity in the cancer wound’, *The Journal of Experimental Medicine*, 211(8), p. 1503. Available at: <https://doi.org/10.1084/JEM.20140692>.

Olive, K.P. *et al.* (2009) ‘Inhibition of Hedgehog signaling enhances delivery of chemotherapy in a mouse model of pancreatic cancer’, *Science*, 324(5933), pp. 1457–1461. Available at: <https://doi.org/10.1126/SCIENCE.1171362>.

Özdemir, B.C. *et al.* (2014) ‘Depletion of Carcinoma-Associated Fibroblasts and Fibrosis Induces Immunosuppression and Accelerates Pancreas Cancer with Diminished Survival’, *Cancer cell*, 25(6), p. 719. Available at: <https://doi.org/10.1016/J.CCR.2014.04.005>.

- Pandiri, A.R. (2014) ‘Overview of Exocrine Pancreatic Pathobiology’, *Toxicologic pathology*, 42(1), p. 207. Available at: <https://doi.org/10.1177/0192623313509907>.
- Pandol, S.J. (2010) ‘Anatomy’, in. Morgan & Claypool Life Sciences. Available at: <https://www.ncbi.nlm.nih.gov/books/NBK54134/> (Accessed: 11 July 2023).
- Patro, R. *et al.* (2017) ‘Salmon provides fast and bias-aware quantification of transcript expression.’, *Nature methods*, 14(4), pp. 417–419. Available at: <https://doi.org/10.1038/nmeth.4197>.
- Peng, J. *et al.* (2019) ‘Single-cell RNA-seq highlights intra-tumoral heterogeneity and malignant progression in pancreatic ductal adenocarcinoma’, *Cell Research*, 29(9), pp. 725–738. Available at: <https://doi.org/10.1038/s41422-019-0195-y>.
- Porter, R.L. *et al.* (2019) ‘Epithelial to mesenchymal plasticity and differential response to therapies in pancreatic ductal adenocarcinoma’, *Proceedings of the National Academy of Sciences of the United States of America*, 116(52), pp. 26835–26845. Available at: <https://doi.org/10.1073/pnas.1914915116>.
- Priestley, P. *et al.* (2019) ‘Pan-cancer whole-genome analyses of metastatic solid tumours’, *Nature*. 2019/10/28, 575(7781), pp. 210–216. Available at: <https://doi.org/10.1038/s41586-019-1689-y>.
- Principe, D.R. *et al.* (2021) ‘The Current Treatment Paradigm for Pancreatic Ductal Adenocarcinoma and Barriers to Therapeutic Efficacy’, *Frontiers in Oncology*, 11, p. 688377. Available at: <https://doi.org/10.3389/FONC.2021.688377/BIBTEX>.
- Proffitt, K.D. *et al.* (2013) ‘Pharmacological inhibition of the Wnt acyltransferase PORCN prevents growth of WNT-driven mammary cancer’, *Cancer Research*, 73(2), pp. 502–507. Available at: <https://doi.org/10.1158/0008-5472.CAN-12-2258/650690/AM/PHARMACOLOGICAL-INHIBITION-OF-THE-WNT>.
- Provenzano, P.P. *et al.* (2012) ‘Enzymatic Targeting of the Stroma Ablates Physical Barriers to Treatment of Pancreatic Ductal Adenocarcinoma’, *Cancer Cell*, 21(3), pp. 418–429. Available at: <https://doi.org/10.1016/J.CCR.2012.01.007>.
- Puleo, F. *et al.* (2018) ‘Stratification of Pancreatic Ductal Adenocarcinomas Based on Tumor and Microenvironment Features’, *Gastroenterology*, 155(6), pp. 1999–2013. Available at: <https://doi.org/10.1053/j.gastro.2018.08.033>.

- Quiñonero, F. *et al.* (2019) 'The challenge of drug resistance in pancreatic ductal adenocarcinoma: a current overview', *Cancer Biology & Medicine*, 16(4), p. 688. Available at: <https://doi.org/10.20892/J.ISSN.2095-3941.2019.0252>.
- Quintanilha, J.C.F. *et al.* (2023) 'Tumor Mutational Burden in Real-World Patients With Pancreatic Cancer: Genomic Alterations and Predictive Value for Immune Checkpoint Inhibitor Effectiveness.', *JCO precision oncology*, 7(7), p. e2300092. Available at: <https://doi.org/10.1200/PO.23.00092>.
- Raghavan, Srivatsan *et al.* (2021) 'Microenvironment drives cell state, plasticity, and drug response in pancreatic cancer', *Cell*, 184(25), pp. 6119-6137.e26. Available at: <https://doi.org/10.1016/J.CELL.2021.11.017>.
- Raghavan, S *et al.* (2021) 'Microenvironment drives cell state, plasticity, and drug response in pancreatic cancer', *Cell*. 2021/12/11, 184(25), pp. 6119-6137 e26. Available at: <https://doi.org/10.1016/j.cell.2021.11.017>.
- Ramirez, F. *et al.* (2014) 'deepTools: a flexible platform for exploring deep-sequencing data', *Nucleic Acids Res.* 2014/05/07, 42(Web Server issue), pp. W187-91. Available at: <https://doi.org/10.1093/nar/gku365>.
- Raphael, B.J. *et al.* (2017) 'Integrated Genomic Characterization of Pancreatic Ductal Adenocarcinoma', *Cancer cell*, 32(2), pp. 185-203.e13. Available at: <https://doi.org/10.1016/J.CCELL.2017.07.007>.
- Raymond, E. *et al.* (2002) 'Cellular and molecular pharmacology of oxaliplatin', *Molecular Cancer Therapeutics*.
- Reichert, M. and Rustgi, A.K. (2011) 'Pancreatic ductal cells in development, regeneration, and neoplasia', *The Journal of Clinical Investigation*, 121(12), p. 4572. Available at: <https://doi.org/10.1172/JCI57131>.
- Rhim, A.D. *et al.* (2014) 'Stromal elements act to restrain, rather than support, pancreatic ductal adenocarcinoma', *Cancer Cell*, 25(6), pp. 735–747. Available at: <https://doi.org/10.1016/J.CCR.2014.04.021>.
- Röder, P. V. *et al.* (2016) 'Pancreatic regulation of glucose homeostasis', *Experimental & Molecular Medicine*, 48(3), p. e219. Available at: <https://doi.org/10.1038/EMM.2016.6>.

- Rosen, M.N., Goodwin, R.A. and Vickers, M.M. (2021) 'BRCA mutated pancreatic cancer: A change is coming', *World Journal of Gastroenterology*, 27(17), p. 1943. Available at: <https://doi.org/10.3748/WJG.V27.I17.1943>.
- Ruiz, J.C. and Wahl, G.M. (1990) 'Chromosomal destabilization during gene amplification.', *Molecular and Cellular Biology*, 10(6), p. 3056. Available at: <https://doi.org/10.1128/MCB.10.6.3056>.
- Ruscetti, M. *et al.* (2020) 'Senescence-Induced Vascular Remodeling Creates Therapeutic Vulnerabilities in Pancreas Cancer', *Cell*, 181(2), pp. 424–441. Available at: <https://doi.org/10.1016/j.cell.2020.03.008>.
- Sarantis, P. *et al.* (2020) 'Pancreatic ductal adenocarcinoma: Treatment hurdles, tumor microenvironment and immunotherapy', *World Journal of Gastrointestinal Oncology*, 12(2), p. 173. Available at: <https://doi.org/10.4251/WJGO.V12.I2.173>.
- Schoenlein, P. V. *et al.* (2003) 'Radiation therapy depletes extrachromosomally amplified drug resistance genes and oncogenes from tumor cells via micronuclear capture of episomes and double minute chromosomes', *International Journal of Radiation Oncology Biology Physics*, 55(4), pp. 1051–1065. Available at: [https://doi.org/10.1016/S0360-3016\(02\)04473-5](https://doi.org/10.1016/S0360-3016(02)04473-5).
- Scholz, B. *et al.* (2016) 'Endothelial RSPO3 Controls Vascular Stability and Pruning through Non-canonical WNT/Ca(2+)/NFAT Signaling', *Developmental cell*, 36(1), pp. 79–93. Available at: <https://doi.org/10.1016/J.DEVCEL.2015.12.015>.
- Schulte, A. *et al.* (2012) 'Glioblastoma stem-like cell lines with either maintenance or loss of high-level EGFR amplification, generated via modulation of ligand concentration', *Clinical cancer research: an official journal of the American Association for Cancer Research*, 18(7), pp. 1901–1913. Available at: <https://doi.org/10.1158/1078-0432.CCR-11-3084>.
- Schutte, M. *et al.* (1997) 'Abrogation of the Rb/p16 tumor-suppressive pathway in virtually all pancreatic carcinomas.', *Cancer research*, 57(15), pp. 3126–30.
- Segerstolpe, Å. *et al.* (2016) 'Single-Cell Transcriptome Profiling of Human Pancreatic Islets in Health and Type 2 Diabetes', *Cell metabolism*, 24(4), pp. 593–607. Available at: <https://doi.org/10.1016/J.CMET.2016.08.020>.

Seino, Takashi *et al.* (2018) ‘Human Pancreatic Tumor Organoids Reveal Loss of Stem Cell Niche Factor Dependence during Disease Progression’, *Cell Stem Cell*, 22(3), pp. 454-467.e6. Available at: <https://doi.org/10.1016/J.STEM.2017.12.009>.

Seino, T *et al.* (2018) ‘Human Pancreatic Tumor Organoids Reveal Loss of Stem Cell Niche Factor Dependence during Disease Progression’, *Cell Stem Cell*. 2018/01/18, 22(3), pp. 454-467 e6. Available at: <https://doi.org/10.1016/j.stem.2017.12.009>.

Siegel, R.L. *et al.* (2023) ‘Cancer statistics, 2023’, *CA: A Cancer Journal for Clinicians*, 73(1), pp. 17–48. Available at: <https://doi.org/10.3322/CAAC.21763>.

Sodir, N.M. *et al.* (2020) ‘MYC instructs and maintains pancreatic adenocarcinoma phenotype’, *Cancer Discovery*, 10(4), pp. 588–607. Available at: <https://doi.org/10.1158/2159-8290.CD-19-0435>.

Somerville, T.D. *et al.* (2020) ‘Squamous trans-differentiation of pancreatic cancer cells promotes stromal inflammation’, *eLife*, 9. Available at: <https://doi.org/10.7554/ELIFE.53381>.

Soneson, C., Love, M.I. and Robinson, M.D. (2016) ‘Differential analyses for RNA-seq: Transcript-level estimates improve gene-level inferences’, *F1000Research*, 4. Available at: <https://doi.org/10.12688/F1000RESEARCH.7563.2/DOI>.

Sperb, N., Tsesmelis, M. and Wirth, T. (2020) ‘Crosstalk between Tumor and Stromal Cells in Pancreatic Ductal Adenocarcinoma’, *International Journal of Molecular Sciences*, 21(15), p. 5486. Available at: <https://doi.org/10.3390/IJMS21155486>.

ter Steege, E.J. and Bakker, E.R.M. (2021) ‘The role of R-spondin proteins in cancer biology’, *Oncogene 2021 40:47*, 40(47), pp. 6469–6478. Available at: <https://doi.org/10.1038/s41388-021-02059-y>.

Steele, C.W. *et al.* (2016) ‘CXCR2 Inhibition Profoundly Suppresses Metastases and Augments Immunotherapy in Pancreatic Ductal Adenocarcinoma’, *Cancer cell*, 29(6), pp. 832–845. Available at: <https://doi.org/10.1016/J.CCELL.2016.04.014>.

Stephens, M. (2017) ‘False discovery rates: a new deal’, *Biostatistics*. 2016/10/21, 18(2), pp. 275–294. Available at: <https://doi.org/10.1093/biostatistics/kxw041>.

Stromnes, I.M. *et al.* (2014) ‘Targeted depletion of an MDSC subset unmasks pancreatic ductal adenocarcinoma to adaptive immunity’, *Gut*, 63(11), pp. 1769–1781. Available at: <https://doi.org/10.1136/GUTJNL-2013-306271>.

Suri, R., Zimmerman, J.W. and Burkhart, R.A. (2020) ‘Modeling human pancreatic ductal adenocarcinoma for translational research: current options, challenges, and prospective directions’, *Annals of pancreatic cancer*, 3. Available at: <https://doi.org/10.21037/APC-20-29>.

Suzuki, T. *et al.* (2021) ‘Mutant KRAS drives metabolic reprogramming and autophagic flux in premalignant pancreatic cells’, *Cancer Gene Therapy* [Preprint]. Available at: <https://doi.org/10.1038/s41417-021-00326-4>.

Takahashi, N. *et al.* (2022) ‘Replication Stress Defines Distinct Molecular Subtypes Across Cancers’, *Cancer Research Communications*, 2(6). Available at: <https://doi.org/10.1158/2767-9764.crc-22-0168>.

Takenaka, W. *et al.* (2023) ‘KRT13 is upregulated in pancreatic cancer stem-like cells and associated with radioresistance’, *Journal of Radiation Research*, 64(2), p. 284. Available at: <https://doi.org/10.1093/JRR/RRAC091>.

Talathi, S.S., Zimmerman, R. and Young, M. (2023) ‘Anatomy, Abdomen and Pelvis, Pancreas’, *StatPearls* [Preprint]. Available at: <https://www.ncbi.nlm.nih.gov/books/NBK532912/> (Accessed: 11 July 2023).

Talevich, E. *et al.* (2016) ‘CNVkit: Genome-Wide Copy Number Detection and Visualization from Targeted DNA Sequencing’, *PLoS computational biology*, 12(4). Available at: <https://doi.org/10.1371/JOURNAL.PCBI.1004873>.

Tarasov, A. *et al.* (2015) ‘Sambamba: fast processing of NGS alignment formats’, *Bioinformatics*, 31(12), pp. 2032–2034. Available at: <https://doi.org/10.1093/BIOINFORMATICS/BTV098>.

Tate, J.G. *et al.* (2019) ‘COSMIC: the Catalogue Of Somatic Mutations In Cancer’, *Nucleic Acids Research*, 47(D1), pp. D941–D947. Available at: <https://doi.org/10.1093/NAR/GKY1015>.

The Cancer Genome Atlas Research Network (2017) ‘Integrated Genomic Characterization of Pancreatic Ductal Adenocarcinoma’, *Cancer cell*, 32(2), pp. 185–203e.13. Available at: <https://doi.org/10.1016/J.CCELL.2017.07.007>.

- Tian, C. *et al.* (2019) ‘Proteomic analyses of ECM during pancreatic ductal adenocarcinoma progression reveal different contributions by tumor and stromal cells’, *Proceedings of the National Academy of Sciences*, 116(39), pp. 19609–19618. Available at: <https://doi.org/10.1073/PNAS.1908626116>.
- Tiriac, H. *et al.* (2018) ‘Organoid Profiling Identifies Common Responders to Chemotherapy in Pancreatic Cancer’, *Cancer Discov.* 2018/06/02, 8(9), pp. 1112–1129. Available at: <https://doi.org/10.1158/2159-8290.CD-18-0349>.
- Tsai, S.Q. *et al.* (2017) ‘CIRCLE-seq: A highly sensitive in vitro screen for genome-wide CRISPR-Cas9 nuclease off-targets’, *Nature Methods*, 14(6). Available at: <https://doi.org/10.1038/nmeth.4278>.
- Turinetto, V. and Giachino, C. (2015) ‘Multiple facets of histone variant H2AX: a DNA double-strand-break marker with several biological functions’, *Nucleic Acids Res.* 2015/02/26, 43(5), pp. 2489–2498. Available at: <https://doi.org/10.1093/nar/gkv061>.
- Turner, K.M. *et al.* (2017) ‘Extrachromosomal oncogene amplification drives tumour evolution and genetic heterogeneity’, *Nature*. 2017/02/09, 543(7643), pp. 122–125. Available at: <https://doi.org/10.1038/nature21356>.
- Waddell, N. *et al.* (2015) ‘Whole genomes redefine the mutational landscape of pancreatic cancer’, *Nature*, 518(7540), pp. 495–501. Available at: <https://doi.org/10.1038/NATURE14169>.
- Walkowska, J. *et al.* (2022) ‘The Pancreas and Known Factors of Acute Pancreatitis’, *Journal of Clinical Medicine* 2022, Vol. 11, Page 5565, 11(19), p. 5565. Available at: <https://doi.org/10.3390/JCM11195565>.
- Weeber, F. *et al.* (2015) ‘Preserved genetic diversity in organoids cultured from biopsies of human colorectal cancer metastases’, *Proceedings of the National Academy of Sciences of the United States of America*, 112(43), pp. 13308–13311. Available at: <https://doi.org/10.1073/pnas.1516689112>.
- White, B.D., Chien, A.J. and Dawson, D.W. (2012) ‘Dysregulation of Wnt/ β -catenin signaling in gastrointestinal cancers’, *Gastroenterology*, 142(2), pp. 219–232. Available at: <https://doi.org/10.1053/J.GASTRO.2011.12.001>.

- Witkiewicz, A.K. *et al.* (2015) ‘Whole-exome sequencing of pancreatic cancer defines genetic diversity and therapeutic targets’, *Nature Communications*, 6. Available at: <https://doi.org/10.1038/NCOMMS7744>.
- Wu, S *et al.* (2019) ‘Circular ecDNA promotes accessible chromatin and high oncogene expression’, *Nature*. 2019/11/22, 575(7784), pp. 699–703. Available at: <https://doi.org/10.1038/s41586-019-1763-5>.
- Wu, Sihan *et al.* (2019) ‘Circular ecDNA promotes accessible chromatin and high oncogene expression’, *Nature* 2019 575:7784, 575(7784), pp. 699–703. Available at: <https://doi.org/10.1038/s41586-019-1763-5>.
- Yang, S., Liu, Q. and Liao, Q. (2021) ‘Tumor-Associated Macrophages in Pancreatic Ductal Adenocarcinoma: Origin, Polarization, Function, and Reprogramming’, *Frontiers in Cell and Developmental Biology*, 8, p. 607209. Available at: <https://doi.org/10.3389/FCELL.2020.607209>.
- Yi, E. *et al.* (2022) ‘Live-cell imaging shows uneven segregation of extrachromosomal DNA elements and transcriptionally active extrachromosomal DNA hubs in cancer’, *Cancer discovery*, 12(2), p. 468. Available at: <https://doi.org/10.1158/2159-8290.CD-21-1376>.
- Ying, H. *et al.* (2016) ‘Genetics and biology of pancreatic ductal adenocarcinoma’, *Genes & Development*, 30(4), p. 355. Available at: <https://doi.org/10.1101/GAD.275776.115>.
- Zeisberg, E.M. *et al.* (2007) ‘Discovery of endothelial to mesenchymal transition as a source for carcinoma-associated fibroblasts’, *Cancer research*, 67(21), pp. 10123–10128. Available at: <https://doi.org/10.1158/0008-5472.CAN-07-3127>.
- Zhang, Y. *et al.* (2013) ‘Canonical wnt signaling is required for pancreatic carcinogenesis’, *Cancer research*, 73(15), pp. 4909–4922. Available at: <https://doi.org/10.1158/0008-5472.CAN-12-4384>.
- Zhang, Z. *et al.* (2018) ‘Role of angiogenesis in pancreatic cancer biology and therapy’, *Biomedicine & Pharmacotherapy*, 108, pp. 1135–1140. Available at: <https://doi.org/10.1016/J.BIOPHA.2018.09.136>.
- Zhong, Z. *et al.* (2020) ‘Wnts and the hallmarks of cancer’, *Cancer and Metastasis Reviews* 2020 39:3, 39(3), pp. 625–645. Available at: <https://doi.org/10.1007/S10555-020-09887-6>.

Zhu, Y. *et al.* (2021) ‘Oncogenic extrachromosomal DNA functions as mobile enhancers to globally amplify chromosomal transcription’, *Cancer Cell*, 39(5), pp. 694-707.e7. Available at: <https://doi.org/10.1016/J.CCELL.2021.03.006>.

7. Acknowledgments

There are many people, without whom, this thesis would have not been possible. With this section I would like to express my gratitude to those, who have contributed either directly to the scientific process, or who have supported me in other ways throughout my PhD.

First, I would like to express my gratitude to my supervisor **Prof. Vincenzo Corbo**, for supporting me and guiding me. Dear Vincenzo, thank you for allowing me to join your research group. You set an example for what a scientist and a mentor should be, and I have learned a lot from you.

I would also like to thank my mentor in the lab, **Dr. Elena Fiorini**. Dear Elena, master of western blots, mice, the liquid nitrogen, and the last chocolate brioche. It has been a privilege to learn from you. You were an integral part of the ecDNA project, and I want to sincerely thank you for taking it on after I left the lab. You are an incredible scientist/human and I hope we keep in touch.

I am also extremely grateful to **Daniel Schreyer and Dr. Peter Bailey** from the University of Glasgow. Your computational analyses provided the basis framework for the ecDNA project, and I have learnt a lot from working with both of you. Daniel, it was a pleasure having you work in Verona, and I hope to see you soon in Munich.

My gratitude also goes to the two bioinformaticians in our lab, **Francesco Pezzini and Davide Pasini**. Thank you for completing sequencing analyses, for being patient with my questions and my nagging, and for teaching me some R tricks along the way.

I would like to thank **Silvia Andreani**, who taught me how to work with organoids and showed me the ropes around the lab. Dear Silvia, your craziness in Verona is dearly missed, but I wish you good luck with your PhD and hope to see you soon in Germany.

I would like to thank the other members of the Corbo lab: **Dr. Michele Bevere, Lisa Veghini, and Dr. Francesca Lupo**. Dear Michele, thank you for your PCR help and for being a top neighbour! Dear Lisa, thank you putting up with my paranoia regarding cell contamination and my venting, and for teaching me all your know-how on both western blots and RT-PCRs. Dear Fra, my PhD journey would have

not been the same without your sassy Italian remarks. Thank you all for always being happy to help.

I would like to express my gratitude to the members of the ARC-NET Biobank, particularly **Sonia Grimaldi, Dr. Borislav Rusev, and Dr. Davide Antonello** for always providing accurate tissue analysis and on-time patient data.

Vorrei anche ringraziare i tecnici di laboratorio del reparto di anatomia-patologia, per aver eseguito le colorazioni dei tessuti e per avermi concesso l'utilizzo del loro microtomo. Vorrei ringraziare **Serena Pedron**, in particolare, per aver eseguito gli esperimenti FISH.

My secondment in Leiden was a highlight of my PhD and therefore I would like to thank **Dr. Karla Queiroz and Dr. Marlene Geyer** for welcoming me and guiding me at MIMETAS. **Laura**, thank you for providing me with housing, chats, and dog's cuddles whilst I was there!

Finally, I would like to thank the external reviewers for reading this thesis: **Prof. Christian Pilarsky** from the University of Erlangen and **Dr. Mariano Ponz-Sarvisé** from the University of Navarra.

As difficult a PhD can be, I was lucky enough to have amazing friends, who helped me along the way.

Robin, my PhD comrade. Thank you for double checking my cell culture math, listening to my presentations late at night, or for just being there.

Delia, my MSc thesis buddy, my Yogi! Thank you for taking me under your wing all those years ago, teaching me Yoga, and providing me with much needed perspective.

Vladi, master of all boulders. Thank you for all our calls, calming me down that it is "all just business" and for honouring me to be your paranymph at your PhD thesis defence.

Поли, няма значение през колко време не сме се чували, ти винаги откликваш! Благодаря ти за безкрайните истории от София и от Глазгоу.

To the rest of my extended Maastricht family: **Nienke, Claudia, Timo, Angela, Marco, Jana, Daniela, Frederik C, Nico, Greg L., and Greg W.** Your birthday

calls, zoom parties, and online improv sessions helped keep me sane. You are all incredible people to know and even better friends to have.

Bas, my partner, and my rock. Thank you for listening to my presentations, spotting all my typos, even though you had no idea what I was talking about, and for doing all my piled-up recycling, whenever you were visiting! I love you.

Благодаря на моето семейство за безкрайната емоционална и финансова подкрепа. На **мама и тати**, без които никога нямаше да стигна до тук. На моята прекрасна **баба Донка**, която ми даде първите насоки и вдъхновение в биологията. На прекрасната ми сестра **Мария и нейното семейство, Йонас-Боян и Себастиан**. Йонасче, babysitting you, дори и в 6 сутринта в събота, беше остров на щастие сред море от стрес.

Thank you all for being such inspiring and supportive individuals!